Surface Acoustic Wave Propagation in Anisotropic Layered Mediums for Biosensor Application: Characterisation and Numerical Method Development

Nathan Craig BEng, MSc

School of Engineering

Newcastle University

This thesis is submitted for the degree of

Doctor of Philosophy

November 2018

I would like to dedicate this thesis to my loving partner for her endless patience and support.

Acknowledgements

And I would like to acknowledge the support of the staff and fellow students of the formerly named, School of Mechanical and Systems Engineering. I would like to thank my supervisor, Dr H.T.D. Grigg, for the support and mentorship, along with their unyielding faith in me, and Dr B.J. Gallacher for their experienced counsel.

I acknowledge the presentation of the currently unpublished transducer design in this thesis, created by Dr H.T.D Grigg. The design in question was created as a collaboration, using data generated by the methods of this research.

Abstract

The main motivation for conducting this research is the continued development of multilayered mechanical biomedical sensors. Biosensors which make use of resonant surface acoustic waves are a contender for Point-of-Care diagnostic technology. An area of interest for this research group, is in microsystem devices that make use of the cyclic degeneracy of cylindrical geometry. Ideally, these modes would remain invariant in the angular axis of the polar form geometry, in reality this isotropy can not be guaranteed. In multilayered biosensor design, various properties of the material and geometry, will introduce anisotropic behaviour. The main focus of this research is the effect of these properties on this variation of the wave modes with, the propagation angle in a material cut. A minor focus is placed on the effect of the various attenuation mechanisms, due to these physical properties, on the quality of the wave resonance.

A uniform numerical framework is developed, by making use of the multidimensional complex structure of the functions, capable of solving all the problems presented. The numerical method, which is well-suited to fixed velocity searches, is combined with optimisation methods to improve efficiency with other search variables. For biosensor application, the common attenuated mechanisms are modelled, these include bulk leaky, viscoelastic, fluid and thermoelastic losses. The effect of these on the annular variation, in addition to the stiffness anisotropic and waveguide dispersions, is investigated. The fixed velocity solutions are computed for several propagation angles, for both novel and currently feasible biosensor combinations. The non-fixed velocity versions of these surfaces are computed for use in shaped annular transducer designs. For the material combinations of interest for sensor application, the different sources of attenuation are compared using a Q-factor approach.

The research conducted in this thesis, provides insight into the material properties that alter the variation of wave modes with angle. Design and research recommendations for mechanical biosensors, have been made based on the cyclic variation and attenuation investigations.

Table of contents

List of figures

List of tables

Nomenclature

Superscripts

E	At constant electric field
ε	At constant strain
I	Incident
R	Reflected
T	At constant temperature

Symbols

A_4	Fourth component of wave amplitude either pressure, thermal or electrical
A_i	Components of wave amplitude $\boldsymbol{A}$
α	Attenuation as the imaginary part of the wavenumber
β	Real part of the wavenumber
C	Specific heat capacity
c_0	Constant speed of sound of a fluid
C_{ij}	Vogit stiffness notation
C_{ijkl}	Stiffness tensor
$\boldsymbol{Z}_i$	Covarient basis
ρ	Density
D_i	Components of electric displacement
d_{ijk}	Piezoelectric coupling tensor

E	Energy of a resonator
e_{ij}	Dielectric tensor
E_{kl}	Strain rate tensor
η	Shear viscosity
ω	Frequency
G	Shear modulus
G'	Shear storage
G''	Shear loss
h	Thickness of a layer on a half-space
k_i	Components of wavenumber $\boldsymbol{k}$
K_{ij}	Thermal conductivity tensor
λ_{ij}	Thermal expansion tensor
λ_i	Components of wavelength $\boldsymbol{\lambda}$
L_i	Components of traction amplitude $\boldsymbol{L}$
m_i	Components of propagation direction along surface $\boldsymbol{m}$
Z_{ij}	Metric tensor
μ_{ijkl}	Viscosity tensor
n_i	Components of decay direction normal to the surface $\boldsymbol{n}$
P	Pressure of a fluid medium
p	Partial wave multiplier
ϕ	Electric potential
Γ_{ij}	Propagation tensor
ρ_0	Initial value of density
ε_{kl}	Strain tensor

σ_{ij}	Stress tensor
t	Time
T_0	Reference temperature
t_i	Components of the tractions $\boldsymbol{t}$ in n_j
δT	Small change in temperature
u_i	Components of wave displacement $\boldsymbol{u}$
v	Phase velocity
V_i	Particle velocity, time derivative of wave displacement u_i
X_i	Components of wave vector $\boldsymbol{X} = [\boldsymbol{m} \cdot \boldsymbol{x},\ \boldsymbol{p} \cdot \boldsymbol{x},\ \boldsymbol{n} \cdot \boldsymbol{x}]$
x_i	Components of Cartesian coordinate system $\boldsymbol{x}$

Acronyms / Abbreviations

A	Anisotropy as in A-factor of stiffness parameters
BAW	Bulk Acoustic Wave
FBAR	Film Bulk Acoustic Resonator
IDT	Interdigital Transducer
LSAW	Leaky Surface Acoustic Wave
MEMS	Micro-Electro-Mechanical Systems
PoC	Point-of-Care
P	Longitudinal (pressure) waveform or displacement
PZT	Lead Titanate Zirconate
QCM	Quartz Microbalance
QL	Quasi-Longitudinal waveform or displacement
Q	Quality as in Q-factor
QS	Quasi-Shear waveform or displacement

SAW	Surface Acoustic Wave
SH	Shear horizontal waveform or displacement
SV	Shear vertical waveform or displacement
TSM	Thickness Shear Mode

Chapter 1

Introduction

1.1 Motivation

Mechanical biosensors are one of the few types of biosensor that have the potential for rapid detection of biology molecules for portable devices. Wave based mechanical biosensors use the change in properties of a propagating waveform, to detect the presence of the biological analyte. This work is focused on a group of wave types known as surface acoustic waves (SAWs), which are highly localised at the surface of a material. A large number of biosensors that make use of SAWs, typically only in planar geometries easily represented by Cartesian coordinates. In this work, biosensors that make use of cylindrical geometries are of interest, along with the unique properties that these devices possess.

1.1.1 Surface acoustic waveforms

Mechanical resonant wave biosensors, use the shift in resonance frequency, caused by the mass increase at the binding site of a biosensor. The shift in the resonance frequency of the device is greater for a lower active mass, when the resonator mass is closer to the loaded substance. Therefore, the higher the frequency of the propagating waveform, the lower the wavelength and generalised mass that takes part in the active dynamics. Bulk acoustic waves (BAWs) that propagate through-the-thickness would require small thicknesses, approaching the microscale, to achieve higher frequencies. SAWs are localised at the surface of a material, therefore these waveforms can naturally operate at higher frequencies, without impacting cost or reliability. The requirement for high frequencies puts biosensor technology within the field of micro-electro-mechanical systems (MEMS).

Many different types of SAWs exist in elastic materials of interest, they exist in different types of crystals and with other physical mechanisms, in addition to elasticity. Two well known isotropic SAWs are the Rayleigh wave, which can exist in single materials and the Love wave, which exists in layered mediums. These waveforms will be central to the research conducted in this thesis and both have been used in the development of SAW biosensors.

1.1.2 Cylindrical geometry and degeneracy

A sensor designed on cylindrical geometry could have many desirable properties, including strong common mode rejection and high resonator Q-factor. An attractive physical phenomenon of polar geometry is the ability to propagate cyclic modes [4–6] that have the same natural frequencies called degenerate modes. The structure of these modes is similar to the orthogonal trigonometric functions sin($n\theta$) and cos($n\theta$), where n is a non-zero integer. In fact, these degenerate modes are seperable functions, that take the forms $F(r,z)cos(n\theta)$ and $F(r,z)sin(n\theta)$. These functions propagate in the angular (θ) axis of a polar coordinate system, see Figure 1.1.

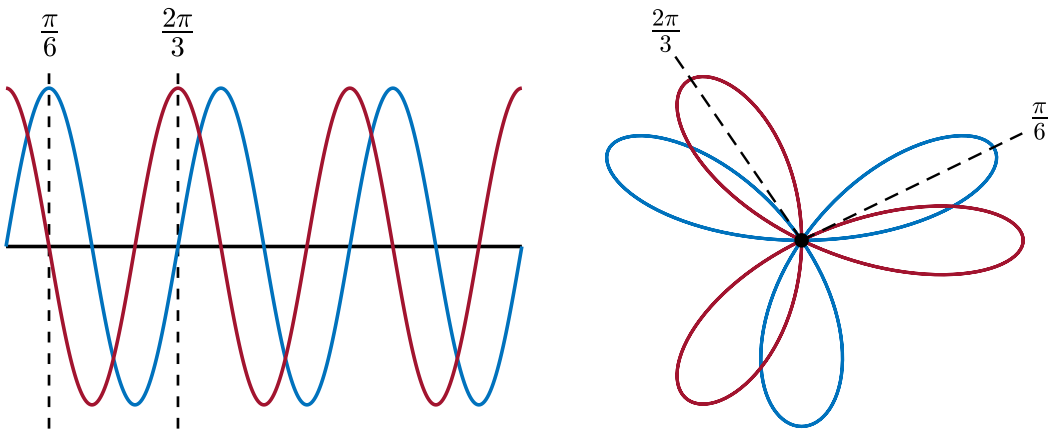

(a) Cartesian (b) Polar

Fig. 1.1 Example of orthogonal trigonometric functions sin3θ and cos3θ in (a) Cartesian and (b) positive part of the polar form coordinates. Note the orthogonality of the functions at the marked points $\frac{\pi}{6}$ and $\frac{2\pi}{3}$.

The orthogonality of these degenerate modes, make them useful for a mechanical sensing mechanism under mass loading. Illustrated in Figure 1.1b, this orthogonality is marked at $\frac{\pi}{6}$ and $\frac{2\pi}{3}$, mass loading at one of these sites will alter one of the modes. The mass loading causes a shift in the resonant frequency of one of the degenerate modes, causing a split from a single resonant frequency peak. This mechanism is called degeneracy breaking, this means that the sensing and reference signals are embedded into a single device. The major advantage

of this design over traditional mechanical biosensors, such as the dual delay-line, come as a result of the compactness and single material cut. Theoretically, the degenerate modes within these devices are equally affected by change in fields such as temperature or stress. Therefore, degenerate biosensors are more robust in real world applications in which error due to mechanical components can impact the reliability of the sensors.

The propagation of degenerate modes is highly dependent on the cyclic symmetry of the device, in which the circumferentially invariation isotropic case has infinite symmetry. For this isotropic case, the cyclic modes may be represented as the seperable functions of the coordinate system, and therefore are solvable. Unfortunately, the common materials used in biosensing technology are anisotropic in their material tensors, primarily the stiffness and piezoelectric coupling. These anisotropic effects are no longer seperable in the polar form coordinates, which will disturb the degeneracy of the cyclic modes. Provided a symmetry structure does exist, then cyclic degenerate modes may be tailored and optimised to that symmetry. A major theme of this work is the study of the impact of anisotropy, due to the stiffness tensor, on the cyclic symmetry of layered solutions. In addition, the study of the interaction of anisotropy with waveguide dispersion, along with other material properties and sources of energy loss.

1.2 Review of Biosensor Technology

A primary objective in Point-of-Care (PoC) diagnostic research is the development of MEMS biosensors that are low cost, highly sensitive and highly specific to the desired analyte [1]. Biosensing research is a well established and funded research field, due to the large global market value of the technology [2, 3], along with predicted future impact. The research area is not limited to any one school of expertise but is a combination of biological, chemical, mechanical and electrical engineering fields. Due to this, many types of biosensors exist, based on different sensing mechanisms and shifts in physical properties, which has lead to a vast amount of research and review papers on the subject.

The following is a brief summarisation of the review papers for biosensing technology. Several reviews exist for a general overview of different biosensing technologies [7–13], for this work, the interest is placed on label-free sensors [14–18], particularly sensors based on mass loading of an analyte, discussed in section 1.2.1. This research is focused on acoustic biosensors [19–26] with particular interest placed on SAW devices [27–31], other common acoustic types include shear bulk [32–34] and resonant cantilever sensors [35–37]. For completeness, review papers also exist for radiation force mechanisms, which make use of acoustic wave techniques for

sensing [38, 39]. Additionally, graphene based sensor technology [40] is becoming increasingly popular due to the unique properties of graphene. Particularly, for mass loading sensors, as they take advantage of the one atom thick crystal lattice for large detectible resonant frequency shifts with analyte binding.

1.2.1 Mass loading biosensors

In this section, a brief summary of the mass loading biosensor is presented, for an in-depth analysis of the literature see the relevant review papers. Mass loading biosensors, of interest, detect some change in a mechanical property caused by the added mass of an analyte, such as deflection or a wave property. Focus is placed on biosensors that make use of shifts in resonant frequency, using a selected normal mode, excited by reflectors. The waveforms within these devices are excited using piezoelectric effects of the material, generated by using interdigital transducers (IDTs) on the surface of the material. These IDTs can also be used to detect the shifts in wave property, due to the linear piezoelectric mechanism back from mechanical to electrical. Other coupling mechanisms may be used to excite waveforms in multiferroic materials such as magnetic coupling, the focus in this thesis is solely on the piezoelectric behaviour.

Focusing on biosensors that make use of mechanical waves, the first type of mass loading biosensors in this discussion uses thickness shear mode (TSM). This waveform propagates with a displacement that reaches through-the-thickness of the material from the top to the bottom of a plate. These biosensors are known as film bulk acoustic resonators (FBAR); among TSM biosensors the most popular design is the quartz microbalance (QCM) which has been well developed. These devices are also known as thin FBAR, due to the requirement of low thickness to decrease the generalised mass and increase the senstivity of the resonant frequency shift. This requirement is also the major limitation of this type of biosensor, design of these devices are a trade off between high frequency and reliability.

SAW based biosensors make use of propagating surface localised waveforms, which decay into the bulk of the material. Due to this decay, these devices may operate at high frequencies with larger thicknesses than FBAR type biosensors. In single isotropic materials the Rayleigh waveform comes into existence due to the stress-free surface. This SAW has an epiltical displacement form, which is a combination of out-of-plane and in-plane longitudinal displacements. In the layered isotropic half-space, the Love wave can come into existence, this is dependent on the relative bulk wave velocities of the layer and substrate, discussed further in Chapter 2. Unlike the Rayleigh wave, these Love waves have a pure in-plane shear displacement pattern.

Love waves are perceived to be superior due to the low fluid loss of the shear mode. In the case of the Rayleigh wave, the out-of-plane displacements couple to generate bulk propagating fluid pressure waves. These views are based off traditional biosensor designs, and have not been well quantified for many relevant cases. Plane wave biosensors use an input and output set of IDTs with an analyte binding site between the IDTs, a second reference device may be used along with the first, in a dual delay-line configuration.

1.2.2 Materials for acoustic wave biosensors

Throughout this work, the focus is placed on pizeoelectric materials; these operate by taking advantage of the coupling between mechanical and electrical properties to excite and detect the waveforms. The multilayered structures must contain a pizeoelectric material with the desired piezoelectric coupling components to generate propagating SAWs. The type, cut and manufacturing process of the material can all effect the Q-factor of the resulting MEMS device by acoustic loss mechanisms. By systematic sampling of the literature, a review of commonly used materials in acoustic biosensors is presented, for both single and multilayered configurations.

Quartz (SiO_2) is a piezoelectric trigonal crystal, in α-quartz configuration, it is popular for electronic applications due to the high performance versus inexpense of the material. The most common mechanical biosensor design is the QCM which is one of the most well studied acoustic biosensors, see review papers [41–47]. The device makes use of the TSM, due to this choice of waveform the limiting factor for sensitivity is thickness of the quartz. Typically the resonance frequency of these sensors operate between 10 to 50 MHz, it is desirable to push the frequency higher for increased sensitivity requiring lower thicknesses. Designing these devices becomes an optimisation problem between the sensitivity and thickness, thin devices can become too fragile for real world application. Quartz is a well researched material in standard cut cases which are of interest for QCM devices. The most commonly used cut for generating shear waves is the AT-cut [48, 49] which is a 35°rotation from the Y-cut [50, 51] around the X-axis [52]. ST-cut is another common cut of quartz typically used for layered acoustic biosensors.

Zinc oxide (ZnO) is a common piezoelectric crystal for use in several different types of biosensors [53] with an 6mm hexagonal structure. ZnO is used in electrochemical [54, 55], optical [56] and acoustic [57] type biosensors. ZnO has been used in multilayered SAW and FBAR type biosensors and is typically used as a thin film on top of substrate materials [20]. The material is a possible contender for acoustic biosensors due to the high piezoelectric coupling coefficient, and the ability to manufacture multilayered MEMS devices. The hexagonal structure

of ZnO leads to transverse isotropy [58], beneficial for pure shear SAW propagation. A transverse isotropic crystal is also useful in cylindrical geometry sensors, that require high cyclic symmetry.

Lead titanate zirconate (PZT) ceramic is a less commonly used piezoelectric material for biosensors, it has been used in many types of acoustic biosensors [59–63]. PZT has an hexagonal crystal structure with transverse isotropy, making it of interest for applications in cylindrical biosensors [64]. One of the drawbacks of PZT is that it contains the toxic substance lead, lead-free alternatives are more desirable [65, 66], modern trends are moving in the direction of removing all lead from electronics.

Aluminium nitride (AlN) ceramic is another piezoelectric material, just as with ZnO this material is typically used as a thin film layer [67, 68, 20]. In recent years this material has been used in biosensors that use bulk waves in layered thin films [33, 70–72] and SAWs in multilayered configurations [73, 74]. AlN has a Wurtzite crystal structrue which is within the crystal class of hexagonal crystals and has been shown to have a transverse isotropic plane [75]. As with ZnO, the isotropic plane, along with the use of AlN as a thin flim layer, means the material is of interest for applications of biosensors with cylindrical geometry.

Lithium niobate ($LiNbO_3$) is a piezoelectric material with a trigonal crystal structure with a quasi-6-fold cyclic symmetry in the Z-cut [76], but is in fact 3-fold. The material is transparent, due to this it has been used in various optical wave applications including electro-optical biosensors [77]. The material has been used for acoustic biosensors of several types [78–80], fluid-sensor interactions have been numerically computed for this material [81–83]. The material has been used for a degenerate mode biosensor [84] in which Z-cut $LiNbO_3$ is manufactured with circular geometry [85, 86]. Another common cut of $LiNbO_3$ throughout the literature is 128°Y-cut.

Lithium tantalate ($LiTaO_3$) was an early piezoelectric material considered for SAW and Leaky-SAW biosensors [27, 87, 88], it has a trigonal structure of the same form as ($LiNbO_3$). Despite the early use of this material for SAW biosensors the literature is quite limited, the material has been used mostly as a substrate material for SH-SAW devices. Numerical work exists for hexagonal geometry, in the annular axis of the cut, for $LiTaO_3$ [89]. Even though this concept is limited in scope it relates closely to cylindrical biosensor devices, by requiring some form of inhomogeneous shape which is linked to the anistropy of the chosen material and cut.

Multilayered SAW devices have a number of advantages over BAW and single material SAW devices due to the existence of in-plane shear SAW modes. The remainder of this section is devoted to the review of material combinations using the piezoelectric materials that have already been discussed along with other commonly used materials. Table 1.1 gives an overview of the

literature for different combinations of layer and substrate materials. The literature is comprised mostly of biosensors with some other MEMS devices and feasibility studies, for a detailed review of film deposition techiques see [20].

	Quartz	$LiNbO_3$	$LiTaO_3$	Silica	Silicon
ZnO	[90–96]	[95, 97, 98]	[99–101]	[102]	[102]
PZT	[103]	—	—	—	[104, 105]
AlN	[106, 116, 108]	[109–112]	—	[113, 114]	[113–116]
Silica	[117–120]	[121–123]	[124–126]	—	—
PMMA	[127, 128, 120]	[129–131]	[132, 133]	—	[134]
SU-8	[135–137]	—	—	—	—

Table 1.1 Review of combinations of layer materials (down the rows) and substrate materials (across the columns) throughout biosensor and feasibility literatures

Materials typically used as substrates may be grown or directly bonded onto other substrates, the following is a brief summary. Quartz may be bonded directly onto silicon [138–141] using SiO_2 and quartz has also been shown to be bonded onto $LiNbO_3$ [142] using SiO_2. Lithium niobate has also been shown to be directly bonded onto silicon using SiO_2 [143] and SU-8/SiO_2 [144], also a study of the growth on silicon using ZnO/SiO_2 layers, has been researched [145].

1.3 Scope of Research

1.3.1 Aim

The investigation into the nature of generalised multilayered surface acoustic wave modes in particular material cases of interest for mechanical biosensor design.

1.3.2 Objectives

The following is a list of three broad research objectives which each following a distinct trend. The first is engineering application focused, the second is gaining physical insight and knowledge, and the third is numerical method development.

1. Applications in sensor design.
    - Formulate models of multiple sources of wave energy loss and then identify, characterise and optimise the major sources of loss, for cases of interest to biosensor application.
    - Identification of physical wave behaviour that may be used to enhance existing mechanical sensing mechanisms or develop novel sensing mechanims.
    - Investigate the variation of the cyclic symmetry of SAW modes for the purpose of cylindrical sensor design.
2. Characterisation of SAW modes that may exist.
    - Characterisation of loss in fluid loaded SAW solutions in isotropic and anisotropic layered media.
    - Investigate the difference in energy loss between the Rayleigh and Love wave types caused by the fluid loading.
    - Study of the displacement pattern for the generalised anisotropic versions of well-studied wave types, for several mulitlayered combinations.
3. Numerical tool development.
    - Develop generalised and efficient methodology to compute a large range of propagating waveforms for various material properties.
    - Expand the numerical methods to allow the capture of energy attenuating waveforms.
    - Development of polar form extension of these numerical methods.

1.3.3 Research questions

The following is a list of research questions that might be answerable throughout the course of this research. Though these questions are linked to the application and objectives, they may also be viewed as areas where insight to a particular physical behaviour is of interest. Through this insight current biosensor designs may be improved and novel concepts may be found.

1. In the layered half-space problem, the wavelength may vary from small to large values, due to the interaction of waveguide dispersion and SAW decay behaviour. How does the symmetry of the solution relate to the symmetry of the material? How do the symmetries of the contributing materials interact to give rise to the symmetry of the multilayered solution? And does the solution symmetry smoothly transition between that of the layer and of the substrate, dependent on the layer thickness?

2. What are the most significant forms of energy loss for mechanical SAW biosensors using anisotropic multilayered waveforms? How can these forms be mitigated from a design and material perspective?

3. For the pure isotropic case, the loss due to fluid loading is assumed to be small in Love waves, compared to Rayleigh waves. To what degree is this true? And how does this differ in the anisotropic case?

4. For multilayered SAW modes within a layered medium comprised of conflicting symmetries, how do the generalised displacements lead to increased or decreased energy loss? And how does the energy loss now vary with the propagation angle?

5. What will the form of the displacement be for the generalised versions of the well-known isotropic wave types in different layered anisotropic media? And how will this impact the piezoelectric coupling of these modes? Is it possible to produce and detect a shear dominated waveform by out-of-plane transducer coupling?

Chapter 2

Elastic Waveforms

This chapter covers the mathematical and physical background knowledge of waveforms, as a prerequisite to topics covered in Chapter 4 through to Chapter 7. The existence of surface acoustic waves, (SAWs) and the classification of these waves in materials with anisotropic stiffness is reviewed. The concepts of anisotropic compatibility between different layered materials, and the transition of isotropic to anisotropic waveforms are introduced. At the end of this chapter bulk wave solutions, and layered bulk wave combinations have been computed as a reference for future chapters.

2.1 Mathematical Preliminaries

The traditional approach for mathematical modelling of problems in continuum mechanics is to use tensor formulation. The advantage of this approach is that the model captures the couplings between all direct and shear interactions, along with anisotropic structures, in a compact form. These are key to the physical behaviours studied throughout this work for application in mechanical biosensors. Formulations are based on continuum mechanics theory using tensor calculus [1], tensor notation is based on [2].

2.1.1 Cartesian wave equation

The Cartesian coordinates in 3-dimensions $x_i = [x_1\ x_2\ x_3]$ where $x_i \in \mathbb{R}$ is used throughout this work. Using this coordinate system, in Appendix A, results in the 3-dimensional linear wave equation for an elastic medium,

$$C^{ijkl}\frac{1}{2}\left(\frac{\partial^2 u_l}{\partial x^j \partial x^k} + \frac{\partial^2 u_k}{\partial x^j \partial x^l}\right) = \rho\frac{\partial^2 u^i}{\partial t^2}. \tag{2.1}$$

The stiffness C^{ijkl} is assumed to be homogeneous, density ρ is a constant and it is assumed that no other forces are acting on the body. The contravariant components of the displacments $\boldsymbol{u}$ are denoted u^i and t denotes time. The rank-4 stiffness tensor has two minor symmetries due to the symmetry of the stress,

$$\sigma^{ij} = \sigma^{ji} = C^{ijkl}\varepsilon_{kl} = C^{jikl}\varepsilon_{kl}, \tag{2.2}$$

and strain tensors,

$$\sigma^{ij} = C^{ijkl}\varepsilon_{kl} = C^{ijkl}\varepsilon_{lk} = C^{ijlk}\varepsilon_{kl}. \tag{2.3}$$

In addition to these minor symmetries the stiffness tensor is also symmetric known as the major symmetry,

$$C^{ijkl} = C^{klij}. \tag{2.4}$$

2.1.2 Inner product and metric

The pairwise inner products of the covariant basis vectors, denoted $\boldsymbol{Z}_i$, results in the covariant metric tensor (also called the Gram matrix in linear alegbra),

$$Z_{ij} = \langle \boldsymbol{Z}_i, \boldsymbol{Z}_j \rangle. \tag{2.5}$$

The metric tensor is fundamental for concepts in tensor calculus and differential geometry, in the latter the metric is defined first and the inner product results from the metric. The metric is used to calculate length and angles, therefore the metric is restricted to a non-degenerate symmetric bilinear form [2, 3].

Restricting the analysis to a real vector space V over the real scalar field F the inner product of any two vectors in V is,

$$\langle \boldsymbol{w}, \boldsymbol{v} \rangle = \langle w^i \boldsymbol{Z}_i, v^j \boldsymbol{Z}_j \rangle = w^i v^j Z_{ij}. \tag{2.6}$$

For Cartesian coordinates the metric tensor is the kronecker delta and the inner product reduces to the known dot product,

$$\langle \boldsymbol{w}, \boldsymbol{v} \rangle = w_i \cdot v^i. \tag{2.7}$$

A metric tensor is positive definite if for any nonzero vector,

$$v^i v^j Z_{ij} > 0, \tag{2.8}$$

and is known as a Riemannian metric. For all the coordinates used throughout this work the metric tensor is Riemannian and the inner product is defined using the metric.

2.1.3 Complex vector space

For the case of a complex vector space V over a complex scalar field F, the inner product now takes the form of a Hermitian inner product, see Hermitian operators [4, 5]. The metric tensor can now be defined as,

$$Z_j^i = \langle \boldsymbol{Z}_j, \boldsymbol{Z}^i \rangle = \boldsymbol{Z}_j \cdot \overline{\boldsymbol{Z}^i}. \tag{2.9}$$

The metric acting on vectors $\boldsymbol{w}$ scaled by a and $\boldsymbol{v}$ scaled by b can be defined as,

$$Z(a\boldsymbol{w}, b\boldsymbol{v}) = a w_i \overline{\boldsymbol{Z}^i} \cdot \overline{bv^j} \boldsymbol{Z}_j = a w_i \overline{bv^j} Z_j^i. \tag{2.10}$$

Now contravariant tensors must be conjugated,

$$\overline{v^j} = v_i Z^{ij}. \tag{2.11}$$

The inner product may be defined using the covariant or contravariant metric tensor denoted Z_{ij} and Z^{ij} respectively,

$$(\overline{aw^i})(\overline{bv^j}) Z_{ij} = a w_j \overline{bv^j}, \tag{2.12}$$

$$(\overline{aw^i})(\overline{bv^j}) Z_{ij} = \overline{aw^i} b v_i. \tag{2.13}$$

But, unlike the definition, (2.10) the order of index contraction on the metric is not enforced. This is due to the conjugate symmetry of the Hermitian inner product,

$$\overline{aw^j} b v_j = \overline{(a w_j \overline{bv^j})} = (a w_i Z^{ij})(\overline{bv^i} Z_{ij}). \tag{2.14}$$

The definition of the inner product in (2.10) enforces the conjugation of the second term in the product. Note the choice of which term is conjugated is arbitary, as both still define a suitable inner product, but consitency must be maintained.

The metric tensor is called Hermitian metric if it is positive definite and can be viewed as the complex analogue of the Riemannian metric [6]. For all cases within this work the coordinate system will be real, and the resulting metric is Riemannian. Complex vectors are also used throughout the formulation of elastic waves, summation and the inner product is assumed to take the form (2.10).

2.1.4 Stroh formulation

The solution to the wave equation (2.1) is assumed to be in the Stroh form [7],

$$u_i = A_i \mathrm{e}^{-\mathrm{i}k(\boldsymbol{m}\cdot\boldsymbol{x}+p\boldsymbol{n}\cdot\boldsymbol{x})+\mathrm{i}\omega t}, \tag{2.15}$$

where $k, \omega, p \in \mathbb{C}$ are the wavenumber, frequency and unknown multiplier to be determined. The components of the amplitude $\boldsymbol{A} \in \mathbb{C}^3$ are denoted A_i. The orthonormal vectors $\boldsymbol{m}, \boldsymbol{n} \in \mathbb{R}^3$ set the propagation direction and bounday surface normal with components m_i and n_i.

In this form, the magnitude of the wavenumber is imposed in both the $\boldsymbol{m}$ and $\boldsymbol{n}$ directions, the unknown p must then be found to satisfy the wave equation. This is equivalent to finding the wavenumber in $\boldsymbol{n}$ for a fixed and consistent wavenumber in $\boldsymbol{m}$, for each of the partial wave solutions. The physical interpretation of p is discussed in Section 2.2.1 in relation to the structure of these partial waves. Substitution of (2.15) into (2.1) results in,

$$C^{ijkl}\frac{k^2}{2}\left[(m_j + pn_j)(m_k + pn_k)A_l + (m_j + pn_j)(m_l + pn_l)A_k\right] - \rho\omega^2 A^i = 0. \tag{2.16}$$

Taking advantage of the minor symmetry of the stiffness tensor, (2.3) and rearranging by index juggling results in the eigenvalue problem,

$$\left[C^{ijkl}(m_j + pn_j)(m_k + pn_k) - \rho v^2 \delta^{il}\right] A_l = 0, \tag{2.17}$$

where the phase velocity is given by $v = \frac{\omega}{k}$. The imaginary part of the phase velocity may be zero for particular combinations of k and ω with non-zero imaginary parts. For a majority of the cases presented in this work $v \in \mathbb{R}$, and the $\mathrm{Im}(k)$ and $\mathrm{Im}(\omega)$ have physical meaning in the spatial and temporal exponential decay, respectively.

The operator of the eigenvalue problem is Hermitian if it is conjugate symmetric. Up until now the conjugate contravariant has not been used, but this can no longer be ignored. To ensure that the operator is Hermitian the following statement must be true,

$$\Gamma^{il} = \Gamma_{li}, \tag{2.18}$$

expanded into,

$$C^{ijkl}(m_j + pn_j)(m_k + pn_k) = C_{lkji}(\overline{m^j + pn^j})(\overline{m^k + pn^k}) \tag{2.19}$$

where $C^{ijkl} = C_{lkji}$ due to the minor and major symmetries (2.2) - (2.4) of the stiffness tensor. Using this symmetry and the Hermitian inner product for the complex variable pn_j, this equality can be shown to be true.

The Hermitian proof comes naturally if the operator is rewritten into the following form,

$$\Gamma_{\cdot i}^{l} = C_{ij}^{\cdot\cdot kl}(\overline{m^j} + \overline{pn^j})(m_k + pn_k). \tag{2.20}$$

Full stops are used to ensure correct ordering of indices. Taking advantage of the minor and major symmetries (2.2) - (2.4) of the stiffness tensor but now (2.20) requires conjugate symmetry,

$$C_{ij}^{\cdot\cdot kl} = \overline{C_{\cdot\cdot ji}^{lk}}. \tag{2.21}$$

Due to the conjugate contravariant (2.10) the operator (2.20) is Hermitian if,

$$\Gamma_{\cdot i}^{l} = \overline{\Gamma_{\cdot i}^{l}} = \Gamma_{l}^{\cdot i}, \tag{2.22}$$

which can be easily shown as,

$$\overline{\Gamma_{\cdot i}^{l}} = \overline{C_{\cdot\cdot ji}^{lk}(\overline{m^j} + \overline{pn^j})(m_k + pn_k)} = \Gamma_{l}^{\cdot i} = C_{lk}^{\cdot\cdot ji}(m_j + pn_j)(\overline{m^k} + \overline{pn^k}). \tag{2.23}$$

2.2 Waveform Existence

For the following sections the components of the wave direction will be represented by $X_i = [X_1,\ X_2,\ X_3]$ distinguished from coordinate system notation by the captialised x. The third direction is the vector orthogonal to $\boldsymbol{m}$ and $\boldsymbol{n}$ denoted $\boldsymbol{p} = \boldsymbol{m} \times \boldsymbol{n}$. The wave direction is

then $X_i = [\boldsymbol{m} \cdot \boldsymbol{x},\ \boldsymbol{p} \cdot \boldsymbol{x},\ \boldsymbol{n} \cdot \boldsymbol{x}]$, with the wavenumbers in these wave directions given by the components $k_i = [k_1,\ k_2,\ k_3]$.

2.2.1 Bulk and partial wave

For a fixed phase velocity the eigenvalue problem (2.17) results in a characteristic polynomial of degree six in p. The solutions are the partial waves, which for an isotropic stiffness tensor are either pure imaginary complex conjugates or pure real, see Figure 2.1.

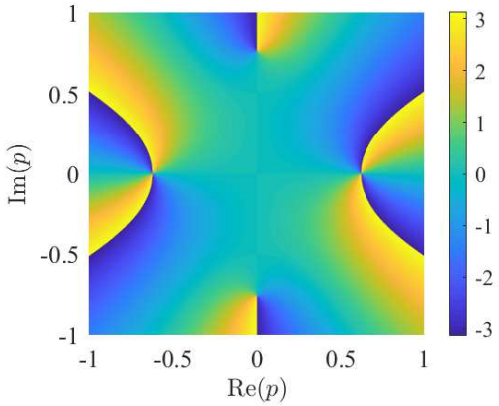

Fig. 2.1 Partial wave determinant of problem (2.17) between the shear and longitudinal velocities. Colour map denotes complex phase, solutions are points that appear to have all phase values.

The solutions are the zeros of this determinant, the colour map which denotes the complex phase of the determinant illustrates the location by solutions as the origins of curves of constant phase. Points from which two distinct sets of constant phase curves originate correspond to degenerate solutions of the eigenvalue problem. The behaviour of a partial wave changes as the p solutions transition from complex conjugate pairs into real solutions, see Figure 2.2.

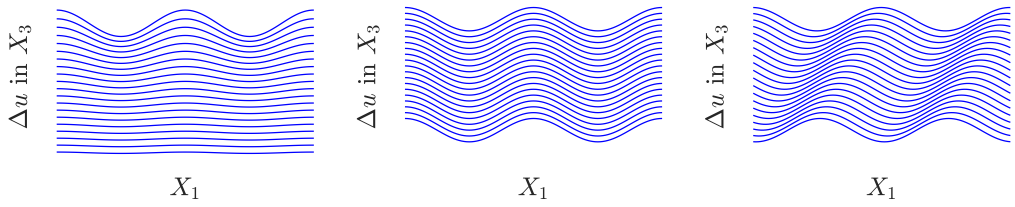

(a) $[k, 0, -\mathrm{i}k]$ (b) $[k, 0, 0]$ (c) $[k, 0, -k]$

Fig. 2.2 Change in partial wave displacement with the change in p unknown for a fixed real k value.

Figure 2.2 illustrates the change in behaviour of the partial waves with change in p unknown, which are dependent on the phase velocity. For isotropic cases, the change in p with the variation

of velocity always follows a well defined pattern. For low values of velocity the partial waves propagate in the imposed X_1 direction and with pure exponential decay in X_3, see Figure 2.2a. Increasing the phase velocity will cause the conjugate p pairs to move along the imaginary axis towards zero, the velocity values corresponding to point where $p = 0$ are called the bulk velocities. Bulk velocities are characterised by a pure propagation in X_1 and constant wave fronts in X_3, see Figure 2.2b. At $\mathrm{Im}(p) = 0$ each p solution from the conjugate pair splits and travel along the real axis towards positive and negative infinite. Now the partial waves given by this case no longer propagate in the X_1 direction but are rotated due to the nonzero $\mathrm{Re}(p)$, see Figure 2.2c.

The solution is assumed in the plane wave form, the wavefronts are prismatic in 2-dimensions, uniformal and constant in the propagating direction. Therefore, the propagation direction is normal to these plane waves, in which all points in the plane have the same wave phase [8]. In the case of Figure 2.2b, the plane waves may then be visualised as uniform surfaces in X_2-X_3, propagating in X_1. The SAW solutions, discussed in the following sections, are combinations of partial waveforms with exponential contributions, see Figure 2.2a. These are now plane-crested waveforms, prismatic in 1-dimension and complex-exponential in the other.

In elastic materials three bulk wave solutions exist, labelled the longitudinal or pressure (P), shear horizontal (SH) and shear veritical (SV) waves. In the isotropic case, the P wave displacement polarisaton vector is always in-line with the wave propagation vector. The displacement polarisation of the SH and SV waves, which correspond to the degenerate solutions, are in the tangent plane of the propagation vector. For anisotropic materials this may no longer be the case, except for choices of the propagation vector in directions of high symmetry. The P, SH and SV waves will favor displacement polarisation, which are no longer in-line with the chosen propagation direction, these waves are termed quasi-bulk [9]. An anisotropic stiffness, may be viewed as an isotropic stiffness with addition terms which deviate it from a uniform surface. As the anisotropic contributions tend to zero, the quasi-bulk solutions should approach the isotropic case, this concept is briefly investigated in Section 2.4.2 for SAW modes.

2.2.2 Rayleigh wave

The Rayleigh wave is a surface wave that can exist in a single isotropic material on a stress-free boundary, which causes decays into the depth of the material. Mathematically a uniform boundary splits the infinite space in half; the tractions on this surface must equal zero,

$$t_i = \sigma_{ij} n_j = 0. \tag{2.24}$$

The half-space material is connected to a vacuum for which no waveform may propagate, therefore the transmitted part of the waveform equals zero [9]. From Snell's law the condition is now,

$$C^{ijkl} n_j \left(\frac{\partial u_l^{(\mathrm{I})}}{\partial x^k} + \sum_{\mathrm{R}} \frac{\partial u_l^{(\mathrm{R})}}{\partial x^k} \right) = 0 \tag{2.25}$$

where the summation incident (I) and reflected (R) waves must equal on this boundary. In the isotropic case the incident longitudinal wave is reflected as a combination of longitudinal and shear waveforms. The ratio is dependent on the angle of incidence which is dependent on the bulk wave ratios of the material. The existence of the Rayleigh wave is a result of the interference of these waveforms at the stress-free boundary. The boundary conditions requires a linear combination of three of the six p partial waves which cause decay into the bulk, for decay in $X_3 > 0$ then $p < 0$ in (2.15),

$$u_i = \sum_{r=1}^{3} B_r u_i^r = \sum_{r=1}^{3} B_r A_i^r \mathrm{e}^{-\mathrm{i}k(\boldsymbol{m}\cdot\boldsymbol{x} + p^r \boldsymbol{n}\cdot\boldsymbol{x}) + \mathrm{i}\omega t}. \tag{2.26}$$

In this chapter only the behaviour of the resulting waveforms is discussed, implementation and solving boundary condition problems will be covered in Chapter 3. On a single boundary the Rayleigh wave exists for a single phase velocity and is non-dispersive, has a linear relationship between $\boldsymbol{k}$ and ω, therefore it exists for all wavenumber values [8]. In dispersive media, frequency is dependent on wavelength, and so the phase velocity is also dependent. For 3-dimensional anisotropic cases, the dispersion behaviour varies with propagation direction, this variation of the solution due to anisotropic is a type of dispersion. The Rayleigh wave exists below the bulk wave velocity, due to this the wave will always propagate along the surface X_1 and decay into the depth X_3. This can be visualised by considering a linear combination of three partial waves of the type shown in Figure 2.2a,

$$u = \mathrm{e}^{-\mathrm{i}k\boldsymbol{m}\cdot\boldsymbol{x}} \mathrm{e}^{k\boldsymbol{n}\cdot\boldsymbol{x}(p^1 + p^2 + p^3)} \tag{2.27}$$

Summating using p values in which $p < 0$ results in exponential decay in $X_3 > 0$ and pure propagation in X_1. The Rayleigh wave has an elliptical displacement pattern in the $X_1 - X_3$ plane that decays away from the boundary surface, see Figure 2.3.

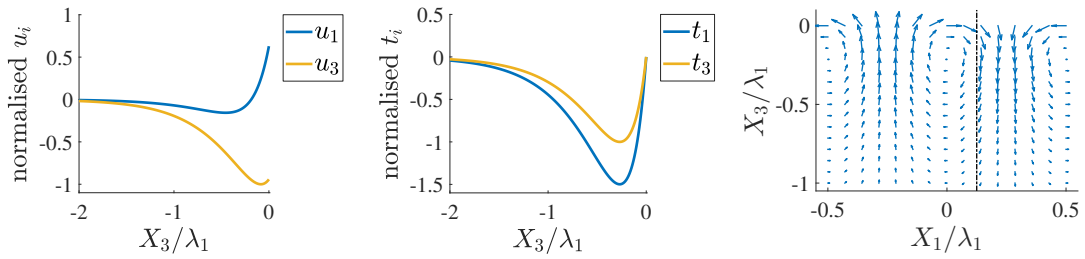

(a) Normalised u_i (b) Normalised t_i (c) Vector u_i

Fig. 2.3 Example displacements for the Rayleigh type wave in isotropic material. In (a) the displacements normalised to the maximum u_3 displacement, and in (b) the tractions normalised to the maximum t_3 traction. These are presented at $\frac{X_1}{\lambda_1} = \frac{1}{8}$, denoted by the dotted black line on (c), the half way point between maximum u_1 and u_3.

A leaky Rayleigh wave may also exist in isotropic materials [8, 10], the transition from Rayleigh to leaky is dependent on the Poisson ratio of the material. The surface wave can exist above the lowest bulk velocity of a material, which is coupled to a partial wave of the type shown in Figure 2.2c. The surface wave now propagates into the bulk of the material, due to the bulk propagating partial contribution, which causes energy leakage away from the surface. Leaky waves are discussed more in Chapter 4 along with their possible use in biosensor application.

2.2.3 Generalised anisotropic surface waves

The existence of surface waves in anisotropic half-spaces has been extensively researched, for a review of termology and wave types the reader is referred to [11]. The half-space problem is not the focus of this work but the existence of half-space waves is fundamental in the construction of multilayered waveforms. The transition states of a material are given by the velocities of the limiting bulk waves, (LBW) called the limiting velocities. The partial roots transition from complex to real values as previously discussed in Section 2.2.1. Now in materials with anisotropic stiffness, the transition does not have to occur at $p = 0$ but may occur at any point along the real axis. These states are key to characterising the behaviour of the waveforms, that can exist in both the half-space and multilayered problems. SAW solutions in the so-called subsonic region are constructed from a linear combination of two or three partial waves, which exponentially decay into the bulk of the half-space material, Figure 2.2a. SAWs in the supersonic region are now some linear combination of two partial waves and a bulk propagating wave, Figure 2.2c, these solutions are generalised Rayleigh waves, leaky surface waves or in some special material cases only consist of one-component.

Recent research into SAWs in half-space geometry have focused on more complicated materials. These problems require the constant development of mathematical and numerical tools to handle mutliferroics, inhomogeneous behaviours and energy dissipation. Models for materials in biomechanical research need to handle forms of inhomogeneous and viscoelastic behaviour [12, 13]. In addition to these forms, the saturation due to water content must be considered for models in solid mechanics [14, 15], important for geophysical applications. Multiferroic materials in which the mechanical fields are coupled to electromagnetic and thermal fields are also an ongoing area of research [16–18].

2.3 Multilayered Waveforms

The main focus of this thesis is on cases in multilayered geometry, the half-space problem is only of interest in understanding the wave existence problem in the layered case. The numerical approaches for computing multilayered solutions also differ from those that would be developed in half-space cases. In this section only the physical behaviour is discussed, the mathematical model along with the numerical solution is developed in Chapter 3.

2.3.1 Mutlilayered geometry

The model used throughout this work is the layered half-space, with the number of layers varying with the problem, see Figure 2.4. The half-space boundary is numerically easier to resolve than SAWs in a plate geometry which would require short wavelengths, resulting in numerical large numbers. In the real world semi-inifinite boundaries do not exist, but at high frequencies the first propagating symmetric and anti-symmetric plate modes coalesce into the Rayleigh wave [19]. At the interfaces between materials it is required that the displacements and tractions of each material are matched. The fully bonded layers at the boundary use all displacements and tractions in the condition. A reduced set of conditions would capture slipping motion of a sliding contact in a particular shear direction [20]. At the surface, the stress-free boundary condition is the most relavent to biosensor design for propagating SAW modes. Alternatively, a clamped boundary condition may be used, which is the displacement free boundary condition, these conditions are typical used for plate modes [8].

The stroh vectors allow for the rotation of the entire multilayer structure, it is also a requirement to be able to rotate each layer individually. The stiffness tensor may be rotated using a combined transformation for fourth rank tensors [21], requiring three angle rotation [22] to

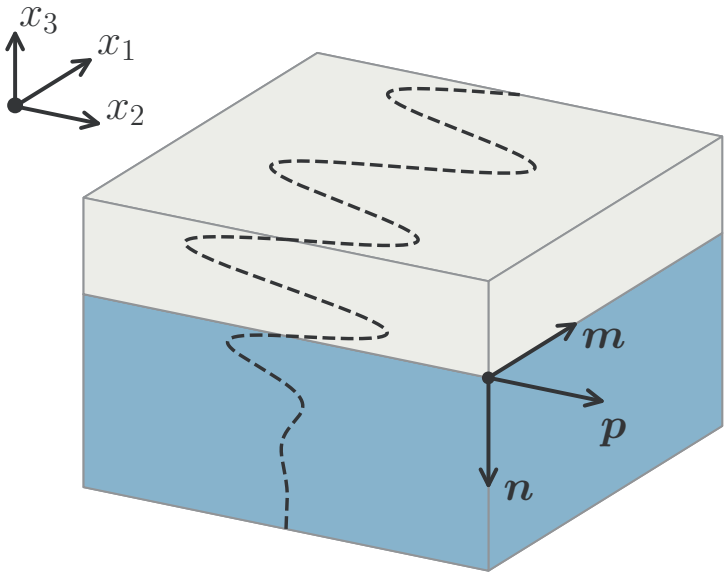

Fig. 2.4 Illustration of a single layered half space with an isotropic Love wave solution, additional layers may be added in the boundary conditions. The orthogonal vectors $\boldsymbol{m}$ (propagation) and $\boldsymbol{n}$ (normal to the layer surfaces) are, in this case, aligned to x_1 and x_3 respectively, but may be freely rotated in the coordinate system.

recover all possible materals cuts. Although three angles are required for computing all possible cuts, only two angles are required to compute all possible points on a sphere. When the aim is to compute data for all possible cuts of a material, the additional computations are redundant. In these cases it is numerically more efficient to compute extra points in the two angle case and average the third angle using a coordinate minimising method. It is important to note that this is only the case for specified propagation directions, for example bulk waves, three angles must for all possible m_j and n_j combinations.

2.3.2 Layered isotropic waveforms and Love waves

The three main types of SAW that can exist in layered isotropic media are the Love, Rayleigh and Stoneley [23]. The Stoneley wave is an energy leaking Rayleigh type SAW which is typically associated with fluidised cases, therefore details on this SAW are covered in Chapter 5. The Love wave exists in the layered half-space geometry between the bulk velocities of the layer and substrate, formally,

$$v_{Layer} < v_{Love} < v_{substrate} \tag{2.28}$$

shown by the analytic solution [8]. The displacement is in the form of a one component in-plane shear, which propagates and resonates through the thickness of the layer and decays into the bulk of the substrate. The Love wave can be viewed as a thickness shear plate mode with a stress-free boundary condition that is replaced by a interface condition with a half-space. As with the plate geometry the Love wave is a dispersive waveform, the cut-off frequency for the plate case is removed by the presence of the substrate, which also breaks the symmetry of the shear mode. See Figure 2.5 and 2.6 respectively for the displacements and tractions of the first three modes.

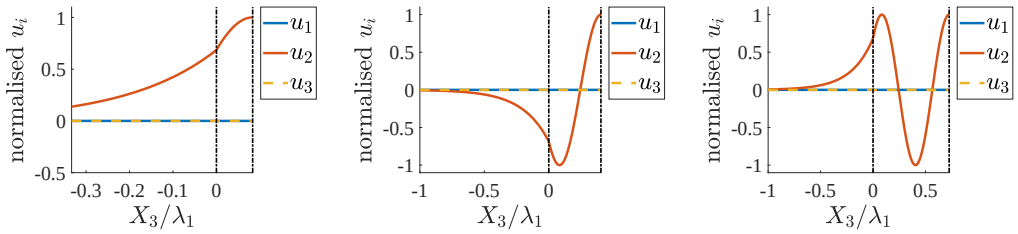

(a) 1st mode (b) 2nd mode (c) 3rd mode

Fig. 2.5 Displacements for the first three modes of the Love type solution in an isotropic layered half-space. Normalised to the maximum u_2 displacement, dotted black line denotes interface and free surface boundaries, interface at $X_3 = 0$.

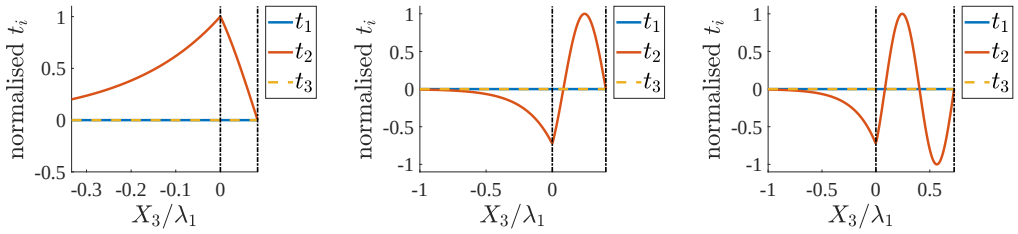

(a) 1st mode (b) 2nd mode (c) 3rd mode

Fig. 2.6 Tractions for the first three modes of the Love type solution in an isotropic layered half-space. Normalised to the maximum u_2 displacement, dotted black line denotes interface and free surface boundaries, interface at $X_3 = 0$.

The half-space Rayleigh wave can be viewed as the smooth transition of symmetric and anti-symmetric Lamb plate mode from plate geometry to half space geometry [8, 24]. The transition can be visualised by either increasing the thickness of plate towards infinity or by decreasing the wavelength of the plate modes. The behaviour can be seen on the dispersion plot [25], symmetric and anti-symmetric parts of the lamb modes coalescence due to the removal of the second boundary at these limits. Therefore multilayered Rayleigh waves, can also be viewed in the same way as Love waves, but now the second boundary of the Lamb modes

solution is being replaced with a half-space interface condition. Unlike the Love wave they may exist under the bulk velocity of the layer material, similar to their half-space counter parts. Multilayered Rayleigh waves are also dispersive waveforms, see Figure 2.7 and 2.8 respectively for the displacements and tractions of the first three modes.

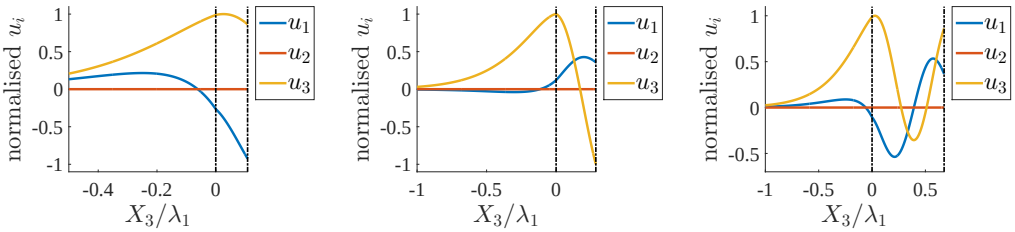

(a) 1st mode (b) 2nd mode (c) 3rd mode

Fig. 2.7 Displacements for the first three modes for Rayleigh type solution in layered isotropic half-space. Normalised to the maximum u_3 displacement, dotted black line denotes interface and free surface boundaries, interface at $X_3 = 0$.

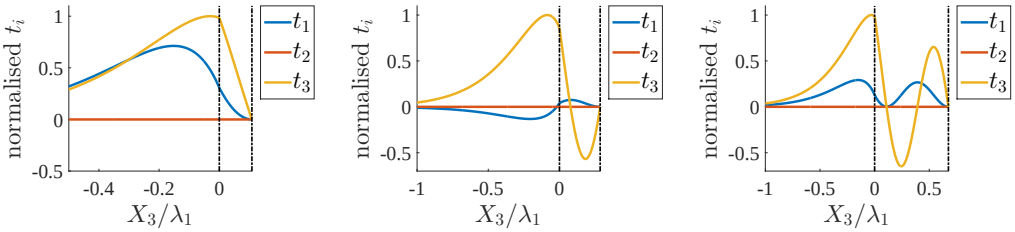

(a) 1st mode (b) 2nd mode (c) 3rd mode

Fig. 2.8 Tractions for the first three modes for Rayleigh type solution in layered isotropic half-space. Normalised to the maximum u_3 displacement, dotted black line denotes interface and free surface boundaries, interface at $X_3 = 0$.

2.3.3 Generalised multilayered surface waves

The anisotropic layered half-space problem has long been studied in the geophysical field but unlike the half-space problem the literature is still lacking outside of a few well studied cases. Some examples in the biosensor focused applications include ST-cut and AT-cut quartz [26–30] and Y-cut lithium niobate [31–33]. The layered problem has a vast increase in the possible combinations of materials with anisotropy stiffness and is not limited to only a single layer for many applications. Multilayered structures also contain more wave types in both the Rayleigh and Love waves, though as mentioned in the isotropic case the well studied half-space and plate geometries can help predict behaviour.

A main difference between the isotropic and anisotropic cases is the possibility of Rayleigh and Love displacement coupling [34, 35]. The coupling is due to the interaction of the quasi-bulk solutions with the material boundaries, SV wave may excite SH waves. Combinations of different anisotropy materials can impose coupling at the interface. Due to this coupling the line between Love and Rayleigh waves becomes blurred, with some cases of near degeneracy having been shown. The naming convention of these waves becomes problematic, throughout this work the waveforms will be defined by the partition of Love and Rayleigh parts, distinguished using the bulk solutions. The consequences of such coupling for biosensor applications is discussed in detail in Chapter 6 in the case of fluid energy loss. Figure 2.9 shows an example of displacements of a generalised multilayered SAW, notice the elliptical Rayleigh type motion in (a) and the SH wave motion in (b).

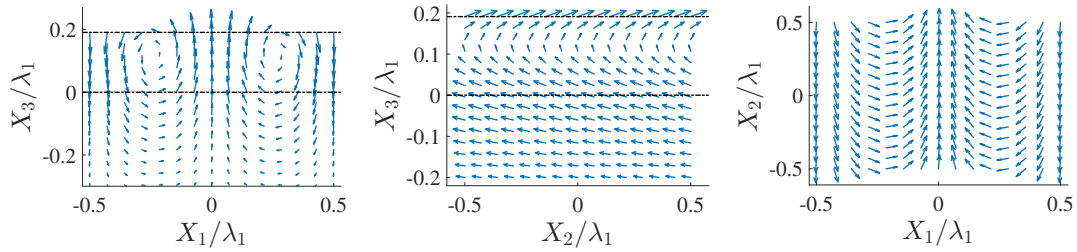

(a) $X_2/\lambda_1 = 0$ (b) $X_1/\lambda_1 = 0.25$ (c) $X_3/\lambda_1 = 0$

Fig. 2.9 Displacement vector plots for generalised anisotropic multilayered SAW mode, for the case of cubic on cubic meeting the condition for Love wave existence. Both stiffness tensors rotated at an angle of $\theta = \frac{\pi}{8}$ in the plane of the surface.

2.4 Layer Compatibility and Symmetry

In this section the concept of anisotropic compatibility between layered anisotropies with differing symmetries is introduced. Also the anisotropic factor is also introduced as a tool to be used in layer chapters, examples of anisotropic problems will be presented. For this section the material used were silicon, quartz [9] and copper [36].

2.4.1 Layer compatability

Plane bulk wave solutions can provide insight into wave types that may exist within materials, and require little computational cost. In the previous sections, it was shown that the behaviour of composite waveforms can be predicted using the partial waves. In anisotropic materials these partial waves are dependant on the propagation direction within the cut of a crystal. Inspecting

the bulk velocity surfaces of multiple materials relative to each other, can provide insight into the compatibility of the material combinations.

The definition of compatibility is dependent on the desired output, throughout this thesis a higher cyclic symmetry is of importance. Therefore, the compatibility is defined as the ratio between the lowest common symmetry and the contributing symmetry of interest for the comparison. The bulk wave velocity curves are a good measure of the symmetry of a particular crystal cut. The compatibility between the relative symmetries of the materials is important for consistent wave behaviour with the propagation angle, see Figure 2.10.

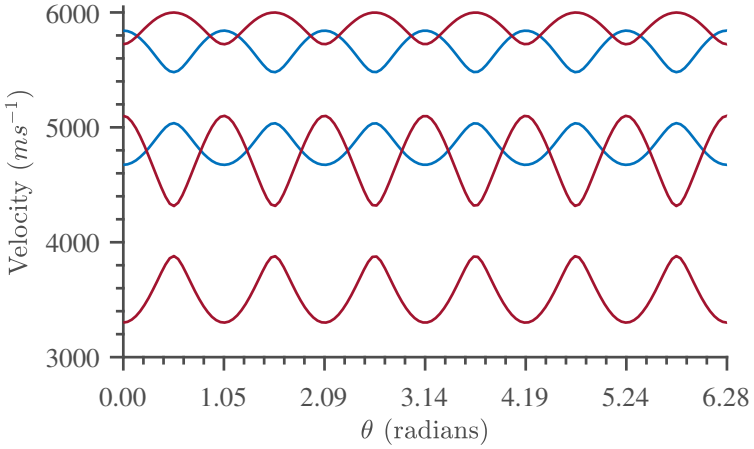

Fig. 2.10 Bulk velocities of Z-cut Quartz (red) and quasi-shear velocities of silicon cut in (111) miller index notation (blue).

The cubic and trigonal symmetries have the lowest common symmetry of 2-fold, when high symmetry directions are aligned in a multilayered combination. Trigonal has 3-fold symmetry, but for Z-cut quartz the symmetry many be assumed as quasi-6-fold. In Chapter 5 a case is presented in which this 6-fold assumption breaks down. In Chapter 6 the effect of the compatibility on shear dominant and Rayleigh dominant waveforms is explored in more detail. This will be investigated between cases of high and low compatible cuts of silicon with a quartz layer.

The intersection of bulk wave velocity curves at particular angles creates new transition regions. Transition regions are defined, in this work, as the section of the bulk velocity curve between intersection points which create bounded areas. These areas that are bounded by the bulk wave velocity curves may have unique behaviours, see Figure 2.10 close to 4900ms^{-1}. Plane wave rotation in this cut, at a fixed velocity, may cycle between several unique areas. The changing partial waves between the two materials may result in leaky solutions at particular directions, and between different layers. This is a prediction of the behaviour based on bulk solutions, the transition may in fact be dependent on the lowest bulk velocity values, due to the

3-dimensional anisotropy of SAW existence theory. Therefore, SAWs around these transition regions are of interest for further study, to be investigated in Chapter 4.

The definition presented here for compatibility only considers the lowest common symmetry for bulk wave velocity curves, this definition could be expand. For example, combinations for desired wave types, an example of this is the Love wave which has the requirement on the relative bulk wave velocities (2.28). This can vary with the propagation angle due to the crossing of bulk wave velocity curves, altering the portion of Love wave to leaky wave within the cut. In some cases the desired wave type may be one that changes from non-leaky to leaky, in such a case it would be desirable to have a particular number of crossing points of the bulk velocity surface. Depending on the bulk waves which overlap, new lossy regions may be created, this is part of the investigation of Chapter 4.

2.4.2 Isotropic to cubic transition

The coefficients of the stiffness tensor describle the shape of the anisotropy, for the crystal classes [37] these shapes are symmetric. Another way of describing the anisotropy of highly symmetric materials is to use anisotropic factors which weigh the change in stiffness parameters between points. Cubic materials are one of the simplest symmetries only requiring one additional stiffness coefficient, than the isotropic case which means only one anisotropic factor is required, see Figure 2.11.

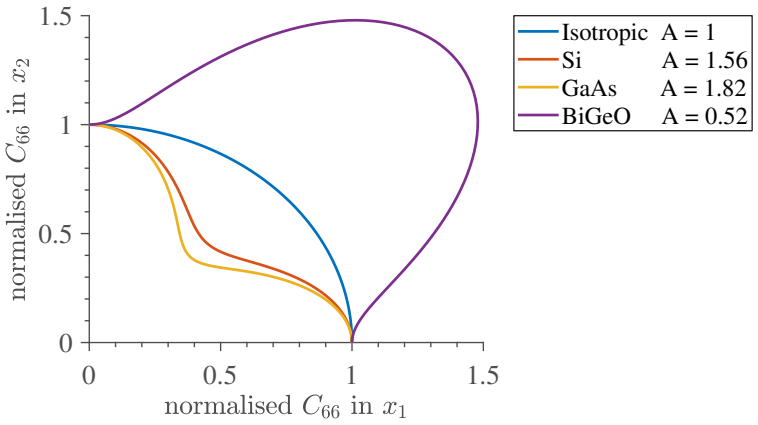

Fig. 2.11 Variation of C_{66} stiffness coefficient in vogit notation by fixing coordinate system and rotating the stiffness tensor in the $x_1 - x_2$ plane.

The anisotropic factor is another tool that may be used to help predict and further classifiy the behaviour within crystal symmetries. An example is the use in the half-space existence problem of Rayleigh and generalised Rayleigh waves [9]. For the cubic materials presented in Figure 2.11

the change in anisotropic factor causes the stiffness coefficients, in this case C_{66} in vogit notation, to increase or decrease.

The anisotropic factor can also be used in investigating the change of a wave property with anisotropy, this is used in Chapter 6 to compare isotropic and ansiotropic substrates. The use of the factor will be shown here, by considering the problem of changing wave structure with transition of a material, from isotropic to cubic by increasing the anisotropic factor, see Figure 2.12. The modes start with the isotropic form at $A = 1$, for mode one and three the structure instantly becomes cubic in shape at $A = 1.2$, mode three sees a gradual change up to $A = 1.8$ to cubic structure.

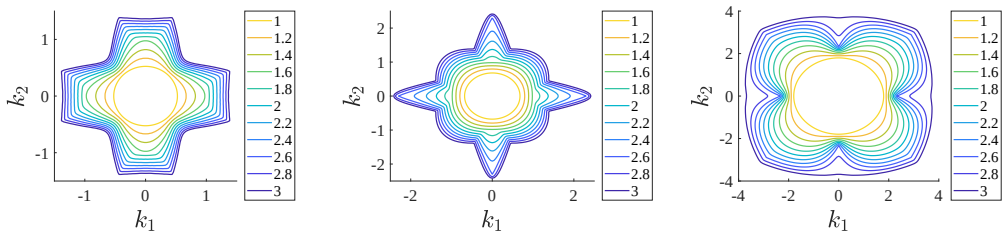

(a) 1st Mode (b) 2nd Mode (c) 3rd Mode

Fig. 2.12 The first three modes for the layered half-space case, the anisotropic factor is varied for both materials at the same rate. The materials are copper layered on silicon which is compatible for isotropic Love wave propagation, velocity fixed at 3000ms^{-1}. Colour map denotes anisotropic factor.

On inspection of Figure 2.12 it would seem at first glance that the plots are incorrect at higher values of A in particular regions. The sudden shift in behaviour could be seen as incorrect resolution of crossing points between the modes 2.12a and 2.12b and modes 2.12b and 2.12c. Infact these are cases in which the wavenumbers of two modes converge onto a point at a particular anisotropic factor value, the mode remains smoothly continuous before and after, see Figure 2.13.

In Figure 2.13b the modes have both a Rayleigh dominant and a Love dominant range in the cut, this is what causes the change in shape at approximately $\frac{\pi}{4}$. The behaviour of each mode switches with each other after the degenerate points, the modes take on the same displacement pattern at these points. Therefore, for anisotropic combinations, points of idenitical or near idenitical wave solution may exist for multiple modes, further illustrating the move away from isotropic wave descriptions. The change in anisotropic factor will shift the bulk wave solutions altering the structure of the problem, a full description of the behaviours would require a third dimension for velocity to generate anisotropic cylinders. In addition, the problem may be viewed

in two angle rotations, Figure 2.14 shows the same degenerate point from 2.13b in two angles by 2-dimensional surfaces touching at a point.

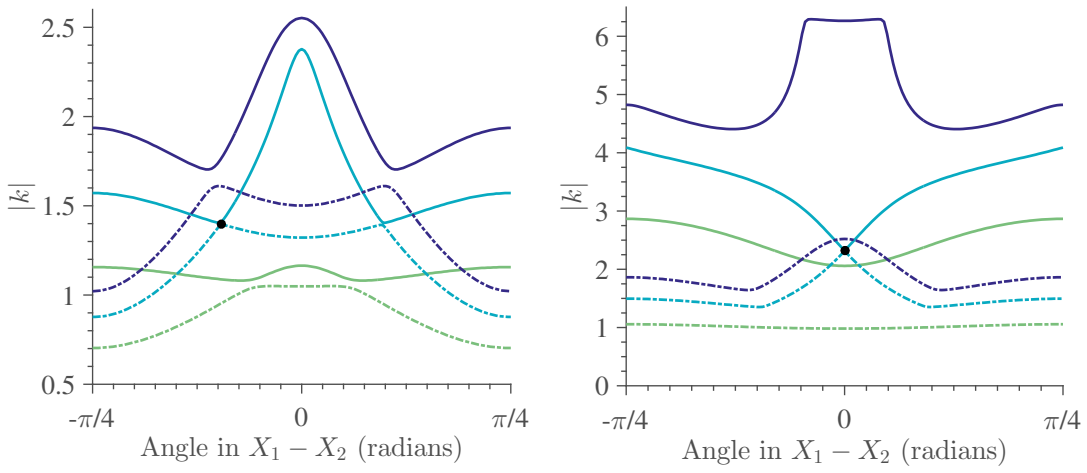

(a) 1st and 2nd Modes

(b) 2nd and 3rd Modes

Fig. 2.13 The convergence of the wavenumber of two modes onto the same point with change in anisotropic factor. In (a) point occurs at $A = 2.8$ and in (b) at $A = 2.6$, modes are distinguished by the solid and dashed lines, with the colour map denoting fixed A-factor values.

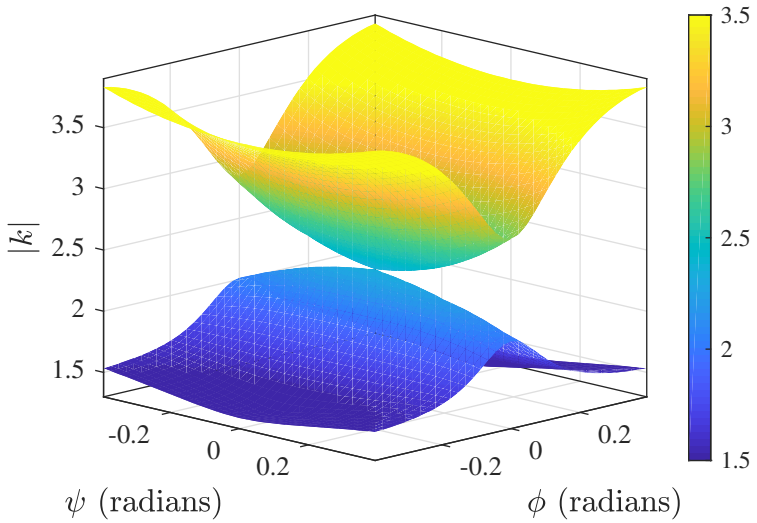

Fig. 2.14 The point shown in Figure 2.13b, now in two angle rotations in the $X1 - X2$ and $X2 - X3$ planes. Colour map denotes magnitude of wavenumber.

2.5 Standard Test Cases

Several standard cases will be considered based on the commonly used materials, feasibility of material combinations and the symmetry of the anisotropy, see [9] for material data. These cases will be used primarily in Chapter 4 to 6 when considering forms of SAW energy loss in layered

anistropic materials. The variation of piezoelectric coupling around the chosen cuts is also a key consideration for the excitation of these waveforms. Along with the thermoelastic properties for minimising energy loss, to be further discussed in Chapter 7.

2.5.1 Bulk slowness surfaces

In section 1.2.2, a selection of commonly used materials for biosensor application were reviewed. For several of these materials the bulk wave velocity surfaces are presented for several cuts of interest using only the mechanical properties. Lead zirconate titanate (PZT) and Zinc oxide (ZnO) are both part of the hexagonal crystal class, therefore these materials have a transverse isotropic plane which is the Z-cut. The bulk wave velocities do not change in this plane just as with an isotropic medium but the two shear velocities have distinct values due to the anisotropy. For PZT the Z-cut longitudinal and shear velocities are approximately 4305ms^{-1}, 2017ms^{-1} and 1848ms^{-1} , for ZnO the Z-cut longitudinal and shear velocities are approximately 6077ms^{-1}, 2795ms^{-1} and 2737ms^{-1}. Presented in Figure 2.15 and 2.16 are the X-cut bulk wave slowness of PZT and ZnO respectivitly, which have the same structure as the Y-cut due to the crystal symmtries. The slowness of ZnO is consistent with the literature [9, 38].

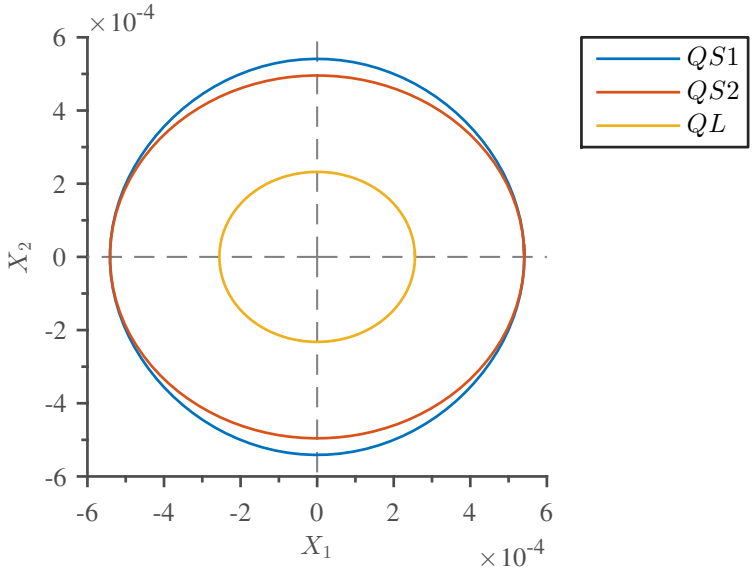

Fig. 2.15 Slowness surfaces for the quasi-shears and quasi-longitudinal bulk waves of X-cut PZT.

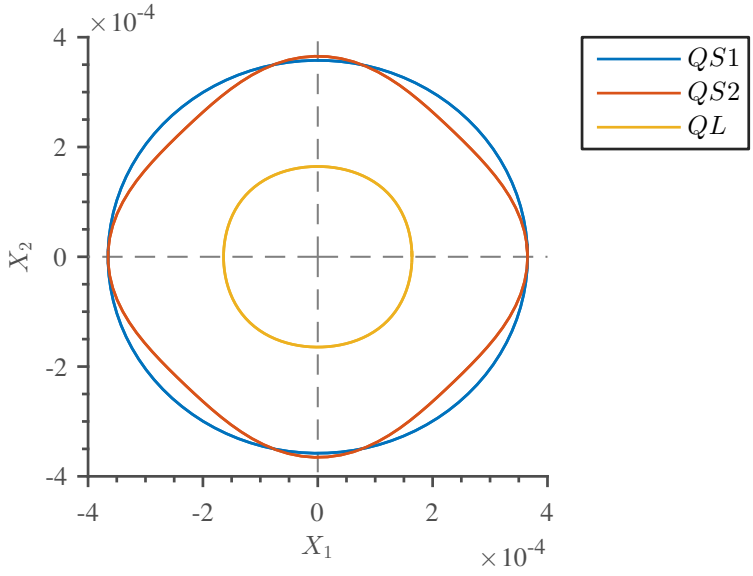

Fig. 2.16 Slowness surfaces for the quasi-shear and quasi-longitudinal bulk waves of X-cut ZnO.

For trigonal crystals quartz and lithium niobate ($LiNbO_3$) the Z-cut has the most symmetry with a quasi-6-fold axis cyclic symmetry. Presented in Figure 2.17 and 2.18 are the Z-cut bulk wave slowness of quartz and $LiNbO_3$ respectively. The variation of the velocities around the Z-cut of $LiNbO_3$ are much less than quartz, due to this $LiNbO_3$ is more attractive for biosensor designs that use cyclic degenerate modes. The maximum variation in velocities around the Z-cut quartz are approximately 576ms^{-1}, 782ms^{-1} and 277ms^{-1} for the lowest shear, highest shear and longitudinal bulk wave velocities. Opposed to Z-cut $LiNbO_3$ where the maximum variations are approximately 110ms^{-1} for the two shear waves and 10ms^{-1} for the longitudinal wave. The slowness surface of Z-cut Quartz is consistent with the literature [38, 39].

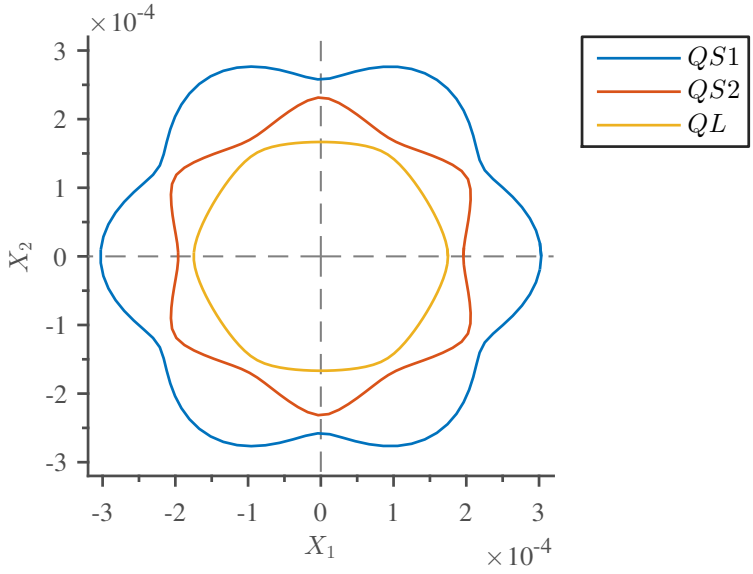

Fig. 2.17 Slowness surfaces for the quasi-shears and quasi-longitudinal bulk waves of Z-cut quartz.

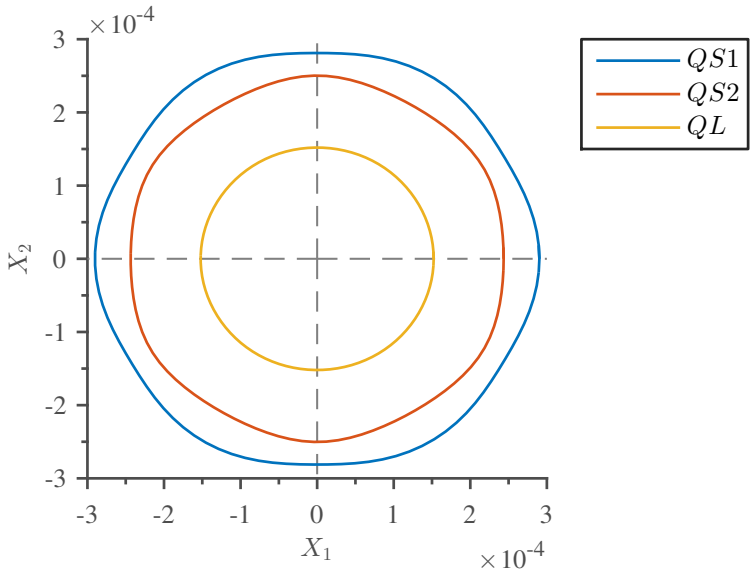

Fig. 2.18 Slowness surfaces for the quasi-shears and quasi-longitudinal bulk waves of Z-cut $LiNbO_3$.

Other common cuts for these materials are chosen for biosensor application, due to their electrical or thermal properties. Traditionally SAW biosensors make use of propagating waves in 1-dimension and so the symmetry of the cut is not as important. The bulk wave slowness of AT-cut quartz is presented in Figure 2.19. Another common cut for SAW devices is ST-cut which bears similar symmetry structure to AT-cut due to only a 7.75°difference in rotation angle from Z-axis in the Y-cut of quartz.

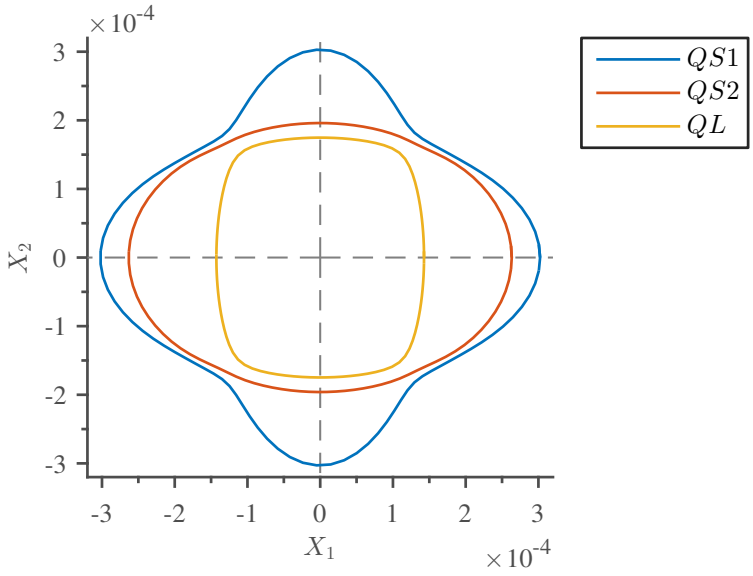

Fig. 2.19 Slowness surfaces for the quasi-shears and quasi-longitudinal bulk waves of AT-cut quartz.

Cubic crystals in the Z, X and Y-cuts have 4-fold cyclic symmetry which are the cuts with the highest symmetry. The bulk wave slowness for Z-cut cubic silicon is presented in Figure 2.20. Slowness surface for Z-cut silicon is consistent with computed literature [9, 40].

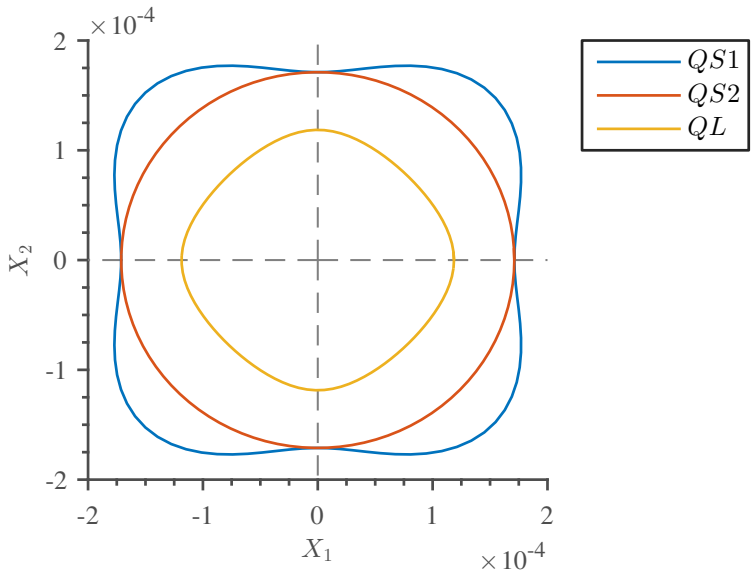

Fig. 2.20 Slowness surfaces for the quasi-shears and quasi-longitudinal bulk waves of Z-cut silicon.

The highest cyclically symmertic cut does not mean that it has the lowest solution variation, for silicon the so called isotropic cut has the lowest variation. In reality this cut has 6-fold symmetry, visualised by a 2-dimensional hexagonal plane slotted at an angle inside a cube, similar to the Z-cut of trigonal crystals. The bulk wave slowness of this cut for silicon is presented in Figure 2.21 denoted in miller indices as (111).

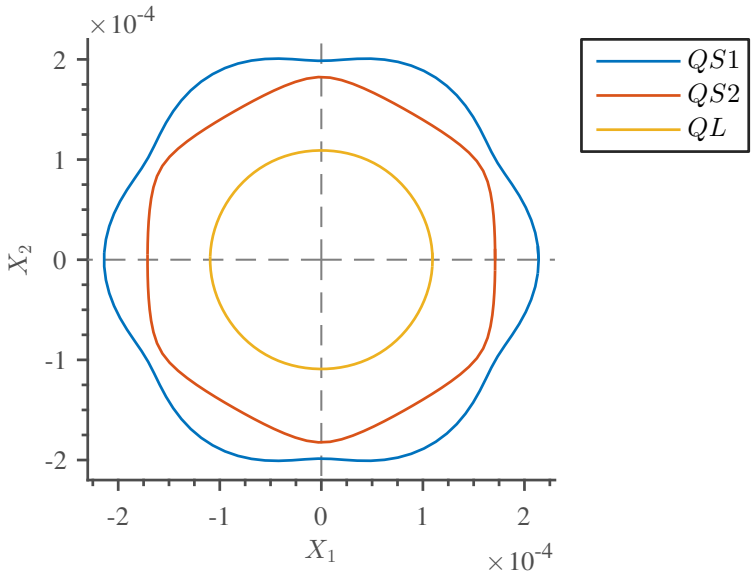

Fig. 2.21 Slowness surfaces for the quasi-shears and quasi-longitudinal bulk waves of (111) silicon.

The longitudinal bulk wave has a variation of approximate 30ms^{-1}, the shears are larger, around 360ms^{-1}, due to the cubic structure.

2.5.2 Material combinations

For the materials cuts presented in Section 2.5.1 several combinations were considered for standard test cases. The interest, at this stage, is placed solely on the anisotropy of these crystal cuts and the affect it will have on mechanical SAW propagation. In Section 2.4 the concept of layer compatibility was used with the case of Z-cut quartz on (111) silicon, in Figure 2.10. For quartz on silicon the crossing of bulk wave solutions gives rise to extra regions of behaviour, which is of interest for the study of leaky waveforms. For $LiNbO_3$ on silicon in Figure 2.22 this is not an issue, this and the lower variation in bulk solution of $LiNbO_3$ leads to a highly compatible combination. The symmetries of quartz and silicon in Figure 2.10 have the same 6-fold cyclic symmetry and the cuts are in-line. It is predicted that this will lead to a more consistent displacement form of plane wave propagation, as a function of the propagation angle due to interactions at the interface. In constrast Figure 2.23 shows Z-cut Quartz with 6-fold cyclic symmetry on Z-cut silicon that has 4-fold cyclic symmetry. The differing symmetries is expected to have an effect on the consistency of generalised displacements around the cut, along with the new overlapping of quasi-shear solutions. This overlapping is interesting for firstly, the possible angle dependent generation of leaky SAWs, and secondly for the comparison of Rayleigh type and Love type displacements around the cut between the two layers.

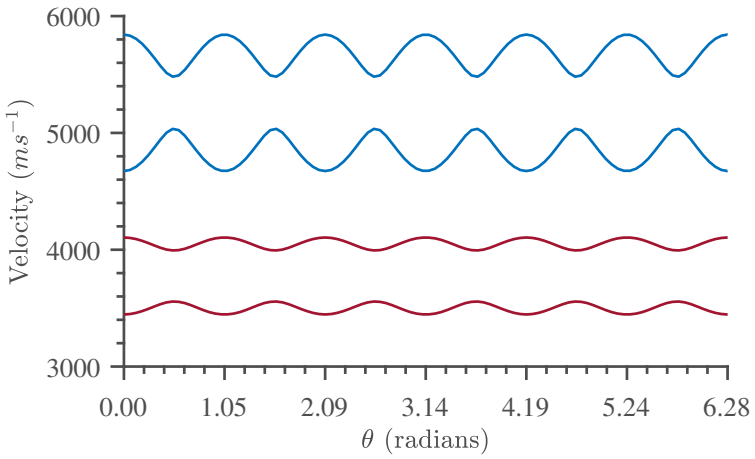

Fig. 2.22 Quasi-shear velocities of Z-cut $LiNbO_3$ (red) and silicon cut in (111) miller index notation (blue).

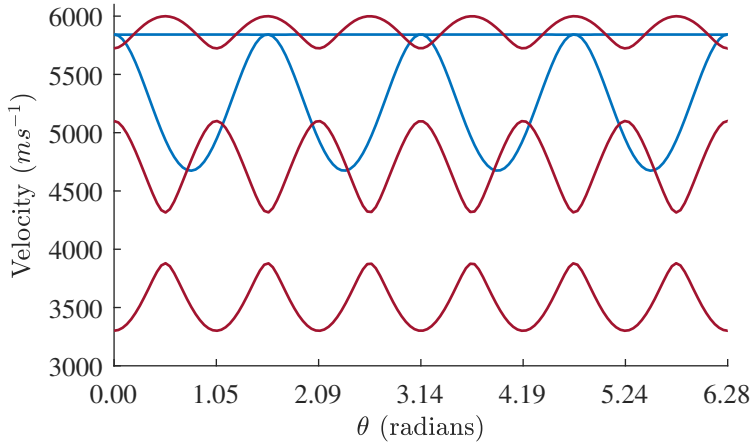

Fig. 2.23 Bulk velocities of Z-cut Quartz (red) and quasi-shear velocities of Z-cut silicon (blue).

AT-cut quartz has a number of advantages which were discussed in the previous sections, the symmetry of this cut is low as shown in Figure 2.19. Even though the lowest quasi-shear of AT-cut quartz has 2-fold cyclic symmetry it is close to 4-fold cyclic symmetry similar to the lowest quasi-shear of Z-cut silicon. Figure 2.24 presents the comparison between AT-cut quartz and Z-cut silicon, the current relative rotations put the quasi-shears of quartz below silicon with touching points. For the lowest quasi-shears of the two materials to be in-line, would require a rotation of $\frac{\pi}{4}$ causing additional overlay of bulk velocities.

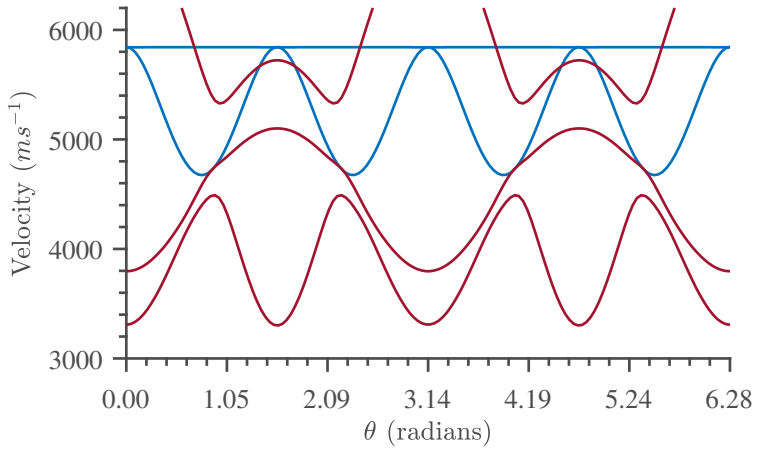

Fig. 2.24 Bulk velocities of AT-cut Quartz (red) and quasi-shear velocities of Z-cut silicon (blue).

Quartz and $LiNbO_3$ have the same trigonal stiffness symmetry, but due to the overlapping of the lowest quasi-shear solutions the materials are not compatible, see Figure 2.25 and 2.26. It has been shown that these materials may be bonded together, but this is not benefical outside of linear devices that take advantage of plane wave propagation and resonance.

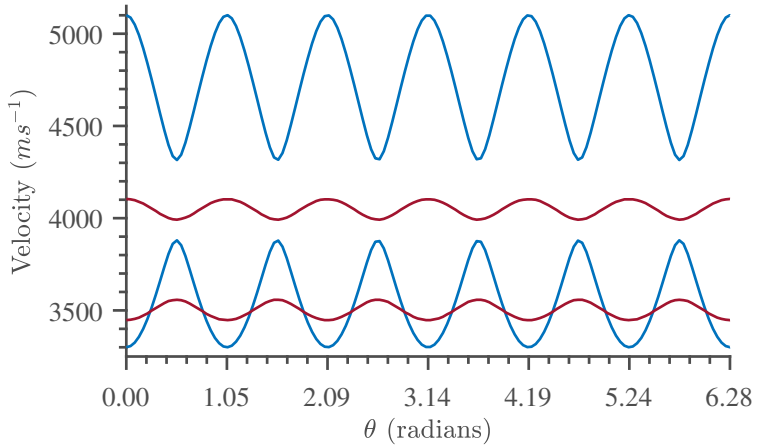

Fig. 2.25 Quasi-shear velocities of Z-cut $LiNbO_3$ (red) and Z-cut quartz (blue).

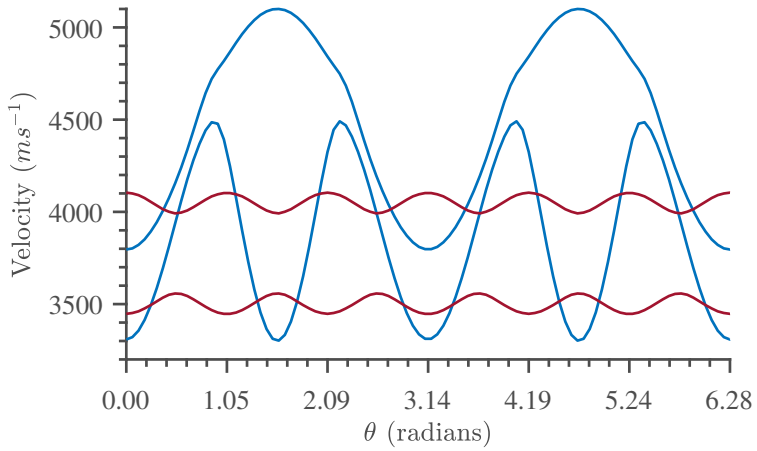

Fig. 2.26 Quasi-shear velocities of Z-cut $LiNbO_3$ (red) and AT-cut quartz (blue).

Piezoelectric materials such as PZT, ZnO and AlN are desirable in circular sensor design due to their transverse isotropic plane. The study of the interaction of these hexagonal crystals with other crystal symmetries, may be of interest along with the energy loss in other polycrystals. SiO_2 benefits from being isotropic, the use of an isotropic waveguide layer on an ansiotropic substrate could reduce energy loss through out-of-plane displacements at the fluid/solid interface. Isotropic and hexagonal waveguides are also of interest for reducing the rotation variation of the overall composite SAW wave, this is dependent on the relative energy partition between layers. For cases of leaky wave propagation, the substrate material would take a more active role in the dynamics, and the cyclic symmetry of the substrate would influence the slowness of the SAW solutions. These cases are of interest for both energy loss mitigation and development of novel biosensor concepts taking advantage of the changing cyclic symmetry.

2.5.3 Piezoelectric coupling

For piezoelectric materials, the coupling between the mechanical and electrical properties can lead to a change in structure of the bulk wave solutions. This change in bulk wave value and structure is dependent on the piezoelectric tensor, see Appendix B for the piezoelectric thermoelastic formulation. The piezoelectric tensor shows which electric fields are linked to which stresses, describing how mechanical waves may be excited by interdigital transducers. Quartz is a piezoelectric 32 trigonal crystal class, the change in bulk wave velocities for Z-cut and AT-cut are presented in Figure 2.27 and Figure 2.28. For quartz, the change in the bulk wave velocities due to the piezoelectric coupling is small. Due to this it is expected that the error in using the mechanical solutions should be insignificant.

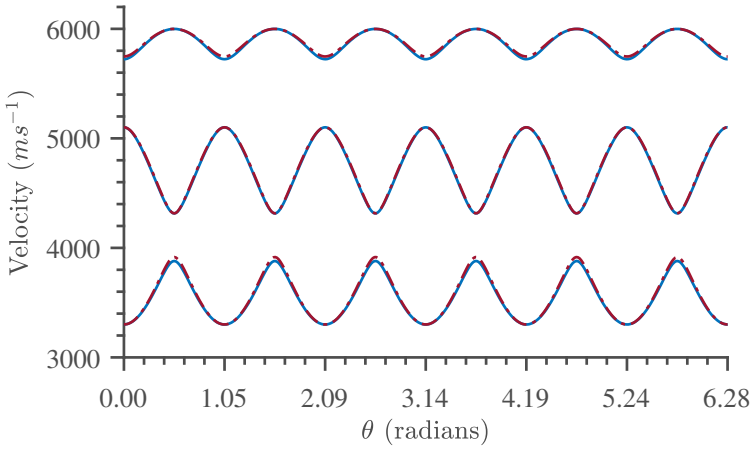

Fig. 2.27 Comparison of quasi-bulk velocities of Z-cut quartz, between mechanical solid-line blue and piezoelectric dotted-line red.

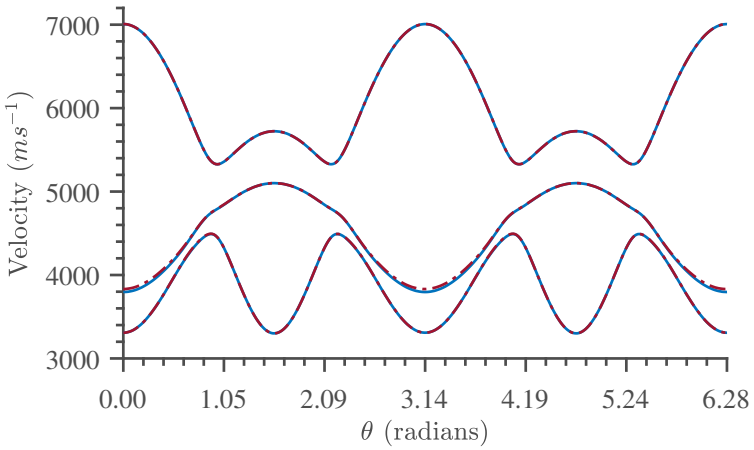

Fig. 2.28 Comparison of quasi-bulk velocities of AT-cut quartz, between mechanical solid-line blue and piezoelectric dotted-line red.

Lithium niobate is also piezoelectric triganol but of the 3m class, with a completely different piezoelectric tensor structure. The piezoelectric coefficients are also larger than quartz, the change in bulk wave velocities for the Z-cut are presented in Figure 2.29.

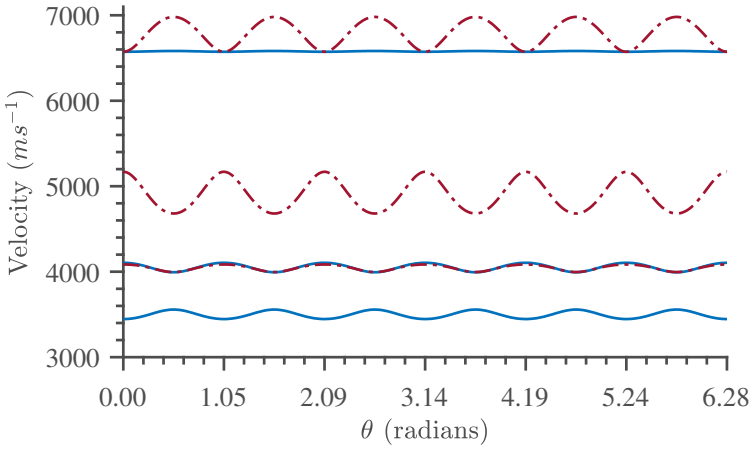

Fig. 2.29 Comparison of quasi-bulk velocities of Z-cut $LiNbO_3$, between mechanical solid-line blue and piezoelectric dotted-line red.

The change in the bulk wave velocities in lithium niobate is much greater than the changes seen in quartz. The symmetry still remains 6-fold but the quasi-shear solutions are now at a different value and the quasi-longitudinal has non-zero change with angle. The change in value of the bulk wave solutions will change the location of existence regions for types of multilayer surface wave solutions. Depending on the material combination, this could alter the location of leaky transitions and may even remove regions of purly mechanical quasi-Love wave propagation. The effects differ for each of the bulk wave velocities, this implies that the affect of piezoelectric coupling may be different for types of surface modes. The error between

mechanical and piezoelectric SAW solutions will be studied in Chapter 7, in which the impact on annular transducer design will be discussed.

2.6 Conclusions

The fundamental knowledge of the mathematical models and physical behaviour for 3-dimensional elastic SAW modes have been outlined. The problem has been formulated using the traditional tensor calculus approach, in complex vector space which is essential for later chapters. The operator for the elastic wave problem is shown to be Hermitian, as expected for a system that is expected to conserve energy. A brief review of the physics of half-space and multilayered SAW solutions has been presented. The underlying partial waves that combine to create these composite waveforms are key in understanding the structure of these waveforms.

For multilayered waveforms, the concept of compatability between the properties of the layers has been introduced. The location of the bulk waves in relation to the bulk waves of other layers provides insight into how these layers will interact with each other. From the bulk wave solutions the multilayered waveform may be predicted, this can be used to tailor which layers will be dynamically active. The problem is complicated further by the anisotropy of the layers which may now cause overlapping of bulk wave velocity surface, it is predicted that these will give rise to new transition regions. These regions may have waveforms with different structures which smoothly transition from previous regions of solutions. Combining this behaviour with the dispersive nature of multilayered waveforms leads to many variations of the problem, which require inspection in later chapters.

The anisotropic A-factor is introduced as a method of scaling the anisotropy, altering the structure of the crystal based on the isotropic values. The number of A-factors required is dependent on the number of independent stiffness coefficients, leading to many degrees of freedom outside of the simple cubic case. A case of two cubic crystals, with differing properties, in the layered half-space geometry is presented, cuts that align the anisotropies are chosen. The main point from this analysis is that the generalised versions of the Love and Rayleigh waves are coupled to each other, this coupling is dependent on the propagation angle. In special cases the modes take on the same solution, at these points the waveforms take on the exact same structure. For bisosensor application the main interest lies in the excitation of these generalised modes, the coupling may now allow excitation of waveforms through other displacements.

The bulk waves and some combinations, have been computed for several anisotropic materials of interest for biosensor application. A case of interest is trigonal Z-cut quartz on silicon Z-cut,

for the transition problem, and isotropic cut due to the high compatibility. The data presented will act as a reference to aid in the predicition of SAW behaviour. Finally the effect of piezoelectric coupling on the bulk wave solutions is inspected for quartz and lithium niobate. The piezoelectric coupling was predicted to not have a large effect on the SAW solutions for these crystal, based on the bulk wave velocities this remains true for quartz. For lithium niobate, the larger coupling coefficient shifts the bulk waves velocity surfaces and increases the anisotropic structure of the crystal. The impact this will have on mulitllayered SAW existence will be explored in Chapter 7, along with possible consequences of ignoring the coupling.

Chapter 3

Development of Numerical Methods

The numerical toolkit that will be used in the subsequent chapters will be developed throughout this chapter. Methods that can solve both the partial wave eigenvalue problem in materials with anisotropic stiffness and layered boundary condition determinant are required. For both stages of the procedure, the problems covered in this work are all deterministic and formulated as linear systems. The main tool is the procedure of tracking curves of constant complex phase, this method is well suited to the problem of layered attenuated surface acoutic wave (SAW) modes. The methods to be able to solve fixed frequency problems are also developed at the end of this chapter, along with any prerequisite conditions for the use.

3.1 Introduction

3.1.1 Requirements of Numerical Methods

In Chapter 2 the behaviour of partial wave solutions of the characteristic polynomial of the wave equation was discussed. For simple cases, for example isotropic materials, the complex roots to the equation of motion lie on either the imaginary or real axis [1]. A particular behaviour of interest occurs around the bulk waves velocity in which the complex conjugate pairs become real by combining and then spliting on the real axis. This leads to loss of information in the numerical tracking with changes in velocity, requiring new initial search input. In cases of anisotropy stiffness, these roots are allowed to be complex and may even return to being complex conjugates after real transition by reforming with another real partial solution. This removes the possibility of attempting to re-track the solutions by sweeping the real axis, instead requiring some form of grid method or redefining the tracker location. This behaviour means that the method to track

these roots must either be able to efficiently track the unknown solutions or be able to re-track the solution after points of joining.

The majority of the work presented in the remaining chapters is focused on SAWs in layered geometries, many requiring searching in the complex domain. Unlike the half-space geometry which has non-dispersive solutions at particular velocity values, branches of solutions may exist for multiple values of velocity. Allowing energy attenuating solutions to the boundary condition determinant now requires searching in the complex plane of the wavenumber or the frequency, see Chapters 4 and 5. The numerical methods need to be 2-dimensional, tracking on the real and imaginary parts similar to the partial wave solution. Unlike the partial wave case which has six solutions, the boundary conditions for dispersive waveforms can have an infinite number of modes. The numerical method would need to be capable of tracking a variable number of solutions as specified by some input range.

3.1.2 Brief review of numerical methods

Traditional gradient descent methods [2, 3] in 2-dimensions make use of the divergence to track a minimum, but require some knowledge of the starting point. An example of a gradient independent method is the search by golden sections, which eliminates regions until convergence on a point is achieved [4, 5]. This method requires some knowledge of the location of a solution and requires only one minimum within a region. Due to the requirements listed in Section 3.1.1 these methods may only be used for secondary tracking within the neighbourhood of a solution.

If the functions in each part of the problem can be shown to be holomorphic, this allows for the use of winding number based methods to determine the complex roots. Focusing on these, a number of methods are present in the literature which use the argument principle in discretisation of a region of complex space [6–9]. Such approaches use the argument principle as a condition for the search of roots by eliminating none solution regions and focusing on correct regions of solutions.

3.2 Complex Analysis and Argument Principle

3.2.1 Argument principle

The main numerical method that will be developed in this chapter uses the argument principle for holomorphic functions, the statement of this principle can be found here [10]. The following

statement is a modified version of this definition of the argument principle, where the p-points, $z = p$, are the preimages of $f(z) = 0$.

> *If f(z) is holomorphic inside and on a simple closed loop G, and N is the number of p-points (counted with their multiplicity) which reside within the loop G, then there exists exactly N curves of constant complex phase which originate at p-points and end at distinct points on the loop G for every complex phase angle.*

This is illustrated in Figure 3.1, (a) the curves of constant phase angle for 0 and $\frac{\pi}{2}$, in the preimage, connect the p-points and loop G. These curves are, in this case, just the portion of the real and imaginary axis between zero and loop G in $f(z)$ in (b). A p-point which is a multiple root will have multiple curves each with distinct end points on loop G.

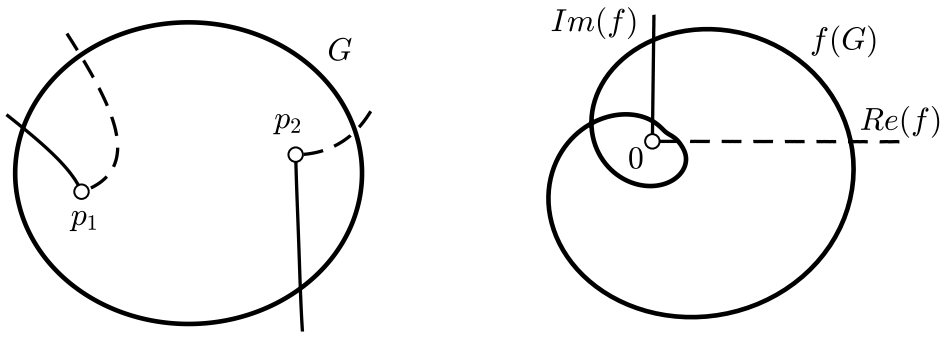

(a) Domain (b) Image

Fig. 3.1 (a) shows the closed loop G around two p-points on the domain of $f(z)$, for both points the curves of constant phase are shown for angle 0 (dashed) and $\frac{\pi}{2}$ (solid). (b) shows the image of G, now G loops around zero and the lines of constant phase are the real and imaginary axis which intersect $f(G)$ twice.

For cases in which solutions of the $f(z)$ are outside of the simple loop G additional curves of constant phase may also exist,

> *For all points on the simple loop G of a fixed phase angle, denoted R, there exists M lines connecting each R point to another unique R point on the loop G or a p-point within the simple loop G, for which the number of curves is given by* $M = N + \frac{R-N}{2}$.

These curves of constant phase may never intersect as this would invalidate the argument principle at the point of intersection. A loop G that smoothly deforms over this intersection to a loop H would have a varying winding number for constant p-points. The definition of the argument principle presented is equivalent by requiring distinctive end points to the curves of constant

phase for each of the p-points. These distinct curves are useful for the fast numerical tracking of all possible solutions within some predefined region of a holomorphic function.

3.2.2 Partial wave determinant

In Chapter 2 the eigenvalue problem (2.17) of the 3-dimensional wave equation was solved using the Stroh form. Additionally, the operator of the eigenvalue problem has been shown to be Hermitian using major and minor symmetries of the stiffness tensor. Now if f is the characteristic equation of (2.17) then $f(p)$ is a sextic polynomial in which each characteristic root p has an associated eigenvector A_l for the eigenvalue ρv^2. Therefore, f is holomorphic and must have six complex solutions, which may be degenerate but will have distinct curves of constant phase. These curves of constant phase can been seen in the determinant of (2.17), presented in Figure 3.2. The complex function presented is a 2-dimensional surface but require four axes to fully visualise the $\mathbb{C}^2$ structure. Although, from the point of view of vector spaces, this statement ignores the additional structure that makes $\mathbb{C}$ isomorphic to $\mathbb{R}^2$. But this statement still highlights the approach to plotting complex surfaces using computation methods.

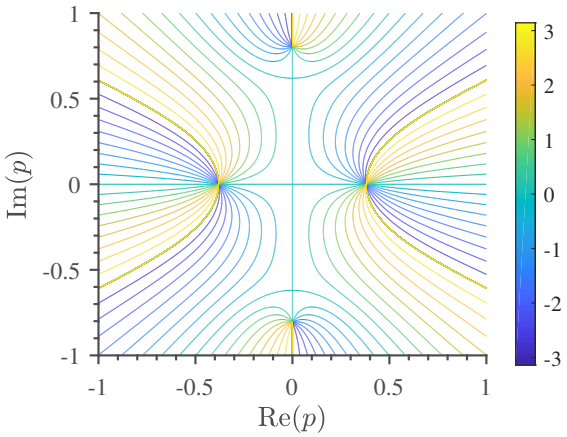

Fig. 3.2 Eigenvalue determinant of problem (2.17) fixed at a velocity between the shear and longitudinal bulk velocities. Colour map denotes complex phase, solutions are points that appear to have all phase values.

The partial wave solutions for an isotropic stiffness tensor presented in Figure 3.2 are either pure imaginary complex conjugates or pure real. The zeroes of this determinant are the solutions, these are located in the domain of $f(p)$ at the origins of curves of constant phase. The image of these curves of constant phase in $f(p)$ are straight lines which originate at a zero in the complex plane and tend towards infinite at their respective phase angles. Zero points at which two distinct

sets of constant phase curves originate corresponds to degenerate solutions of the eigenvalue problem.

The isotropic case presented in Figure 3.2 has an analytic solution [11], along with special cases such as cubic in highly symmetric directions. A symbolic approach with Cardano formula may be used if the problem can be written as a bi-cubic then an analytic solution may be determined. The introduction of odd power terms into the sextic equation breaks the symmetry in the complex plane in the imaginary axis, this is normally due to the loss of symmetry in the stiffness tensor. In most anisotropic cases, numerical methods are required to compute these partial wave solutions.

3.2.3 Boundary condition determinant

The boundaries used throughout this work are uniform surfaces which are normal to $\boldsymbol{n}$, this allows inhomogenous behaviour in only the $n_j x_j$ direction. Several types of boundary conditions listed in Table 3.1 [11].

Type	**Boundary conditions**
Free surface	$u_i = 0$
Free surface	$t_i = 0$
Interface	$u_i = u_i'$
	$t_i = t_i'$

Table 3.1 Lists several boundary conditions taken into consideration for the development of the numerical scheme.

The components of the traction $\boldsymbol{t}$ are t_i, these are normal to the boundary surfaces defined as,

$$t_i = \sum_{j,k,l=1}^{3} C_{ijkl} \frac{\partial u_l}{\partial x_k} n_j. \tag{3.1}$$

The displacements in these boundary conditions are the linear combinations of the solutions to the eigenvalue problem (2.17) in the summation,

$$u_i = \sum_{r=1}^{6} B_r A_i^{(r)} \mathrm{e}^{\mathrm{i}(k(\boldsymbol{m}\cdot\boldsymbol{x} + p^{(r)}\boldsymbol{n}\cdot\boldsymbol{x}) + \omega t)}. \tag{3.2}$$

The boundary conditions listed in Table 3.1 are sufficient for describing the plate and half-space geometries for single or multi-layer combinations of materials. The constants B_r of (3.2)

are found by solving the boundary condition determinant, constructed for a particular geometry. A square determinant is a summation of d! terms in which each term is a permutation of products for d elements. Once rearranged, each term of the determinant will be some combination of sums and products of the displacements (3.2) and tractions,

$$t_i = \sum_{r=1}^{6} B_r L_i^{(r)} k \mathrm{e}^{\mathrm{i}(k(\boldsymbol{m}\cdot\boldsymbol{x}+p^{(r)}\boldsymbol{n}\cdot\boldsymbol{x})+\omega t)}, \tag{3.3}$$

Therefore, for all boundary conditions listed, the determinant is composed from sums and products of analytic functions and therefore is holomorphic.

3.2.4 Modular object orientated MATLAB code

Throughout all of the remaining chapters, additional physical behaviours are introduced along with the updated boundary conditions. The methods developed in this chapter may be applied to all of these up coming cases. Therefore, the numerical code that is developed in this chapter will take advantage of object-oriented coding to modularise the boundary conditions [12]. This combination of different behaviours is done through each of the material types and will allow cross combinations to generate determinants.

The object-oriented code is used only for the organisation and inherited functionalities, different types of materials are created using classes. The class contains all the matlab functions and methods required for the generation of mathematical functions pertaining to that material type, primary the eigenvalue and boundary conditions. The base class of this numerical code is the elastic class, which contains the definable properties values for stiffness and density. The eigenvalue and boundary condition functions may be generated as an instance of this class for a defined material. The material types to follow in the remaining chapters will be subclasses from this base class, or from each other but the elastic class is the superclass to all.

For each of the boundary types outlined in Table 3.1, a matrix or matlab function will be generated. These may be combined into a predefined function for the determinant, using all of the materials in the combination. Taking this approach will allow many different layered combination to be explored including variation of plate and half-space geometries, for various types of materials. New types of boundary conditions or physics, that can be modelled using the eigenvalue approach, can be inserted with ease. This will prove useful for modelling the various material combinations of interest, see Section 1.2.2 for common materials.

3.3 Tracking Along Curves of Constant Phase

3.3.1 Procedure

The following steps outline the procedure for tracking over curves of constant phase on a 2-dimensional surface $f(z)$, see Appendix C for example MATLAB code. The main procedure uses a two part algorithm consisting of a tracker section and a correction section, when the curvature increases the correction activates to adjust the direction of the next step. Without a correction step the tracker may drift onto a curve for another solution, the correction method used is based on ridge tracing methods [13]. When the sign of the curvature changes, the direction of the correction search also changes to reduce the amount of steps required to make a correction, the procedure is illustrated in Figure 3.3.

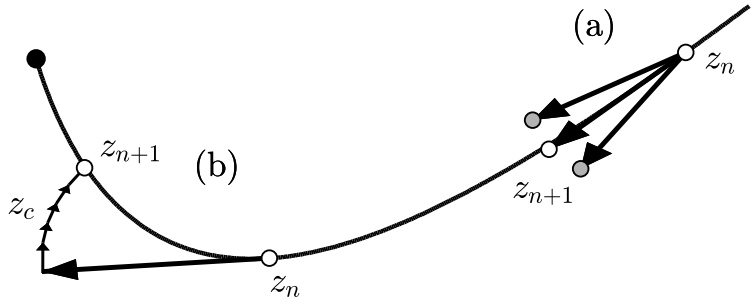

Fig. 3.3 Shows the line tracing part of the procedure. At (a) the linear step is taken in the predicted direction to find the next point on the curve. At (b) the correction step, due to increased curvature, requries additional search steps which may be reduced by predicting the correct direction.

Initial procedure to find all starting point z_0:

I. Define a search region enclosed by a loop or box G.

II. Search over G for all the starting points denoted z_0 of a selected phase $arg(f(z_0))$. The approach taken is a search on the elements of G to minimise the difference in $arg(f)$ between points along G and the selected phased.

Main procedure for each starting point z_0:

1. The first step can take one of two possible directons along the curve of constant phase. A minimum of four steps in two orthogonal directions is required to get a rough approximation of the correct direction for the first step, see Figure 3.4. Assuming that the test steps are within a linear range, from the two orthogonal directions one should minimise the change in phase $arg(f)$ which corresponds to the direction closest to the curve. Two

possible directions now remain on a line, the step that minimises the magnitude $|f|$ is the correct direction. More steps can be used for greater accuracy without a large cost to the overall runtime of the procedure.

2. Tracker: Take a primary step dz in the predicted direction to a new point on the curve z_n. Take two secondary steps with the same radius dz but at a positive and negative angle from the primary step, see (a) in Figure 3.3. In this procedure the angle is tied to the correction step size.

    * If step is outside of the search region G discontinue search.

    * If $|f|$ of the primary step is not the minimum of the three steps taken, then proceed to the correction step 3 with updated sgn(C) based on which step is the minimum, otherwise $z_{n+1} = z_n$ return to 2.

3. Correction: Search over a circle around the centre point z_n in the direction given by $sgn(C)$, the step z_c is based on the radius dz and the number of discretizations.Take the point z_{n+1} which minimises the $arg(f)$ and lowers the $|f|$ from z_n. The correction section concludes as soon as z_c meets the criteria, see (b) in Figure 3.3.

    * If the circle sweep is unable to find a value for z_{n+1}, with a lower$|f|$ than z_n, then continue to final step, otherwise return to 2.

4. Reduce the $|dz|$.

    * If the error term is within the required convergence then output solution, otherwise return to step 2.

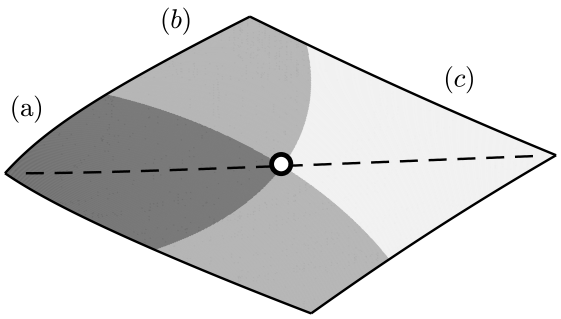

Fig. 3.4 The regions on the surface $f(z)$ illustrate different behaviours for a step taken from the white point on the constant phase curve (dotted) into these regions. For (a) and (c) the step will have greater change in $|f(z)|$ than $arg(f(z))$ and for the two (b) regions the step will have greater change in $arg(f(z))$ than $|f(z)|$. For the curve of constant phase, the region (a) with $|f(z)| \to 0$ is towards the solution, and so (c) with $|f(z)| \to \infty$ moves away from the solution.

3.3.2 Optimisation of input

To further analyse the numerical method that has been developed, the overall procedure must be broken down into seperate algorithm blocks. Three different step sizes are used in the outlined procedure, one in part II of the initial procedure and two in the main procedure in parts 2 and 3. The number of steps performed in Part II is a linear funtion of the step size or divisions of the loop G. The step size should be chosen to minimise the number of steps without sacrificing accuracy. Though the selected starting phase angle may be chosen to be any phase angle with the same result, therefore the step size only needs to be small enough to distinguish between sets of phase angles for different solutions. If the number of roots are known then the step size can be reliably large as long as the starting phase is redefined for the main procedure.

The steps taken in the main procedure starts as a linear function of two input step sizes, this is then followed by a quasi-logarithmic form when the tracker starts to approach the solution. For each step in the main procedure the number of steps taken is given by,

$$f = 3n_2 + N_c n_3, \tag{3.4}$$

where n_2 and n_3 are step sizes for part 2 and part 3. The order of magnitude of n_3 is consecutively reduced whenever the tracker reaches the solution, inducing the quasi-logarithmic convergence. The number of correction steps taken is N_c which varies for each step. The step size n_3 is the arc length dependent on the radius n_2, see (b) in Figure 3.3. The input variable is instead taken as d, the number of line elements in the discretisation of the completed circle around z_n. On the last

step of the procedure the correction step acts as a convergence check with the number of steps $N_c = d$. So now n_3 can be written in the form

$$n_3 = \frac{2\pi n_2}{d}. \tag{3.5}$$

Increasing the size of n_2 reduces the number of steps required to get within the local range of the solution for the convergence process to begin, see Figure 3.5. The maximum allowable size of the initial input n_2 is limited by the smallest length between what is numerically taken as non-degenerate solutions. Increasing this initial size of n_2 leads to a higher chance of the tracker jumping to the curve of constant phase of another solution, in the case shown in Figure 3.5 this occurs close to the maximum step size presented. Note this optimisation test was performed on the partial wave determinant of an anisotropic material and results may vary based on the case.

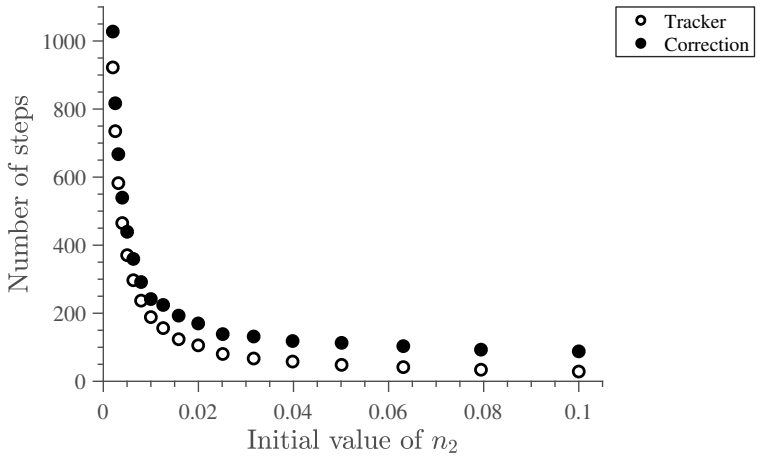

Fig. 3.5 The total number of steps taken in the tracker (part 2) and correction (part 3) with change in the initial starting step of n_2 with $d = 36$, the case shown is the average computation of all six solutions to the partial wave determinant.

The input d should be as small as possible to reduce the number of correction steps N_c, see Figure 3.6. If the step size n_3 is too large the correction or convergence will fail, this is the only factor limiting the minimum possible input of d. Therefore, for both stepsizes, the optimisation of the stepsize is a simple balance between reliability and number of steps required to complete.

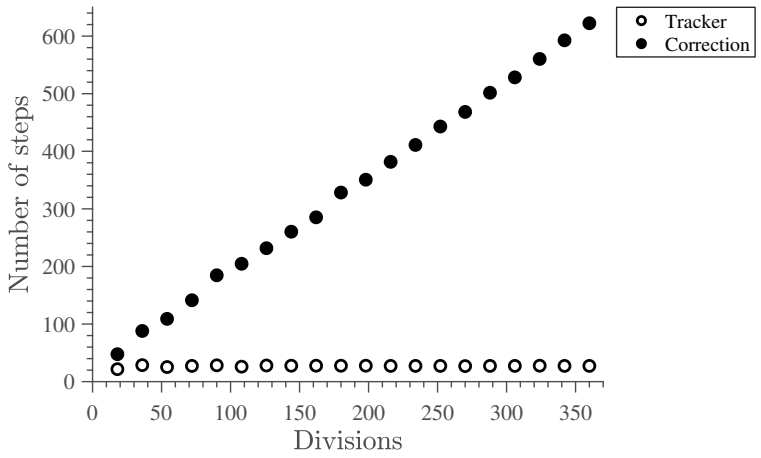

Fig. 3.6 The total number of steps taken in the tracker (part 2) and correction (part 3) with variation of number of divisions d with $n_2 = 0.1$, the case shown is the average computation of all solutions to the partial wave determinant.

3.3.3 Comment on real velocity

The eigenvalue problem (2.17) for the non-attenuated and non-leaky case only requires real values of k and ω. By fixing the velocity, the p roots remain constant from point to point in the boundary condition search due to the form of (2.17). This significantly reduces the computation required in the boundary condition problem which is a function of k for fixed velocity, and can easily be transformed back to the $k - \omega$ form. For the attenuated and leaky cases, constant velocity values may be imposed and solutions will exist. However, for complex k values, which are required for these cases, complex ω values are also required to get real velocities. Constant velocity solutions are still of interest but limiting in scope, the more applicable solutions require real ω values. This would require a changing velocity value of the form,

$$v = v_{real}\left(1 + \mathrm{i}\frac{\alpha}{\beta}\right), \tag{3.6}$$

where $k = \beta + \mathrm{i}\alpha$ which reduces to the non-attenuated case for $\alpha = 0$. Therefore, p roots would no longer remain constant but is now a function of the ratio between imaginary and real wavenumber values for fixed ω. A numerical search applied in the $\beta - \alpha$ space, for the boundary condition problem, would now require the computation of p roots for every point. Taking advantage of the form (3.6), the search could be performed in directions of constant ratio $\frac{\alpha}{\beta}$ in which the complex velocity v remains fixed. In Chapter 4 the existence of solutions in which $\mathrm{Im}(\omega) = 0$ will be investigated by introducing a complex velocity in this form.

3.4 Phase Tracking for Fixed Frequency

In wave based biosensor design a fixed wavelength is typically imposed in the transducer design, this is imposed by the geometry of the biosensor. Solving the wave problem in velocity space is useful for viewing the existence of different types of waveforms within particular ranges, this would also limit the possible frequency range. In mechanical biosensor design, it is the frequency shift mechanism which is of interest; waveforms are excited at particular frequencies and the changes are observed. For annular transducer design, the entire transducer array is excited at a single frequency, requiring a non-circular structure for variation due to anisotropy in material properties. Annular transducer design will be discussed further in Chapter 5.

The frequency may just be fixed at a set value in the constant phase tracking procedure, the partial wave roots would have to be computed for every change in velocity at each step or precomputed for a velocity range. The computation of these roots would not only be numerically costly but at times lead to instability, requiring a higher degree of convergence and checking to smoothly plot the boundary conditions. The instability occurs most typically in problems which couple physical gradients that are orders of magnitude apart, magnifying boundary determinant errors. Therefore, it is of interest to develop a fixed frequency numerical method which has the benefits of constant velocity tracking, this is the objective of this section.

3.4.1 Fix frequency and sampling dispersion curves

The first approach which may be taken is to compute the dispersion curves in for fixed velocity, and then take slices at particular frequencies that may exist. If the waveguide dispersion information has already been computed, then this becomes a rough way of approximating the possible fixed frequency surfaces. For frequency independent cases, the dispersion curve only need to be computed for one wavenumber, the frequency and wavenumber can be scaled relative to the velocity, assuming a fixed real velocity. For frequency dependent cases, the dispersion structure will also be dependent on frequency and would have to be computed on a based by based case. In the case of computing anisotropic slowness information, the dispersion curves will be a set of slowness-dispersion cylinders for each of the modes. The fixed frequency data would then be slices of these slowness cylinders at particular frequency values. Examples of anisotropic velocity surfaces are given in Section 4.2 in the wavenumber domain. These slowness cylinders are numerically costly to compute, this without factoring in the possibility of frequency dependence. The computation of this data would also have to be at a high enough resolution to minimise error in slicing the velocity data for which the fixed frequency may lie between

computed steps. This approach is not feasible for computing frequency information for particular cases, the use of this method should be restricted to first approximations for pre-existing data.

3.4.2 Golden section optimisation with phase tracking

An alternative approach is to use an additional numerical search after the constant phase tracking to minimise the difference between the required and output freqency. The optimisation method chosen is search by golden sections [4, 5], taking advantage of the golden ratio (3.7) allows the sampling and elimination of sections of a predefined 1-dimensional region,

$$\Phi = \frac{1-\sqrt{5}}{2}. \tag{3.7}$$

This would require prior knowledge of the location of a solution, the easiest approach would be computing the dispersion information within the desirable velocity range. So this method would either be used to converge on an already known solution or find the starting point of a solution branch at constant frequency. Even though prior information of the solution is also required in the constant phase tracking approach, in the forms of starting regions, this method requires knowledge of a local branch of solutions. The major benefit of this method is the faster computation time along with natural reduction of error caused by frequency dependence, discussed further in the next section.

Provided that the dispersion structure is known, the desired fixed frequency within a section of the dispersion is selected. A velocity range around this frequency is selected as the golden section search range, this is illustrated in Figure 3.7.

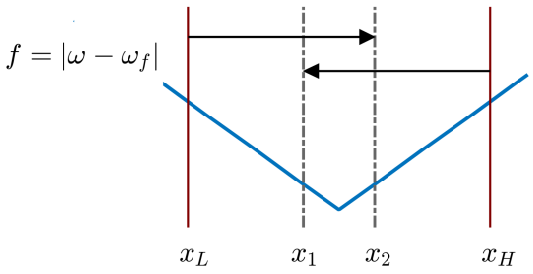

Fig. 3.7 An illustration of the search by golden section method on a portion of the dispersion curve, the function is now the difference in magnitude of the frequency curve and the selected fixed frequency.

For each step of the golden section search, the constant phase tracking procedure is used on a local area to find the point on the dispersion curve. A direct magnitude tracking approach may be used for the search dispersion, provided the search range is small and outside the range of

other dispersion curves. The partial wave solutions must be tracked using curves of constant phase to allow the search by golden sections to be performed across transiton points. The search by golden section method is briefly outlined in the following steps:

1. Define the set frequency and velocity search range, labelled x_L to x_H, around this value.

2. Find x_1 and x_2 using the golden ratio,

$$x_1 = x_H - \Phi(x_H - x_L), \tag{3.8}$$

$$x_2 = x_L + \Phi(x_H - x_L). \tag{3.9}$$

3. Check the function $f(v)$ at x_1 and x_2, and then redefine x_L or x_H based on the following conditions.

   * If $f(x_1) > f(x_2)$ set $x_L = x_1$
   * If $f(x_1) < f(x_2)$ set $x_H = x_2$

   It is guaranteed that the minimum, dependent of course on the shape of the function, is within the remaining search range.

4. If sufficient convergence is achieved between the function values at x_L and x_H, then output the solution, else repeat steps 2 through to 4.

3.4.3 Fixed partial solutions in frequency dependent cases

In the remaining chapters, partial wave eigenvalue problems which have a frequency dependency exist. Therefore, in the constant phase tracking step, the partial waves will be dependent on the changing frequency even if the velocity is fixed. This would make the search by golden section redundant, increasing the computation steps beyond the amount needed for a constant phase tracking in the frequency domain. It is possible to attempt a search by repeated fixing and updating frequencies, briefly outlined in the following steps. This may be combined with a perturbation method to find the change in the solution with changes in a parameter such as layer thickness or angle.

1. Set the fixed frequency ω_{fix} close to a known solution.

2. Using gradient tracking or constant phase tracking, find the local change in frequency ω_{out}. For a perturbation approach the change in solution from a known solution may be track with change in a parameter such as angle or thickness.

3. Update ω_{fix} with ω_{out}.

    * If a convergence between fixed and output values is reached then end procedure.

    * Else repeat steps 2 to 3.

Unfortunately, the frequency dependency may cause large drifts from the true value with small shifts in the fixed frequency. With increased steps the error between ω_{fix} and ω_{out} divergences, this can occur close to known solutions. For searches using golden sections, this divergence can be seen in the function to minimise, $f = |\omega_{out} - \omega_{set}|$. Presented in Figure 3.8 is the comparison between the correctly tracked and fixed minimisation functions, where for the fixed case $\omega_{fixed} = \omega_{out}$ at ω_{set}.

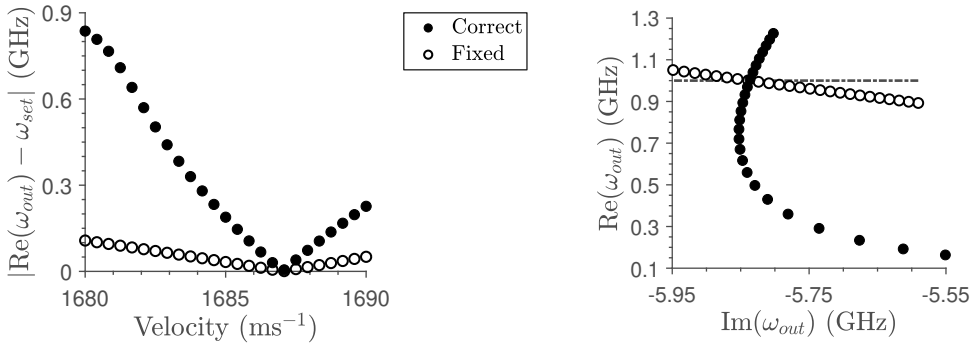

(a) Minimisation

(b) Complex plane

Fig. 3.8 Comparison between the correctly tracked and fixed frequency functions, ω_{fix} is set to ω_{out} at the ω_{set} of the correct function. Presented in (a) is the minimsation function used in the golden section search and in (b) the ω_{out} functions projected on the complex plane.

Away from the point where $\omega_{fix} = \omega_{out}$, the solutions to the fixed case diverge from the correctly tracked solutions. Attempting to track the minimum for any changes in parameter leads to diverging errors, dependent on the strength of the frequency dependency. In this case the function is the branch of solutions for SU-8 epoxy-based photoresist (shear viscosity of $\eta = 0.059$) on lithium niobate, this particular material is discussed in more detail in Section 5.2.

Tracking fixed slowness surfaces will be of interest in Chapter 5, the error between the fixed and tracked slowness surfaces will be checked to see if the fixed approach is suitable. Otherwise, the remaining options are constant phase tracking or locally tracking the shift in solution, this would be done using a 2-dimensional gradient method on the complex plane. This approach

is numerically quicker than constant phase tracking, but can not account for variation due to transition points. Additionally, the branches of solutions must not be in the local vicinity of other branches, due to the 3-dimensional nature of the problem, this tends not to occur.

3.5 Conclusions

In this chapter the argument principle for holomorphic functions, has been redefined to emphasise the structure of the curves of constant complex phase. For this definition to be equivalent to the well-known argument principle, it is required that the curves of constant phase of different solutions can not intersect. The functions of the partial wave and boundary condition problems are holomorphic, this allows for the use of numerical methods that take advantage of the argument principle. A numerical method based on the curves of constance phase has been developed, in constrast to the literature which is comprised of grid based approaches. This constant phase tracking procedure traces the phase curves from a loop G to the solutions. For this procedure it has been shown that the two step sizes should be set as large as possible, with the limiting factor being reliability of the curve tracing. The other factors affecting computation time includes, size of search loop in relation to solutions and the number of curves of constant phase to track.

For the mechanical problem, the partial waves remain constant for fixed phase velocity, this significantly reduces computation time for the boundary condition problem. Fixed velocity searches are normally used in the existence problem, where the change in velocity can lead to changes in wave structure. For biosensor application, it is required that the frequency remains constant, a hybrid search by golden section with velocity constant phase tracking has been developed. This approach minimises the frequency within a velocity range, unlike constant phase tracking for a set frequency, this would require prior knowledge of the location of the solution. Another disadvantage is the limiting of one branch of solutions per computation, these negatives are outweighed by the increased computation time. For cases with frequency dependent partial waves, it has been shown that a fixed frequency approach leads to divergences in the solution. The procedure requires additional partial wave tracking to account for these frequency dependent variations, unless the dependency is small.

Chapter 4

Attenuation in Mechanical Waveforms

In Chapter 2 several non-attenuated waveforms were defined, as discussed in Chapter 1, these waveforms have traditionally been used in biosensor designs. In addition to these waveforms, energy leakage SAWs may exist in the half-space geometry which carry energy away from the surface of the structure. The study of these attenuated waveforms will lead to insight on their behaviour, which may be used to optimise current biosensor designs and develop novel sensors. Presented throughout this chapter is the definition and numerical study of leaky behaviour in SAWs. The leaky transition is explored in anisotropic combinations, in which conflicting symmetries create new transition regions, and directional dependent leaking of energy. These transition regions are sections of the bulk wave velocity curves between intersection points with other bulk velocity curves. The resulting bounded area between the two velocity curves may have unique behaviour, due to the partial wave roots, this is investigated in this chapter. At the end of this chapter, velocity surfaces for fixed real frequency values are presented, in this format the data can be used readily for biosensor design.

4.1 Formulation of Attenuated Waveforms

The leaky surface acoustic wave (LSAW) is a supersonic phenomenon that exists in isotropic media under certain conditions, [1, 2] and in anisotropic media [3]. These waveforms are labelled supersonic, due to the coupling of a bulk propagating partial wave, which comes into existence above the bulk velocities of the material. The slowness structure of these LSAWs, is of interest for circular biosensor application, for the mitigation of energy loss. Numerical studies in the slowness structure of LiNbO3 and LiTaO3 have been preformed for LSAWs [4–6], recently the experimental and numerical study of several silicon cuts were conducted [7]. LSAW

branched solutions may exist in the layered case, in which the substrate has a contribution from a bulk propagating partial wave. The literature on multilayered LSAWs is limited compared to the half-space cases, most literature that can be found only considers particular directions of anisotropic materials [8, 9]. Leaky behaviour in most cases is detrimental to the preformance of a biosensor, but some cases of biosensor detection mechanisms based on LSAWs exist [10–13].

4.1.1 Expansion to attenuated cases

The assumed form for the solution in Chapter 2, only permitted propagating waves in the $\boldsymbol{m}$ direction. An approach to capturing leaky behaviour in the literature, [14] is to introduce a complex wavenumber $k = \beta + \mathrm{i}\alpha$. The imaginary part, corresponds to the energy loss through decay behaviour in the propagation direction, denoted the attenuation α. The solution now takes the form,

$$u_i = A_i \mathrm{e}^{-(\mathrm{i}\beta-\alpha)(\boldsymbol{m}\cdot\boldsymbol{x}+p\boldsymbol{n}\cdot\boldsymbol{x})+\mathrm{i}\omega t}. \tag{4.1}$$

This solution can be rewritten into the velocity form using $v = \frac{\omega}{\beta+\mathrm{i}\alpha}$. For now only attenuated cases in which $v \in \mathbb{R}$ will be considered, these require $k, \omega \in \mathbb{C}$. These cases have improved computation runtime when v remains fixed, and serve to provide initial insight into attenuated wave behaviour.

The partial wave eigenvalue problem of (4.1) is written in terms of k and ω in the form;

$$\left[(\beta + \mathrm{i}\alpha)\Gamma^{il} - \rho\omega^2\delta_i^l\right] A_l = 0. \tag{4.2}$$

The case of setting only $\alpha = 0$ has already been covered, the operator is Hermitian and so a set of p solutions may be found for a real frequency input. Setting only $\beta = 0$ results in the skew-Hermitian version of Γ^{il} leading to an imaginary value for the frequency. Isotropic solutions which were originally on the real axis, in the Hermitian case, are now rotated back onto the imaginary axis, see Figure 4.1.

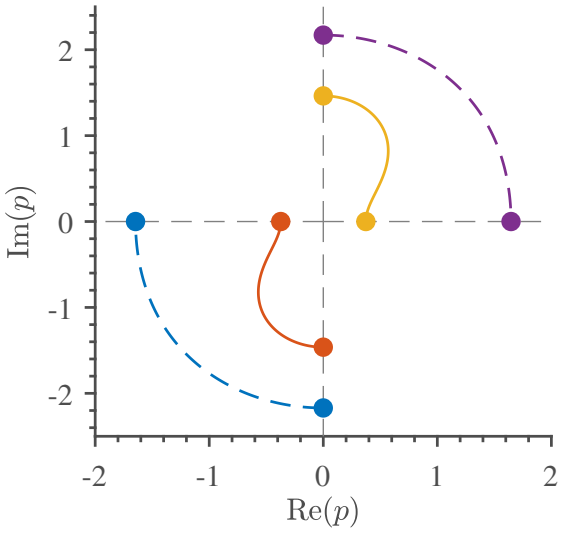

Fig. 4.1 The effect of rotating the wavenumber along the complex unit circle has on the partial wave solutions of an isotropic material. The starting point is on the real axis with a phase velocity that is greater than the highest bulk velocity, the dotted lines correspond to the degenerate shear partial solutions.

The operator $k\Gamma^{il}$ can be shown to be normal, simply from the product of the commutative Hermitian and skew-Hermitian parts. This commutative property is well expressed in the summation notation of the tensor formulation, order of the terms does not matter in this case. Following this for attenuated cases, the eigenvalues ω does not have to be purely real but the eigenvectors do form an orthogonal basis.

Consider once again the complex case, but with an additional condition to enforce $\omega \in \mathbb{R}$ requiring a complex velocity. The constrained dispersion relationship takes the form;

$$\frac{\omega}{\beta + \mathrm{i}\alpha} = v_r - \mathrm{i}\frac{\alpha}{\beta}v_r, \tag{4.3}$$

where v_r is the real part of the velocity $\mathrm{Re}(v)$. This condition reduces the allowable range of velocity values, by enforcing the imaginary part of the velocity to be a scaling of the real part, by the ratio of imaginary to real parts of the wavenumber k. This can be viewed as restricting the search to the subset of possible solutions, which result in complex wavenumber with real frequency. Setting both of the values v_r and ω, enforces the following condition between the real and imaginary parts of the wavenumber,

$$\beta = \frac{\alpha^2 v_r}{\omega} + 2\mathrm{i}\alpha + \frac{\omega}{v_r}. \tag{4.4}$$

4.2 Transition to Leaky Waves

Combinations of anisotropic materials, with differing material symmetries for particular cuts, can commonly occur in biosensor applications. For most biosensing technologies, these anisotropic effects do not have a significant impact. For devices that take advantage of circular geometry, these effects can no longer be ignored due to excitation of the whole cut. The overlapping of bulk solutions can give rise to new regions of wave transition in the combined bulk wave solutions, in these new regions LSAWs can exist. In this section the affect of leaky behaviour is studied in particular crystal symmetries and the resulting dispersive behaviour of the composite SAW modes is discussed.

4.2.1 Leaky transition in anisotropic materials

Cubic silicon has 4-fold cyclic symmetry, while trigonal quartz has 3-fold cyclic symmetry, but a quasi-6-fold symmetry in the Z-cut which is dependent on wave type. The behaviour of LSAWs is explored in these cuts of quartz on silicon, in a layered half-space configuration. The bulk wave velocities of quartz, are typically lower than the bulk velocities of silicon, making them compatible for quasi-Love propagation. As discussed in Chapter 2, this less compatible combination of silicon and quartz symmetries, will lead to extra transition regions due to overlapping bulk solutions. The relative bulk wave surfaces are the same as those shown in Figure 2.23. Interest is placed on the overlapping of the first silicon and second quartz velocities, which occurs at four points, the first is at approximately $\frac{2\pi}{6}$. At these points the wave is expected to become leaky, due to the contribution of a bulk propagating shear horizontal partial wave in the silicon.

After the maximum point on the lowest shear velocity of quartz, there is a region from approximately 3900ms^{-1} to 4300ms^{-1} of no overlapping in bulk solutions. After this region, up to around 4600ms^{-1}, the solutions remain non-leaky, but several crossings of the second quartz bulk wave occurs. This whole range is ideal for non-leaky SAW propagation, presented in Figure 4.2 are the first two complete SAW modes at velocities within the non-leaky range, which are above 4300ms^{-1}. The first mode is a shear dominate SAW and the second is the Rayleigh displacement dominate SAW. However, due to the cyclic dispersion by anisotropic stiffness, the relative contributions of each are not constant with propagation angle. Both modes illustrate 2-dimensional dispersive behaviour, in particular they show the coupling between these two dispersions, namely the waveguide and anisotropy. This behaviour is clearly seen in the first mode at 4300ms^{-1}, it has the 6-fold cyclic symmetry of the Z-cut quartz layer. On increasing the

velocities to 4600ms^{-1} the wave length into the depth increases, leading to a shape resembling the 4-fold symmetry of the silicon substrate. This is a reflection of the energy partitioning between the layer and the substrate, with increased velocity, the energy in the cubic substrate increases modifying the cyclic dispersion.

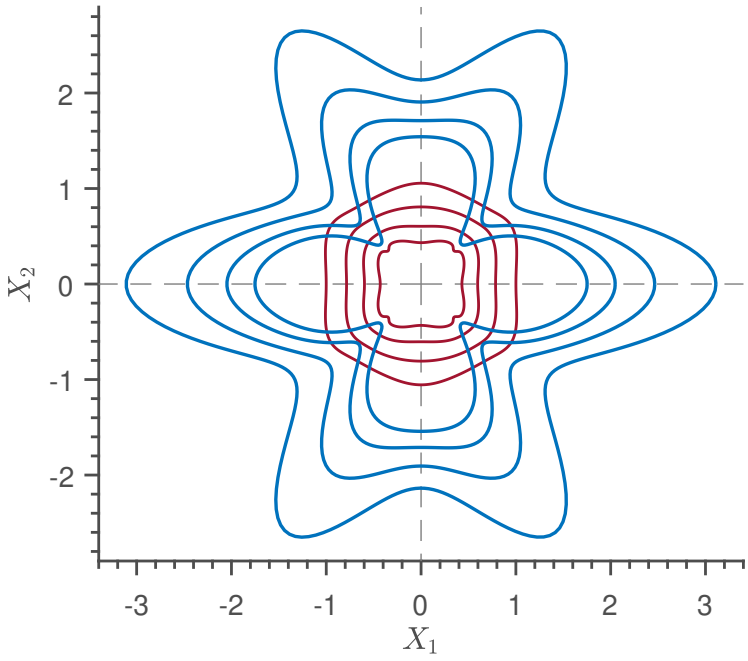

Fig. 4.2 Wavenumber surface for the first two complete plane propagating SAW modes in Z-cut quartz on (100) silicon, rotated in the $X_1 - X_2$ plane. For velocities 4300ms^{-1} (outer) to 4600ms^{-1} (inner) in increments of 100ms^{-1}.

At around 4700ms^{-1} the lowest shear of silicon will start having an effect on the SAWs, introducing leaky behaviour at particular angles. Presented in Figure 4.3 are the first two complete SAW modes between 4500ms^{-1} across the leaky transition to 4900ms^{-1}, note these are different modes than those shown in Figure 4.2. The leaky behaviour has an affect on the the 2-dimensional dispersion structure, in addition to the effects in the non-leaky case. The rapid shift in the symmetry structure of the modes is once again due to the increased energy contribution in the substrate, but this is due to the bulk penetrating LSAWs. The contribution of a bulk propagating partial, will change the generalised displacement form of the modes. Along with the relative dominance shear and Rayleigh type displacements between layer and substrate. The peak of the attenuation of the first mode at 4900ms^{-1} is approximately 0.81 rad, this is close to, but not directly corresponding to, the minimum of the lowest silicon bulk. This would suggest that the leaky behaviour is not completely dependent on the substrate bulk velocity as expected, but is slightly offset due to the quartz symmetry.

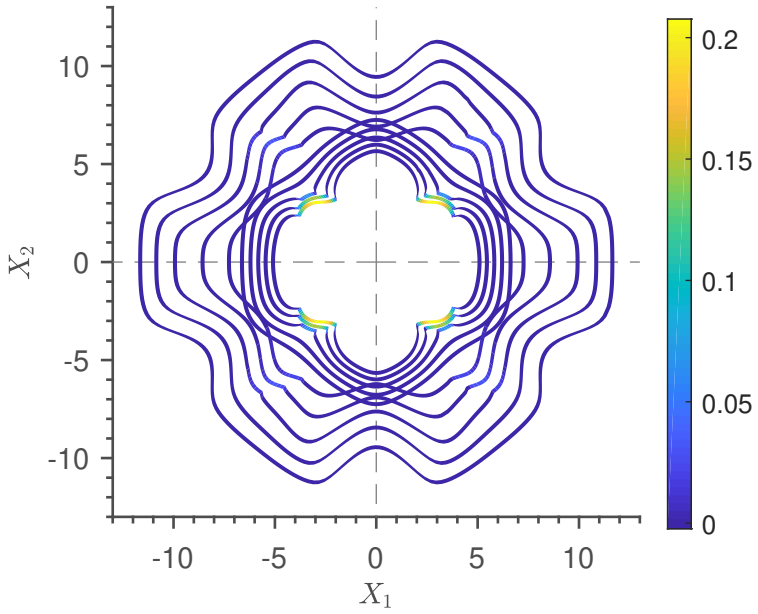

Fig. 4.3 Wavenumber solutions for the first two complete plane propagating SAW modes over leaky transition in Z-cut quartz on (100) silicon, rotated in the $X_1 - X_2$ plane. For velocities 4500ms^{-1} (outer) to 4900ms^{-1} (inner) in increments of 100ms^{-1}. Colour map denotes complex phase of the wavenumber.

Presented in Figure 4.4 is the change in real wavelength in X_1 denoted Re(λ_1) over the leaky transition, which is seen on Figure 4.3. The shift to LSAW behaviour is seen as a smooth kink in the wavelength surface for both presented modes. The rate of change in the real part of the wavelength in the X_1 direction reduces after this transition. The waveform is no longer propagating in the X_1 direction, but instead at some angle into the bulk, the wavelength surface supports this idea.

The behaviour presented is just the case of a single layer on a substrate, the bulk propagating partial is only coupling a larger portion of the substrate. The possiblility of taking advantage of this transition mechanism for dynamical activation of embedded inactive layers also exists. The study between the effect of SAWs verse LSAWs on embedded layers with bulk velocities lower than the transition velocity, would have to be conducted. Such mechanisms are beyond the scope of this research, but may prove interesting for enhancing biosensor detection mechanisms.

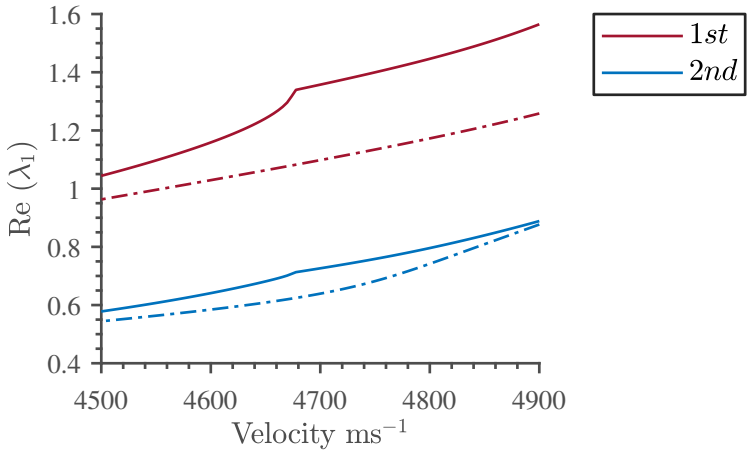

Fig. 4.4 Change in real wavelength in X_1 over the leaky transition for both modes presented in Figure 4.3. Presented for angles 0 rad (dotted) and 0.81 rad (solid), 1st corresponds to the mode with the lowest wavenumber.

So far, in this chapter, the data computed has been for fixed real velocity, a desirable requirement is that the frequency remains real requiring a complex value for the velocity. Such a solution would have no decay in the time part of the waveforms, this would correspond to pure spatial leaking. The possible existence of such solutions is worth checking, though the goal should be to minimise the imaginary part of the frequency. The imaginary frequency is discontinuous over zero imaginary velocity and tends toward large values towards positive and negative imaginary velocity. Figure 4.5 presents the frequency solutions in quartz on silicon over the leaky transition at a propagation angle 0.81 rad. These branches are from the same case as Figure 4.3 of transition from a non-leaky to leaky solutions.

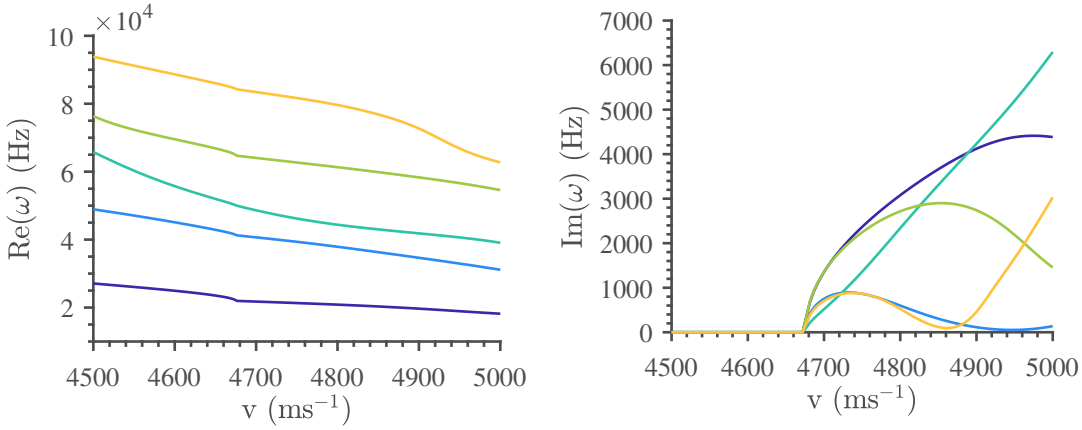

(a) Re(ω)

(b) Im(ω)

Fig. 4.5 Frequency solutions for the first five low attenuated branches in quartz on silicon at a propagation angle of 0.81 rad for velocity values over the leaky transition point.

For completeness, there also exists high attenuation solution branches before the transition point. Presented in Figure 4.6 are the positive high attenuation branches for the case of quartz on silicon, across the transition velocity at an angle of 0.81 rad. Based on the existence theory, these branches may correspond to a type of bulk propagating generalised Rayleigh LSAW in the layer. The Rayleigh type waves, come into existence below the lowest bulk velocity of a material, and may become leaky for transition velocities of the layer. The peak attenuation of these branches occurs within the first transition at approximately 4700ms^{-1} and the second transition at approximate 4900ms^{-1}, corrsponding to the second bulk velocity of quartz. The attenuation reduces as the velocity approaches the second transition, after the transition point the attenuation reduces to a similar range as the shear branches of Figure 4.5.

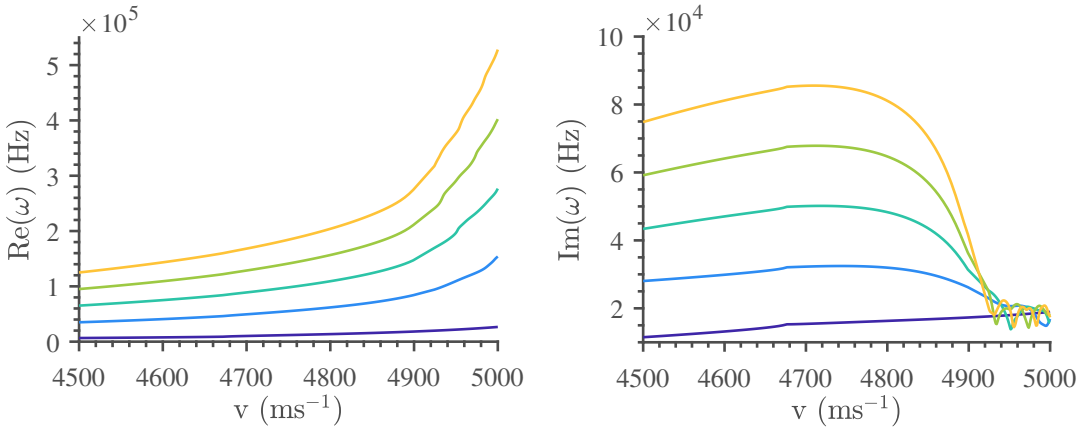

(a) Re(ω) (b) Im(ω)

Fig. 4.6 Frequency solutions for the first five high attenuated branches in quartz on silicon at a propagation angle of 0.81 rad for velocity values over the leaky transition point.

The presence of small minimums in the third region suggest the possibility of an optimum Im(v) to minimise the Im(ω). In this third region the substrate material will also have a bulk propagating partial contribution, which may lead to interactions between the layer and substrate leaky behaviours.

An interesting question arises, in the case of a generalised supersonic Rayleigh wave in the layer on a substrate with only decaying partial contributions. Can a leaky Rayleigh wave exist in this layer, and what happens to the waveform as the wavelength decreases from the plate range to the SAW range? Unfortunately these high attenuated solutions are not of interest for biosensor application and the focus is placed solely on low attenuated cases.

4.2.2 Plane wave solutions

The transition to leaky behaviour significantly changes the structure of the modal symmetry, the changing displacement forms of the mode gives insight into this rapid shift. The displacements will be inspected in the direction of maximum attenuation for the first mode shown in Figure 4.3 at an angle of 0.81 rad. Presented in Figure 4.7 and Figure 4.8 are the 1-dimensional displacements of the first and second modes, respectively. Each shown at the 4500ms^{-1} and 4900ms^{-1}.

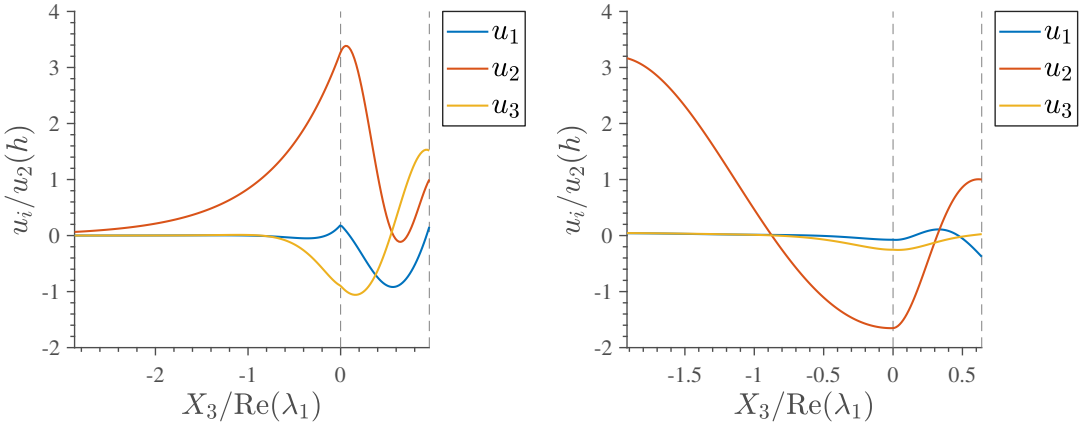

(a) 1st mode at 4500ms^{-1} (b) 1st mode at 4900ms^{-}1

Fig. 4.7 Displacements of 1st silicon on quartz SAW mode in X_3 normalised using $\mathrm{Re}(\lambda_1)$. Stiffness tensors for both materials rotated in $x_1 - x_2$ by 0.81 rad. Normalised to the surface displacement $u_2(h)$, dotted lines denote the interface (at 0) and surface (at $\frac{1}{\mathrm{Re}(\lambda_1}$)) boundary conditions.

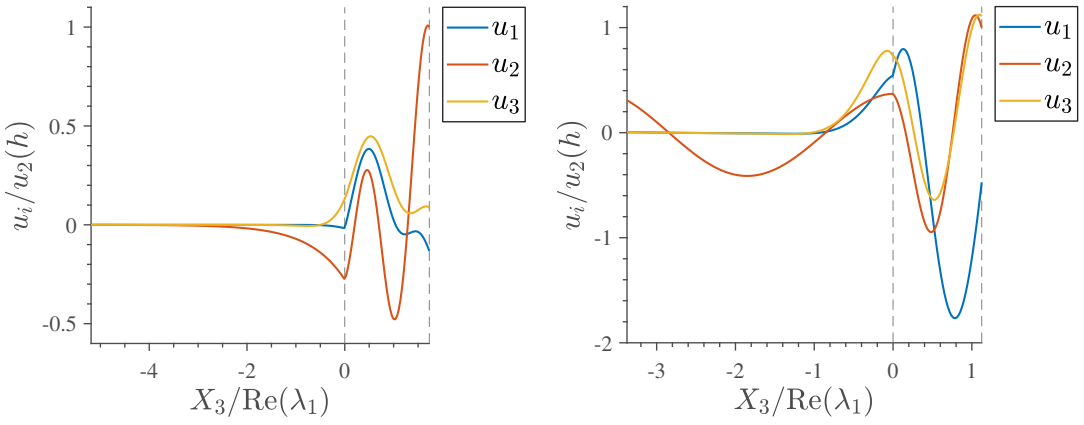

(a) 2nd mode at 4500ms^{-1} (b) 2nd mode at 4900ms^{-}1

Fig. 4.8 Displacements of 2nd silicon on quartz SAW mode in X_3 normalised using $\mathrm{Re}(\lambda_1)$. Stiffness tensors for both materials rotated in $x_1 - x_2$ by 0.81 rad. Normalised to the surface displacement $u_3(h)$, dotted lines denote the interface (at 0) and surface (at $\frac{1}{\mathrm{Re}(\lambda_1)}$) boundary conditions.

In the chosen direction of propagation, the modes presented in Figures 4.7 and 4.8 before the leaky wave transition are both generalised SAWs. After transiton the decaying structure in the substrate remain the same for the Rayleigh displacements U_1 and U_3, but now with a propagating horizontal shear component. For both modes, the substrate is now dominated by the shear waves due to the coupling of the shear bulk propagating partial wave. This behaviour is tied to the LSAW, quartz on silicon on a new substrate would allow Rayleigh displacements to propagate along the new interface, removing the horizontal shear dominance. These leaky structures are of interest to circular devices for mitigating energy leakage and possible novel devices, that may take advantage of the cyclic dispersive behaviour.

4.2.3 Fixed frequency surfaces

For biosensor applications, a fixed frequency data set is required for the design of IDTs for the excitation of waveforms at a uniform frequency. The fixed velocity approach is still useful for the fast computation of the existence problem and dispersion data. Computing this dispersion data is also the first step in computing fixed frequency surfaces, for the correct selection of a starting position. Presented in Figure 4.9 are the first three complete frequency curves between 4000ms^{-1} to 5200ms^{-1} with a 1μm thick layer.

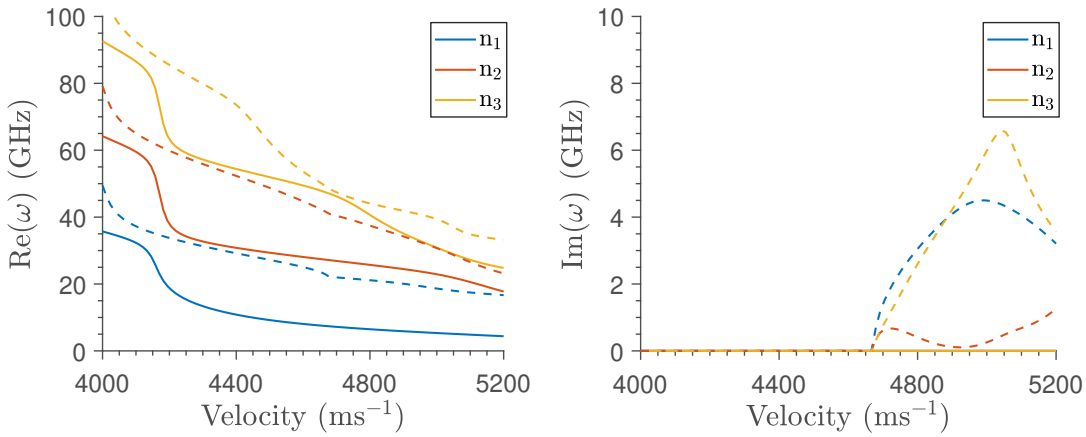

(a) Re(ω) (b) Im(ω)

Fig. 4.9 The (a) real and (b) imaginary parts of the frequency of the first four modes of 1μm thick Z-cut quartz layer on silicon (100) substrate with velocity. Data is computed for propagation angles 0 rad (solid) and $\frac{\pi}{4}$ rad (Dotted).

Using the hybrid search by golden sections with constant phase tracking, outlined in Section 3.4, the fixed frequency velocity data can be computed. Presented in Figure 4.10 are velocity

solutions computed for changes in propagation angle along the $X_1 - X_2$ surface for the first mode between fixed frequency values of 20GHz to 25GHz.

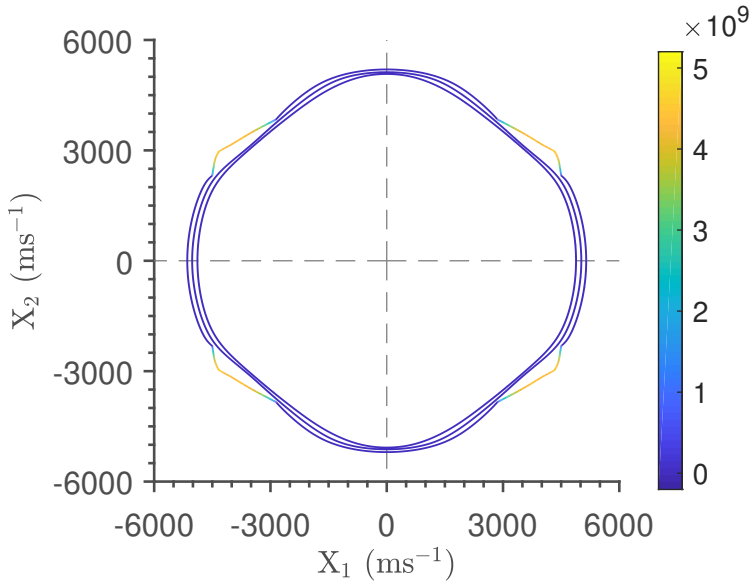

Fig. 4.10 For real fixed frequencies of 20GHz (outer), 23GHz (centre) and 25GHz (inner), the velocity surfaces have been computed for rotations in the $X_1 - X_2$ plane. For the case of 1μm thick Z-cut quartz on silicon (100), the colour map denotes the imaginary frequency.

In the non-leaky range the fixed frequency surfaces, at 20GHz and 23GHz, have a dominate 6-fold cyclic symmetry of the Z-cut quartz layer. Increasing the frequency to 25GHz over the leaky transition leads to angle dependent leaky behaviour at the same angles as the fixed velocity cases, as expected. This angular dependent leakiness increases the coupling to the 4-fold (100) silicon substrate, and breaks the dominant 6-fold structure. The novel problem shown here, is not typical of cylindrical biosensor design; in the next chapter a case which is closer to a real world application of these surfaces will be studied.

4.3 Conclusion

A common approach throughout the literature, is to model leaky behaviour by making use of a complex wavenumber. Unlike the non-leaky problem, the partial wave eigenvalues may be complex for velocities higher than the bulk velocities. The problem of transition from non-leaky to leaky behaviour, is considered in the case of quasi-6-fold Z-cut quartz on 4-fold (100) silicon. The bulk wave solutions in Section 2.5 hint that this combination will cause leaky transitions in particular directions, this has been shown to be true.

The overall symmetry of the combination is 2-fold, but the relative energy partitioning between the layers, will alter the dominant symmetries. The non-leaky case of a dominant 6-fold structure changing into a dominant4-fold, has been shown is due to only the waveguide and anisotropic dispersions. In the leaky transition case, the shift in symmetry is larger at particular angles, due to the increase depth of propagation into the substrate. Due to the anisotropic combination, the modes presented are generalised multilayered modes with some combination of Rayleigh and shear horizontal displacements. For the lowest mode a clear transiton between dominant 6-fold and dominant 4-fold symmetry is seen, at angles of leakiness this 4-fold shape is accentuated. The existence of high attenuated solutions were also noted and briefly discussed, these solutions are currently not of interest for biosensor application.

For biosensor applications, it is required that the slowness surfaces be computed using a fixed frequency value. For the same case of quartz on silicon, several fixed frequency velocity surfaces have been computed around the same transition point. The behaviour viewed in the fixed velocity surfaces is also present in the fixed frequency surfaces with the same angular dependent leakiness. These velocity surfaces play a important role for the design of annular IDTs on anisotropic crystals for cylindrical biosensor design, to be discussed further in Chapter 5. The possibility of using directional dependent bulk penetrating waveforms to dynamically activate embedded layers was briefly discussed. These concepts are beyond the scope of this research, but will be discussed briefly as further work in Chapter 8.

Chapter 5

Viscoelastic Waveguide and Shaped Annular Transducers

Biosensors are a combination of several different components including mechanical components, viscoelastic and biological. Viscoelastic components of biosensor design will have damped contributions which leads to time-dependent energy loss by internal friction mechanisms. When tailoring the waveforms for engineering applications these effects can not be ignored, in the case of resonant biosensors, the Q-factor (quality) is impacted. Damping in materials is studied using a 3-dimensional viscoelastic formulation which extends the formulations of Chapter 4. The effect of frequency dependency on the partial wave solutions is investigated, this dependency will alter the numerical approach. The computation of fixed frequency velocity surfaces, started in Chapter 4, is extended in this chapter to illustrate the design process of shaped annular transducers. The effect of the anisotropy of particular crystal symmetries is studied along with the potential impact to these annular transducer designs.

5.1 Formulation of Viscoelastic Waveforms

Biosensors are constructured using a combination of mechanical, electrical and biological elements. These biological and mechanical elements can contribute to the energy loss of the waveform due to their viscoelastic properties. The viscoelastic behaviour of the waveguide, [1, 2] and biological binding site [3–5] can contribute to the overall attenuation of the waveform. Depending on the anisotropy of the material, the impact of viscoelastic damping may have cyclic dependence, also impacting the effective electromechanical coupling [6] in particular directions. For these cases the viscoelastic behaviour will therefore, in addition to waveguide and anisotropic

dispersion, alter the solution surfaces of wave modes in a cut. The common motivation behind studying the viscoelastic behaviour is to reduce the energy loss for traditional biosensor designs, particularly layered devices [7–9]. In other applications, such as constrained layer damping, the viscoelastic properties are tailored to attenuate energy at particular excitation frequencies [7, 8]. This behaviour also has the potential to be used as a sensing mechanism in biosensor technology due to rapid frequency shifts and modal degeneracy breaking.

5.1.1 Viscoelastic damping in equation of motion

So far in this work the analysis has been focused on only elastic materials in which the stresses instantaneously result in a strain response. Viscoelastic materials are a combination of the elastic response and the viscous property which is a measure of the resistance to change. Due to this the stress-strain response in viscoelastic materials is now time-dependent, giving rise to creep and relaxtion behaviours [9]. The linear viscoelastic behaviour may be introduced into the wave equation through several different approaches in the constitutive relationship, see Appendix A.

The numerical methods developed in Chapter 3 are sufficient for solving the resulting eigenvalue problems which will be discussed. The choice of approach is therefore dependent on which viscoelastic behaviours are trying to be captured by the model and the amount of material data that is available.

The first approach is a full model by capturing the viscoelastic behaviour in rank-4 tensor similar to the stiffness [10],

$$\sigma^{ij} = C^{ijkl}\varepsilon_{kl} + \mu^{ijkl}\frac{\partial \varepsilon_{kl}}{\partial t}, \tag{5.1}$$

where μ^{ijkl} captures viscous behaviour. The viscoelastic equation of motion using this form for the stress is,

$$C^{ijkl}\frac{\partial^2 u_l}{\partial x^j \partial x^k} + \mu^{ijkl}\frac{\partial^3 u_l}{\partial x^j \partial x^k \partial t} = \rho\frac{\partial^2 u^i}{\partial t^2}. \tag{5.2}$$

Assuming a solution in the form (4.1) results in an eigenvalue problem with an additional frequency dependent term,

$$\left[(C^{ijkl} + \mathrm{i}\omega\mu^{ijkl})(m_j + pn_j)(m_k + pn_k) - \rho v^2 \delta_i^l\right] A_l = 0. \tag{5.3}$$

Another approach seen in the literature uses a reduced form by introducing imaginary terms into the stiffness tensor, typically the materials are isotropic. For these isotropic materials the

shear modulus is a common variable used to introduce an imaginary part to capture the shear loss effects. The shear modulus is a combination of the shear storage G' and shear loss G'',

$$G = G' + \mathrm{i}G''. \tag{5.4}$$

A similar loss modulus can also be introduced into Young's modulus, but typically for biosensor applications only the shear loss modulus is considered. For waves propagating in biosensors, the energy loss occurs in waveguide materials which are assumed to be thin film leading to damped behaviour, dominated by the in-plane displacements. The frequency dependence in the equation of motion will no longer exist in this approach, instead the shear modulus is now a function of frequency; typically using a relaxtion function. Unlike (4.2) for a real wavenumber, the partial wave determinant will already have an inital rotation into the complex plane breaking the conjugate symmetry.

5.2 Characterisation of Damped Loss

Viscoelastic behaviour will be modelled using the viscosity of the material, and solving (5.2) using the assumed form (4.1). This approach will be similar to the modelling of linear fluid behavior in Chapter 6, except a pressure waveform is not generated in this case. SU-8 photo-resist will be used as the viscoelastic waveguide throughout this section, it is an isotropic epoxy-type material. The properties of this material significantly vary depending on the processes used to layer SU-8 in MEMS devices, see [11].

5.2.1 Frequency dependence on partial wave solution

The viscoelastic form of the constitutive equation presented in (5.1) introduces frequency dependence in the equation of motion and boundary condition procedure. The partial wave solutions, need to be computed for each step of the boundary conditon for each viscoelastic layer, computating these changes is numerically inefficient. The order of magnitude of the viscoelastic coefficients is approximately nine times smaller than the stiffness coefficients. The viscoelastic behaviour will only have an effect on the partial wave and boundary solutions for high order of magnitude frequency values. The mechanism is similar to the constrained layer damping mechanism in which the thicknesses of the viscoelastic layers is tailored to particular wavelengths corrsponding to lossy frequency ranges. The shear viscosity, denoted η, of SU-8 in [11] depending on the type is either 0.059, 1.5 or 15 Pa·s. Figure 5.1 presents the change in

partial wave solution for SU-8, with change in frequency between these values of viscosity at a velocity above the bulk wave velocities.

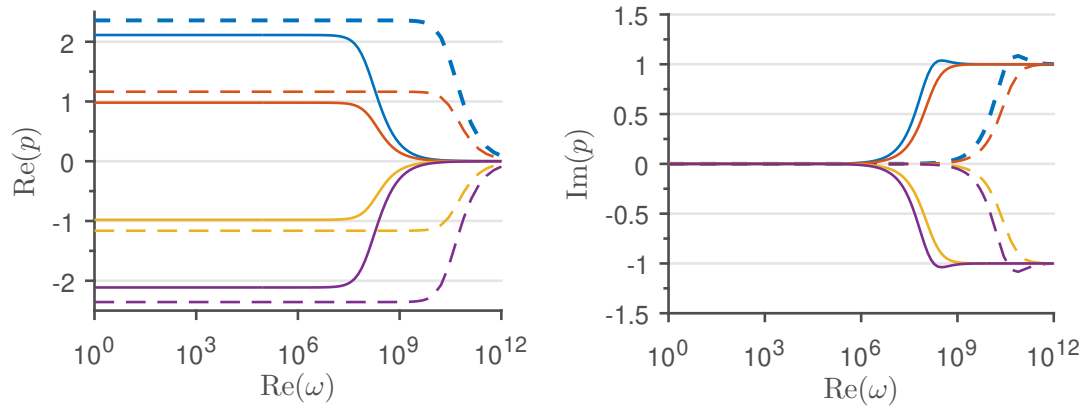

(a) Re(p) (b) Im(p)

Fig. 5.1 Presented is the change in partial wave solutions of SU-8, with change in frequency for different values of shear viscosity η at a velocity of 3000ms^{-1} above the bulk wave velocities. Solid lines are $\eta = 15$ Pa·s and dashed lines are $\eta = 0.059$ Pa·s.

The partial waves, at a frequency that is dependent on the viscosity, switches from real to imaginary values which corresponds to a rotation of the solutions back into the complex, similar to Figure 4.1. This switching may be visulised as the wave transitioning from propagating sinusoidal behaviour to expontial decay. The point of switching can be clearly shown on a log-log scale shown in Figure 5.2, the frequency at this point is denoted ω_η the switch frequency.

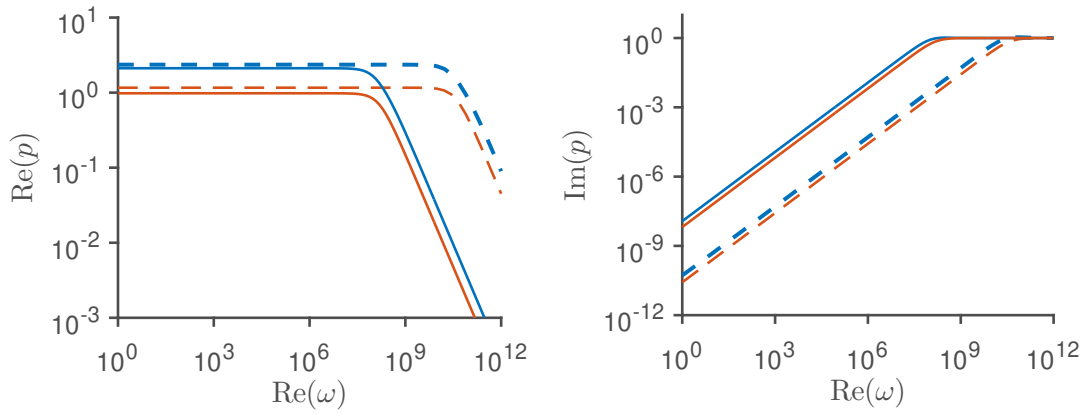

(a) Re(p) (b) Im(p)

Fig. 5.2 Presented is the change in partial wave solutions of SU-8, with change in frequency on a log-log plot for different values of shear viscosity η at a velocity of 3000ms^{-1} above the bulk wave velocities. Solid lines are $\eta = 15$ Pa·s and dashed lines are $\eta = 0.059$ Pa·s.

For $\eta = 15$ Pa·s the switching occurs approximately within the range $10^7 < \omega_\eta < 10^8$ corrsponding to a wavelengths around the 100μm range. For the lower viscosity of $\eta = 0.059$ Pa·s, the switching range is higher at $10^{10} < \omega_\eta < 10^{11}$, within the μm range for wavelength. For both cases the lossy behaviour occurs in wavelength ranges that are within common guidewave thicknesses for biosensor application, typically the μm range. The guidewave at these thicknesses are perfect for attenuation of the propagating SAWs, this would lead to a significant decrease in the biosensor Q-factor. The correct excitation frequency should be chosen, so that the nautral frequency is in the non-lossy range, so that the damping ratio is as low as possible. In addition, the changes in the velocity have a insignificant effect on ω_η, see Figure 5.3 for a comparison of velocities. Therefore, for viscoelastic behaviour, the selection of frequency and velocity can be assumed independent for the isotropic partial solutions.

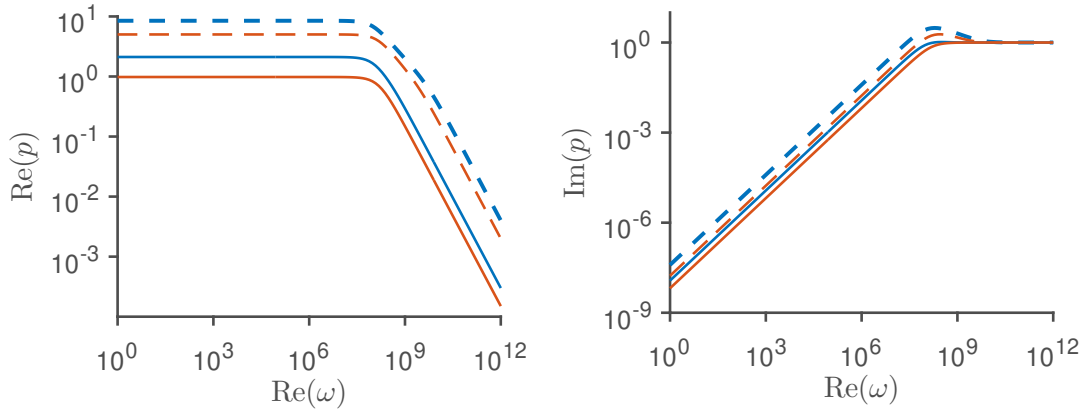

(a) Re(p) (b) Im(p)

Fig. 5.3 Presented is the change in partial wave solutions of SU-8 with change in frequency for different velocities for fixed viscosity of $\eta = 0.059$. Solid lines are at $v = 3000$ ms-1 and dashed lines are at $v = 10000$ ms-1.

Inspecting the partial wave solutions not only gives clear insight into the possible ranges of lossy behaviour of a material, but also the computational approach that should be taken. When the frequency is smaller or larger than ω_η, the changes in partial wave solutions, for the case of SU-8, are predictable. For $\omega < \omega_\eta$ Re(p) does not change and the change in Im(p) is insignificant compared to the Re(p) within the limit as ω approaches ω_η. For these ranges the boundary conditon solutions may be accurately tracked by only computating the partial solutions once, using the phase tracking procedure. For ranges around ω_η the propagating partial waves rapidly switch to expontial decaying waves, this change must be tracked but this is inefficient. A more desirable approach is to apply the phase tracking procedure, to small enough regions in which

the change in partial wave solution is negligible. The change in partial values between regions must be small enough to approximately connect the surface together without discontinuities.

5.2.2 Effect of lossy term on damping of generalised modes

Presented is the case of plane wave propagagtion in the half space geometry, 1μm thick SU-8 with $\eta = 0.059$ is layered on Z-cut lithium niobate. Lithium niobate is in the trigonal crystal class, it has a 3-fold rotational symmetry but in the Z-cut the bulk solutions have a 6-fold cyclic symmetric, termed quasi-6-fold. The velocity is set to 3000ms^{-1} above the bulk wave solutions of SU-8 and below the bulk solutions of lithium niobate. The resulting modes are generalised multilayered waveforms indistinguishable from the isotropic cases covered in Chapter 2. The attenuation is dependent on propagation angle, all the modes in this case are lossy which results in the tilting of the solution surface off the real axis, this is clearly shown in the first computed mode see Figure 5.4, modes ordered by magnitude of Re(k).

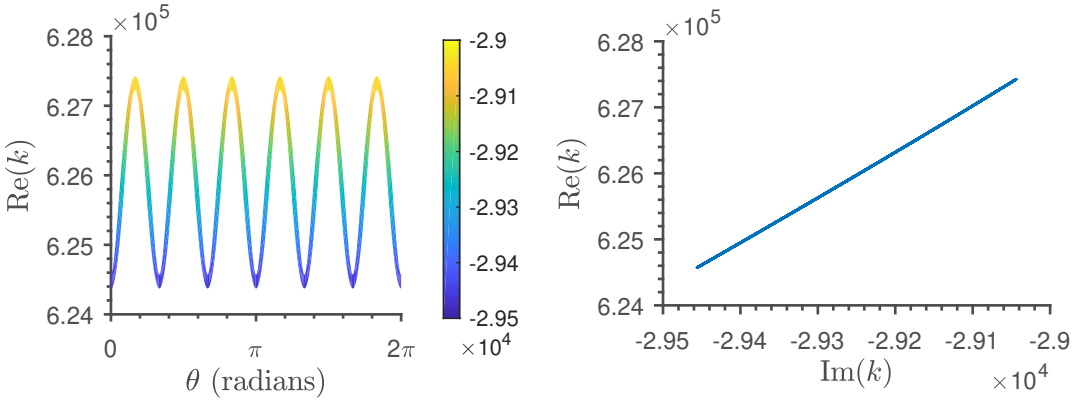

(a) Angle

(b) Complex plane

Fig. 5.4 Presented is the 1st computed mode for SU-8 on lithium niobate, (a) change in Re(k) with propagation angle θ, colour map denotes Im(k). In (b) the solutions presented in (a) shown in the complex plane of k.

Modes are not required to have the uniform tilting, non-uniform attenuation $\alpha = \text{Im}(k)$ leads to a breakage of the symmetry projected onto the real plane. Figure 5.5 shows the seventh computed mode in which the quasi-6-fold cyclic symmetry of the lithium niobate is twisted into 3-fold. Trigonal crystals has 3-fold cyclic symmetry, although the bulk wave solutions of the Z-cut show a 6-fold rotational symmetry. This is a quasi-6-fold symmetry which is dependent on the wave types, for example a horizontal shear SAW would also have a quasi-6-fold structure.

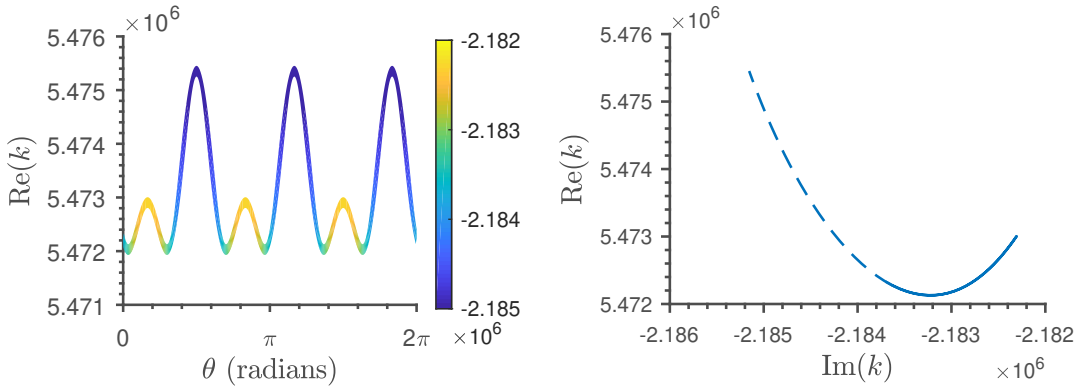

(a) Angle (b) Complex plane

Fig. 5.5 Presented is the 7th computed mode for SU-8 on lithium niobate, (a) change in Re(k) with propagation angle θ, colour map denotes Im(k). In (b) the solutions presented in (a) shown in the complex plane of k, solid line for the range $0 < \theta < \frac{2\pi}{6}$ and dotted line for $\frac{2\pi}{6} < \theta < \frac{2\pi}{3}$.

A change in symmetry from quasi-6-fold to 3-fold is seen in this simple case of a viscoelastic isotropic layer on a high symmetry, low variation cut. Another mode of interest is the sixth computed mode which has a wavenumber close to the seventh mode, presented in Figure 5.6. This mode exhibits the same attenuated behaviour, but now the odd and even peaks have been twisted in reverse directions which results in a flipping of the symmetry shown in Figure 4.4. Note this case is only symmetric in Re(k) not Im(k), the attenuation varies with a different symmetry.

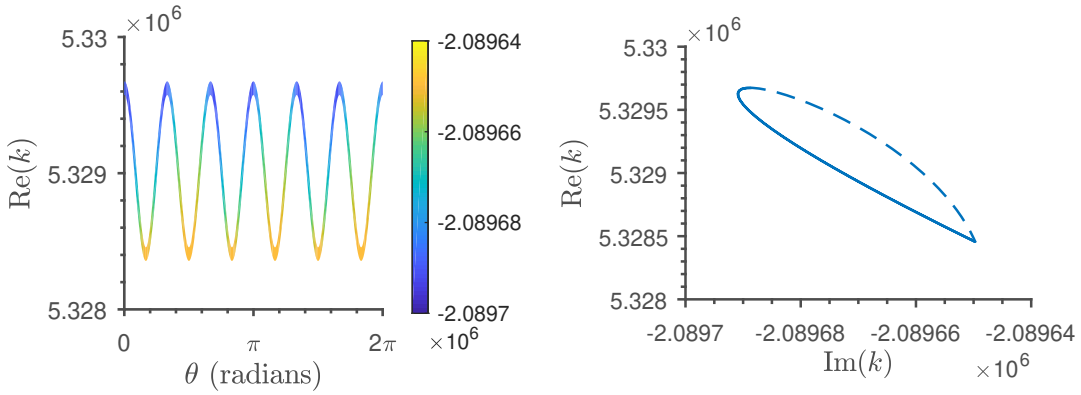

(a) Angle (b) Complex plane

Fig. 5.6 Presented is the 6th computed mode for SU-8 on lithium niobate, (a) change in Re(k) with propagation angle θ, colour map denotes Im(k). In (b) the solutions presented in (a) shown in the complex plane of k, solid line for the range $0 < \theta < \frac{2\pi}{6}$ and dotted line for $\frac{2\pi}{6} < \theta < \frac{2\pi}{3}$.

5.3 Annular Transducer for Lithium Niobate

In this section the problem of annular transducers for excitation of waveforms in cylindrical geometry is considered. The methods developed up to this point are in the form of plane propagating waves. The methodology used here takes advantage of this formulation by assuming plane fronted waves in the far field. The method uses the precomputed slowness diagrams to approximate the Green's function for a point loading that propagates SAWs into the far field [12–14].

The goal is to design a transducer using the Green's functions that does the reverse, focusing plane waves onto a central point for biosensor application. For isotropic materials there is no cyclic dispersion, therefore the phase and group velocities do not vary, and a circular transducer may be used. In the case of anisotropy, this is no longer the case and an annular transducer based on the slowness shape must be developed.

In the literature, only the half-space problem has been considered, applying a layer also adds waveguide dispersion. This will alter the structure of the slowness structure in the third frequency axis, in the half-space case these structures are uniform slowness cylinders. Even though the inital research into the half-space transducer design exists, literature in this area is limited and does not exist for the layered case.

5.3.1 Effect of piezoelectric coupling

The solution surfaces computed throughout this work are purly mechanical, neglecting the effects of the piezoelectric materials. The piezoelectric coupling can be introduced to get a more accurate picture of the slowness surface for these layered structures. Instead, in the approach taken here, it is assumed that the variation due to the piezoelectric coupling is small. Provided the error is small, then the mechanical slowness surfaces will be sufficient for a first concept. Piezoelectric slowness surfaces may be computed in the future for further optimisation of the transducer designs, if required.

The error must be small enough per cycle of the oscillatory waveform to not significantly impact the excitation of the overall mode, number of cycles is dependent on the size of the device. The error is dependent on the piezoelectric coupling coefficient of the materials in the multilayered structure, the larger the coupling the larger the variation. As shown in Chapter 2, quartz has a relatively low piezoelectric coupling opposed to lithium niobate which has high coupling. The error in slowness data due to the piezoelectric coupling will be checked at particular angles for both of these materials in Chapter 7.

The piezoelectric coupling strength between particular applied electric fields and stresses will not be considered in the design of the transducer. The main reason for neglecting this is due to the current limitations in transducer designs, even if the variation in piezoelectric coupling is known, it can not be controlled in the annular transducers that will be presented. More sophisticated annular or grid based IDT designs will need to be developed, which is currently beyond the scope of the work presented but will be discussed further in Chapter 8.

5.3.2 Half-space shaped annular transducer design

The starting point for the annular transducer design is the fixed freqency slowness diagram, for half-space waveforms, the solution only exists at particular velocity values. The solution for every propagation angle is searched in the velocity domain, these solutions are non-dispersive. In this case, for Z-cut lithium niobate, a velocity surface may be computed for a non-leaky Rayleigh type waveform, presented in Figure 5.7.

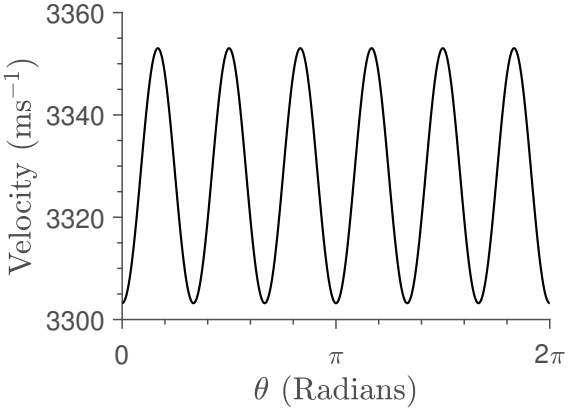

Fig. 5.7 The velocity surface for a generalised non-leaky Rayleigh wave solution in Z-cut lithium niobate half-space.

The velocity surface is computed using the elastic formulation, the slowness is the reciprocal of this surface, ignoring the effect of the piezoelectric coupling. As seen in Section 2.5.3, the coupling in lithium niobate can have significant effects on the bulk solutions, unlike quartz. The annular transducer pattern will be designed by not considering the piezoelectric coupling in the slowness computation and Green's function. The impact of this will be investigated with comparison to some piezoelectric computations and the literature.

Using the data surface of lithium niobate, in Figure 5.7, the Green's function may be computed and used for shaped transducer designs. An example of a shaped annular transducer using this data is presented in Figure 5.8, designed by Dr H.T. Grigg as a collaboration. The curvature of this particular design has been increased by a rough factor of ten to emphasise the anisotropic

structure which would not be visible but still relevant. This procedure may be automated, an input slowness curve can be processed into a shaped transducer. Several design parameters may also be automated in this computation process, for example the number of reflectors, allowing fine tune control of the design process. The real advantage of this comes when combined with a robust slowness surface computation method and adequate MEMS production facilities.

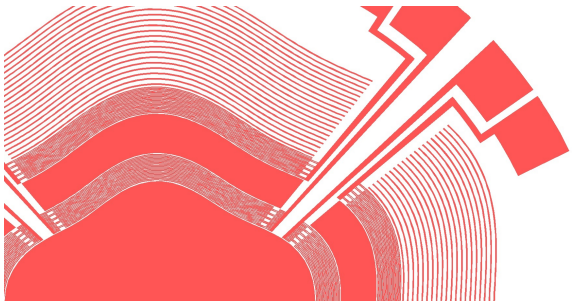

Fig. 5.8 A portion of the shaped annular transducer design for a non-leaky SAW mode in the half-space of lithium niobate. Elements include reflectors at the outer most radius, two sets of interdigital transducers and sites for analyte functionalisation.

5.3.3 Slowness curves of SU-8 on lithium niobate

Using the hybrid phase tracking and golden sections method, developed in Section 3.4, the fixed frequency velocity surface for SU-8 on lithium niobate are computed. For this case the behaviour of the modes are dependent on the anisotropy of the substrate, dispersion due to the layer and viscoelastic parameters of the layer. It is expected, due to the dominant layer dynamics, that the wave structure is dependent mostly on layer properties, which are isotropic but viscoelastic.

Several cases are shown to illustrate some of the factors that need to be considered when designing annular transducers for a viscoelastic layered piezoelectric crystal. Starting with the case of shear viscosity $\eta = 0.059$Pa·s, the dispersion of the first four modes is presented in Figure 5.9, within the first and second bulk velocity of SU-8.

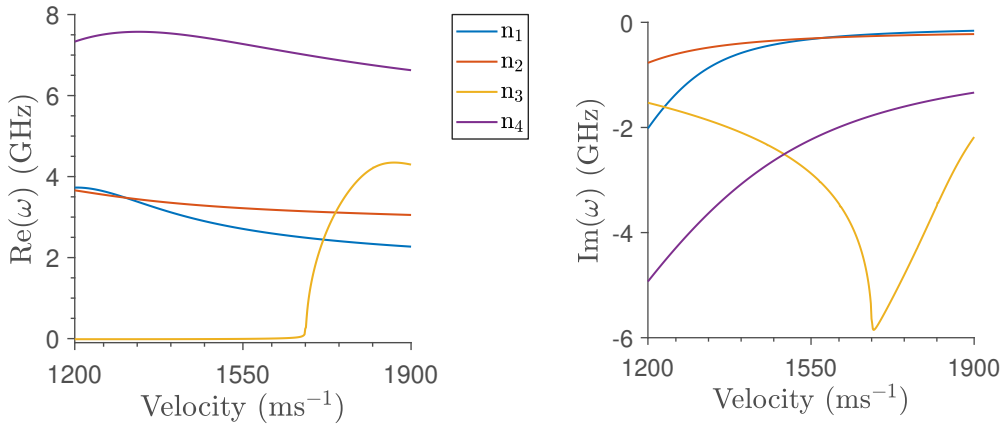

(a) Re(ω) (b) Im(ω)

Fig. 5.9 The (a) real and (b) imaginary parts of the frequency of the first four modes of SU-8 ($\eta = 0.059$Pa·s) on Z-cut lithium niobate for velocities. Velocity range is between the first and second bulk wave solutions of SU-8.

For the first mode, from right to left, the velocity surface for rotation of propagation angle θ around the cut is presented in Figure 5.10. The velocity surface is computed for a fixed frequency of 2.7GHz.

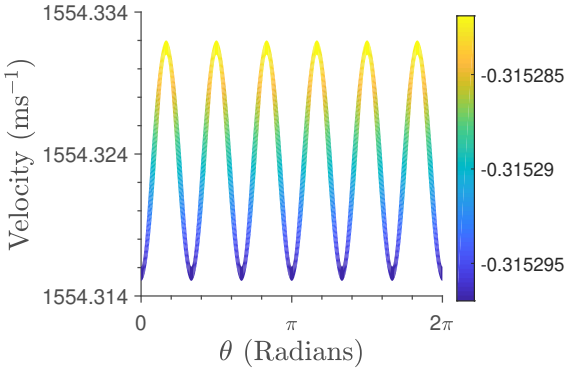

Fig. 5.10 The velocity surface computed for multiple angles within the surface of SU-8 ($\eta = 0.059$Pa·s) on Z-cut lithium niobate. Velocities are computed at a fixed frequency of 2.7GHz with colour map denoting imaginary frequency.

The major point to highlight for this case, is that the velocity variation between the maximum and minimum is only 0.0159ms^{-1}. This compared to the half-space case, which is roughly a difference of 50ms^{-1}, this may be considered insignificant for IDT design. This is a case in which the cyclic dispersion caused by anisotropic stiffness is small due to the dominant isotropic layer. Assuming the annular transducer to be circular, will induce an error per cycle of the propagating waveform. This error may be insignificant compared to other sources such as design imperfections, or the error in electrical components of the device.

For the third mode, in Figure 5.9, a high attenuation peak exists which rapidly changes both the real and imaginary parts of the frequency. Presented in Figure 5.11 is the change of the first four modes with change in shear viscosity, at a constant velocity of 1900ms^{-1}.

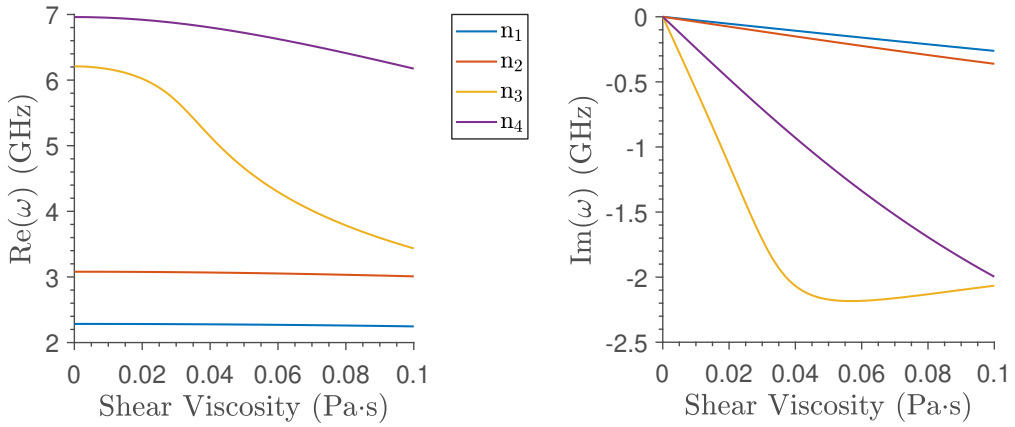

(a) Re(ω) (b) Im(ω)

Fig. 5.11 Presented is the change in the (a) real and (b) imaginary parts of the frequency solutions, for the first four modes of SU-8 on Z-cut lithium niobate, with changing shear viscosity. The velocity is set at 1900ms^{-1}

On inspecting the change of these modes, with change in the shear viscosity, it becomes clear that the third mode becomes highly attenuated close to $\eta = 0.059$Pa·s. Unlike the other modes this produces a small velocity range in which the real frequency rapidly changes, which might prove desirable for a leaky biosensor. For a fixed frequency annular transducer design the structure of the velocity surface also rapidly changes over this range. The novelty that may come from this is once again irrelevant due to the small velocity variation of the solutions in the isotropic layers. In fact this viscosity curve and the dispersion curves, are near identical between the Z-cut lithium niobate and quartz cases, illustrating that the substrate material plays almost no significant role in the cyclic symmetry. From the point of view of a degenerate mode biosensor, this behaviour is ideal for propagating cyclic degenerate modes, provided that the desired waveform may be excited. The mean error difference between the numerical results using the tracked frequency and fixed frequency approaches, discussed in Section 3.4.3, is $5.1454\text{x}10^{-5}$ checked for the third mode at 4GHz.

Next is the case of SU-8 on lithium niobate with a higher shear viscosity of $\eta = 1.5$Pa·s, the disperion curves are presented in Figure 5.12.

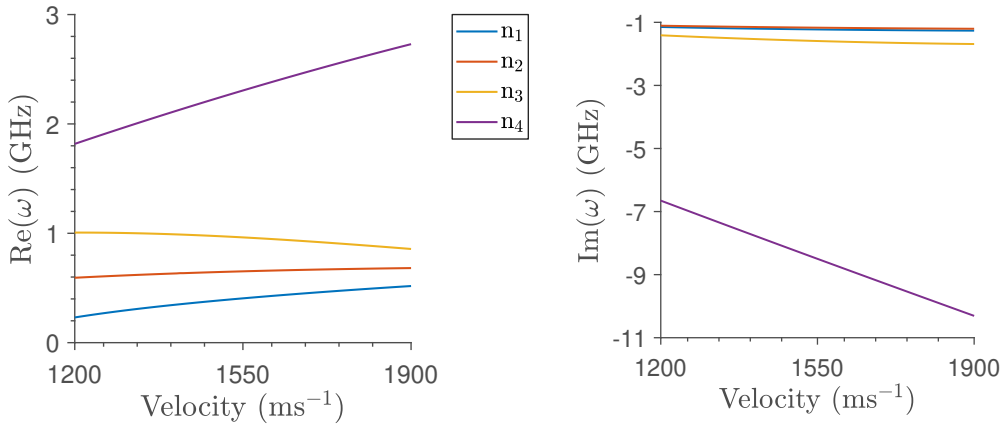

(a) Re(ω)

(b) Im(ω)

Fig. 5.12 The (a) real and (b) imaginary parts of the frequency of the first four modes of SU-8 ($\eta = 1.5$Pa·s) on Z-cut lithium niobate for velocities. Velocity range is between the first and second bulk wave solutions of SU-8.

The fixed frequency velocity surface is computed with rotation in propagation angle, presented in Figure 5.13, for a fixed frequency of 0.4GHz.

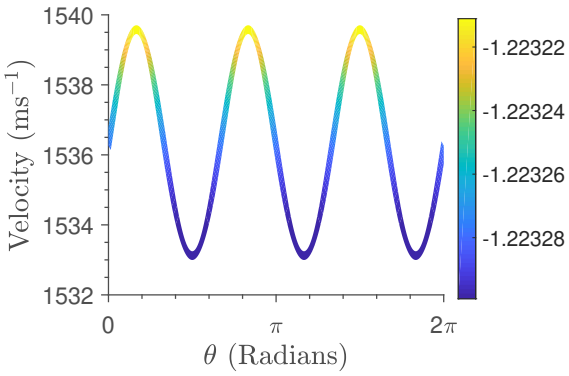

Fig. 5.13 The velocity surface computed for multiple angles within the surface of SU-8 ($\eta = 0.059$Pa·s) on Z-cut lithium niobate. Velocities are computed at a fixed frequency of 0.4GHz with colour map denoting imaginary frequency.

The increased viscoelastic parameter combined with the lower frequency of 0.4GHz, due to dispersion, has lead to a situation with an increased velocity variation of roughly 6.5ms^{-1}. In this case, the imaginary part of the frequency is much higher than the real part, the velocity surface has twisted from quasi-6-fold cyclic symmetry to 3-fold cyclic symmetry. In this case, even though the layer is isotropic, if a circular transducer is used the viscosity of the layer increases the variation in velocity, which increases the error per cycle.

5.4 Conclusion

The visocelastic extension has been made to the leaky formulation of Chapter 4, and the frequency dependent behaviour of the resulting partial wave solutions discussed. At a particular frequency the coupling of the viscoelastic tensor becomes large enough to effect the partial wave solution, rotating the partial waves in the complex plane. For real propagating partial waves, at velocities above the corresponding bulk velocity, this rotation sees a transition from propagating to decay behaviour. For the problem of an isotropic viscoelastic layer on anisotropic lithium niobate, the slowness structure may be altered by the attenuation. Cases are presented in which this alteration, is an uniform rotation leading to uniform compacting of the slowness shape projected in the real axis. In other cases, the attenuation varies with the propagation driection, this causes a twisting behaviour in the complex plane of the wavenumber, changing the symmetry from quasi-6-fold to 3-fold.

For biosensor application, the problem of high frequency multilayered waveforms in viscoelastic layered Z-cut lithium niobate is considered. The annular transducer design for a generalised non-leaky Rayleigh wave on a Z-cut lithium niobate half-space has been presented. In the case of SU-8 viscoelastic layer, the isotropic behaviour dominates the dynamics, reducing the velocity variation closer to the isotropic case. Some cases are presented of large velocity vairation due to the viscoelastic twisting of the quasi-6-fold symmetry into 3-fold. In some of these cases, a shaped annular transducer may be required, but typically the isotropic layer will dominate. The key point is the large energy loss in biosensors with a viscoelastic layer, this will be considered further in Chapter 7.

Chapter 6

Linear Fluid Waves and Material Compatibility

SAW biosensors orginated as an attempt to transfer the techniques developed for Rayleigh wave based gas sensors. These attempts were unsuccessful due to the increased energy loss of these devices when a liquid was applied to the surface. Rayleigh wave type displacements, have an out-of-plane displacement, which couples to the fluid to generate pressure waves in the fluid, that propagate energy away from the surface. Shear horizontal wave types such as the Love wave in isotropic media, are significantly less attenuated by the presence of a fluid layer. This perceived view of the physics is based on traditional biosensor designs and 1-dimensional isotropic models of the solid-fluid interface problem. As discussed in Chapter 2, anisotropic stiffness contributions in the multilayered combination, can lead to generalised wave types containing both shear horizontal and Rayleigh type displacements.

In this chapter, a 3-dimensional fluid loading model is developed based on a small signal approximation to linearise the continuity and momentum equations. The goal is to develop a model capable of providing quantitative results and to further the insight of these isotropic waveforms. Along with their generalised anisotropic extensions, for which the behaviour is not well understood or modelled, all providing a novel contribution to this thesis. The pressure wave displacement is introduced into the eigenvalue problem as a fourth displacement field coupled to the wave motion in the solid. The methods for attenuated waveforms developed in Chapter 4 and 5 are expanded to the fluid case. The objective is to study the effect of fluid loading on the waves propagating at the surface of an anisotropic media, less interest is placed on the behaviour of the fluid.

6.1 Fluid Mathematical Formulation

6.1.1 Linearisation and mass continunity

The following formulation of the equation of state, and linearisation by small-signal approximation is based on methods from [1]. It is assumed that pressure is only dependent on the density, changes in temperature are not considered, the series expansion of the isentropic equation of state is given,

$$P = {c_0}^2(\rho - \rho_0)\left[1 + \frac{B}{2!A}\left(\frac{\rho - \rho_0}{\rho_0}\right) + \frac{C}{3!A}\left(\frac{\rho - \rho_0}{\rho_0}\right)^2 + \cdots\right]. \tag{6.1}$$

Pressure and initial presure are denoted P and $P_0 = {v_0}^2(\rho - \rho_0)$, density and initial density are denoted ρ and ρ_0. The speed of sound, of the fluid, is assumed to remain constant using a small-signal approximation, this constant speed is denoted c_0. A small disturbance in the density $\delta\rho$ and by extension pressure δP is taken,

$$\rho = \rho_0 + \delta\rho, \tag{6.2}$$

$$P = P_0 + \delta P. \tag{6.3}$$

A requirement of the linearisation is that these changes are insignificantly small in $\delta\rho << \rho$ and $|\delta P| << \rho_0 {c_0}^2$, neglecting higher order term in (6.1). This would then impose a maximum limit on the magnitude of the displacements of the fluid wave equation of motion, making large wavelength formulations less reliable. However, the linearity as a result of this small-signal approximate will be valid for ranges of interest for biosensor application, typically micrometre to picometre ranges.

The statement of mass continuty for a system leads to,

$$\frac{\partial\rho}{\partial t} + \frac{\partial\rho V_i}{\partial x_i} = 0, \tag{6.4}$$

which describles the change in density of a fluid, where V_i denotes the particle velocity. Substituting (6.2) into (6.4) results in,

$$\frac{\partial(\rho_0 + \delta\rho)}{\partial t} + \frac{\partial(\rho_0 V_i + \delta\rho V_i)}{\partial x_i} = 0, \tag{6.5}$$

expanded and removing any derivatives of constants,

$$\frac{\partial \delta\rho}{\partial t} + \delta\rho\frac{\partial V_i}{\partial x_i} + V_i\frac{\partial \delta\rho}{\partial x_i} + \rho_0\frac{\partial V_i}{\partial x_i} = 0. \tag{6.6}$$

The quantities δP, $\delta\rho$ and V_i are assumed to be small and any products of these terms is neglectable,

$$\frac{\partial \delta\rho}{\partial t} + \rho_0\frac{\partial V_i}{\partial x_i} = 0. \tag{6.7}$$

The equation of state (6.1) also reduces to,

$$P = {c_0}^2\delta\rho. \tag{6.8}$$

Substituting (6.8) into (6.7) results in,

$$\frac{1}{{c_0}^2}\frac{\partial P}{\partial t} + \rho_0\frac{\partial V_i}{\partial x_i} = 0. \tag{6.9}$$

6.1.2 Linear fluid wave equation

The approach to modelling the fluid in this thesis now differs from [1], in which the 3-dimensional model is simply an expanded 1-dimensional model. This would ignore the interaction of the shears, which is a key component of studying these waveforms, the formulation must therefore start from the 3-dimensional constitution. A novel approach will have to be developed to numerically solve the resulting system of equations for the desirable displacement information, instead of the pressure waveform.

The fluid stress constitution is a combination of the hydrostatic pressure and isotropic viscosity terms. The viscosity tensor of Chapter 5 is used to capture all direct and shear interactions in the following form,

$$\sigma^{ij} = -P\delta^{ij} + \mu^{ijkl}E_{kl}. \tag{6.10}$$

Unlike the elastic or viscoelastic formulations the stiffness is zero and so, there are no direct or shear stresses due to elasticity. The derivative of the strain tensor is denoted E_{kl} the strain rate tensor,

$$E_{kl} = \frac{1}{2}\left(\frac{\partial V_k}{\partial x_l} + \frac{\partial V_l}{\partial x_k}\right). \tag{6.11}$$

Substituting (6.10) into the equations of motion results in,

$$-\frac{\partial P}{\partial x_j}\delta^{ij}+\mu^{ijkl}\frac{\partial^2 V_l}{\partial x^j\partial x^k}=(\delta\rho+\rho_0)\dot{V^i}. \tag{6.12}$$

The derivative of the velocity term can be found using the kinematic expression for acceleration [2],

$$\dot{V_i}=\frac{\partial V_i}{\partial t}+V_j\frac{\partial V_i}{\partial x_j}. \tag{6.13}$$

Substituting (6.13) into (6.12) and expanding results in,

$$-\frac{\partial P}{\partial x_i}+\mu^{ijkl}\frac{\partial^2 V_l}{\partial x^j\partial x^k}=\delta\rho\left[\frac{\partial V^i}{\partial t}+V^j\frac{\partial V^i}{\partial x^j}\right]+\rho_0\left[\frac{\partial V^i}{\partial t}+V^j\frac{\partial V^i}{\partial x^j}\right]. \tag{6.14}$$

Similar to the continuty of mass, products of small terms are assumed to be negligible resulting in the final form for the equations of motion,

$$-\frac{\partial P}{\partial x_i}+\mu^{ijkl}\frac{\partial^2 V_l}{\partial x^j\partial x^k}=\rho_0\frac{\partial V^i}{\partial t}. \tag{6.15}$$

6.1.3 Coupled eigenvalue problem

The equations of motion (6.15) and mass continuity equation (6.9) must be solved as a set of coupled equations. Substituting the displacements into these leads to the set of equations,

$$-\frac{\partial P}{\partial x_i}+\mu^{ijkl}\frac{\partial^3 u_l}{\partial x^j\partial x^k\partial t}=\rho_0\frac{\partial^2 u^i}{\partial t^2}, \tag{6.16}$$

$$\frac{1}{{c_0}^2}\frac{\partial P}{\partial t}+\rho_0\frac{\partial^2 u_i}{\partial x_i\partial t}=0. \tag{6.17}$$

The solution to the displacements and pressure is assumed in the same form as (4.1),

$$u_i=A_i\mathrm{e}^{-(\mathrm{i}\beta-\alpha)(\boldsymbol{m}\cdot\boldsymbol{x}+p\boldsymbol{n}\cdot\boldsymbol{x})+\mathrm{i}\omega t}, \tag{6.18}$$

$$P=A_4\mathrm{e}^{-(\mathrm{i}\beta-\alpha)(\boldsymbol{m}\cdot\boldsymbol{x}+p\boldsymbol{n}\cdot\boldsymbol{x})+\mathrm{i}\omega t}, \tag{6.19}$$

Substituting (6.18) and (6.19) into (6.16) and (6.17) results in,

$$\begin{aligned}&\mathrm{i}\omega(\mathrm{i}\beta-\alpha)^2\mu^{ijkl}\left(m_j+pn_j\right)\left(m_k+pn_k\right)A_l-(\mathrm{i}\beta-\alpha)\left(m^i+pn^i\right)A_4\\&-\rho_0\omega^2A_i=0,\end{aligned} \tag{6.20}$$

$$A_4 - \rho_0 {c_0}^2 (\mathrm{i}\beta - \alpha)(m^i + pn^i) A_i = 0. \tag{6.21}$$

Substituting (6.21) into (6.20) results in the combined eigevalue characteristic for displacement amplitudes,

$$\begin{aligned} &\left(\mathrm{i}\omega\mu^{ijkl}\left(m_j + pn_j\right)\left(m_k + pn_k\right) - \rho_0 {c_0}^2\left(m^i + pn^i\right)\left(m^l + pn^l\right)\right. \\ &\left.-\rho_0 v^2 \delta_i^l\right) A_l = 0. \end{aligned} \tag{6.22}$$

6.1.4 Fluid partial waves

Throughout this chapter the fluid used in the loading is water [3], the properties of which may be assumed to be linear under the Newtonian fluids assumption. The eigenvalue problem (6.22) may be solved using the same numerical methods developed in Chapter 3. The partial wave solutions for a fluid are initially complex, see Figure 6.1 for the case of water.

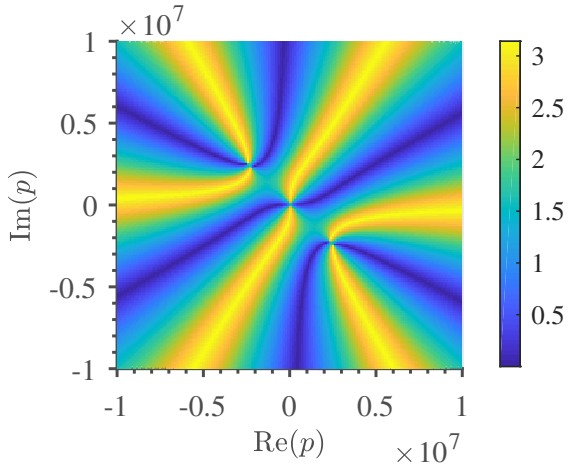

Fig. 6.1 Partial wave eigenvalue determinant of the combined fluid characteristic at 3000ms^{-1} at $\omega = 10^0$ for water. Colour map denotes complex phase, solutions are points that appear to have all phase values.

The partial waves are initially complex above bulk wave velocities, like viscoelastic materials the solutions may be rotated onto the real axis using an imaginary wavenumber. This may be seen as pumping energy into the fluid but unlike the viscoelastic materials, this rotation will not align all the partial solutions with the real axis.The frequency dependency simplifies significantly from the viscoelastic case, due to the lack of elastic stiffness to interact with the viscous behaviour. Up to values of 10^{10} the roots are linearly dependent with frequency on a log-log scale, illustrated in Figure 6.2, this linear relationship is independent of input velocity (ratio of input k and ω).

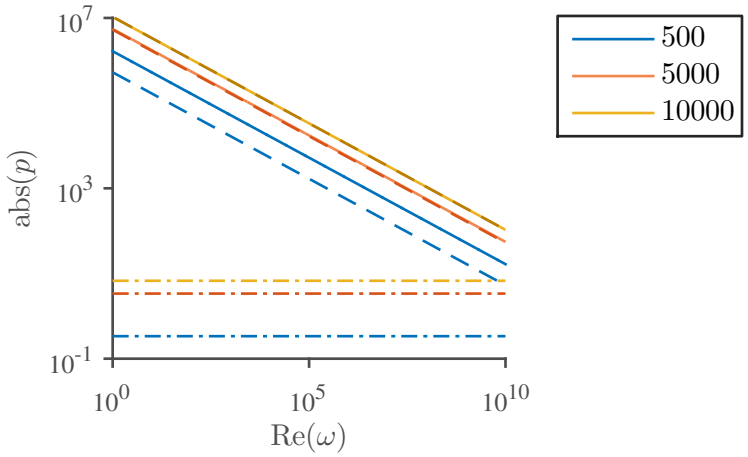

Fig. 6.2 The change in partial wave solution of water with change in frequency for different velocities on a log-log scale. Solid and dashed lines correspond to the shear partial solutions and dash-dot lines correspond to longitudinal partial solutions.

The change in the longitudinal partial wave solutions within the frequency range is negligible, in Figure 6.2 at values $\delta p < 10^{-5}$. For a fixed velocity the shear solutions can be approximated for any frequency using the gradient of the log-log scale in the simple relationship,

$$p(\omega) = p_0 \omega^m. \tag{6.23}$$

The value of m can be easily calculated, for the case shown in Figure 6.2, $m \approx -0.5$ for all shear partials for both the real and imaginary p-values. The change of the highest shear partial solution with change in imaginary frequency is presented in Figure 6.3. The bulk partial solutions remain constant and the lower shear follows the same trend as the highest shear.

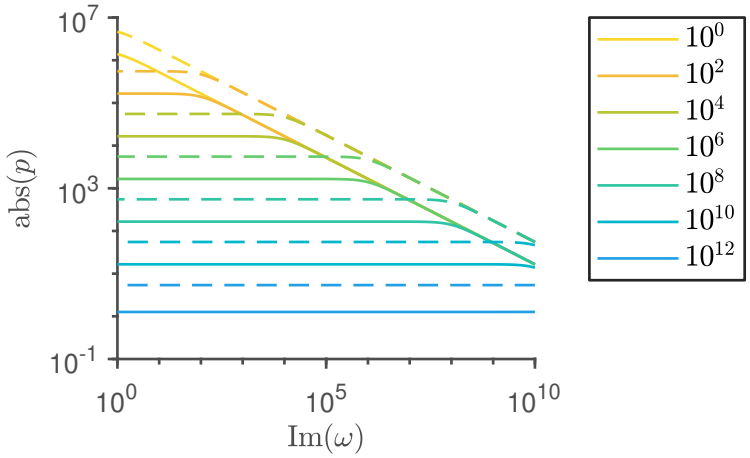

Fig. 6.3 The change in the highest shear partial wave solution of water with change in imaginary frequency at fixed real frequency values on a log-log scale. Solid lines are at a velocity of 500ms^{-1} and dotted at 5000ms^{-1}.

For values below the fixed imaginary frequency the partial solutions remain constant, beyond this point they have the same linear change on the log-log scale as the real frequency. Changes in velocity will only alter the starting values of the partials and does not effect the frequency dependence, the roots may be approximated from a starting value. The point Re(ω) = Im(ω) is the change from constant partial wave solution to the constant gradient on the log-log scale. This point can be used as the starting value p_0 for approximating the solution at any complex frequency. The change in solution with the changing frequency with equating Re(ω) and Im(ω) parts is the same as Figure 6.3. Varying Re(ω) with differing fixed Im(ω) values will result in a relationship similar to that shown in as Figure 6.3. But this approximation will track each of these parts individually starting with Re(ω).

The approximate tracking of the partial wave solution with changes imaginary frequency is shown in Figure 6.4, real frequency fixed at 10^4.

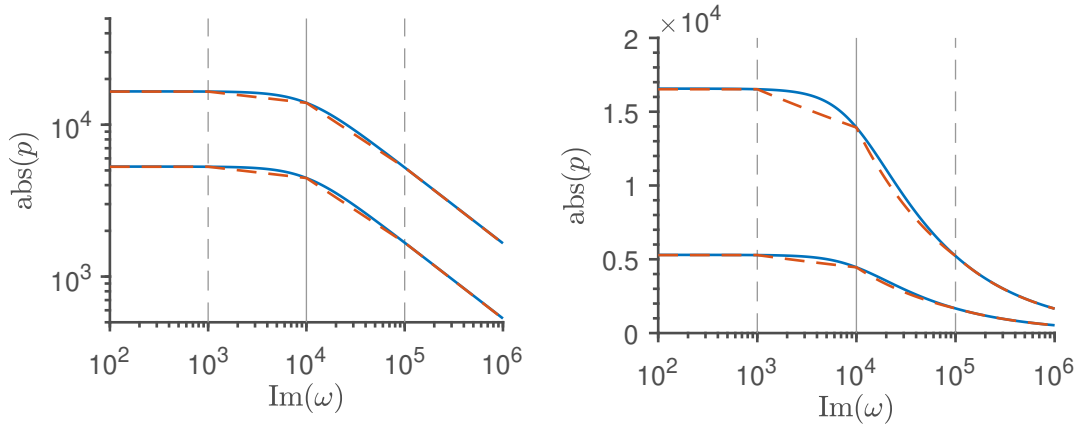

(a) Log-log

(b) Lin-log

Fig. 6.4 The tracking of the positive shear partial wave solutions by using sloped elements at 500ms^{-1} and Re(ω) = 10^4. Solid lines are computed using phase tracking and dashed lines using sloped elements.

The curved section has an estimated range of 10^3 to 10^5, within the dashed boundary lines in Figure 6.4, an order of magnitude on each side of p_0. In this case, for illustration purposes, the curved section has been discretised into two elements, the gradients for each element only needs be calculated once for all possible partial wave solutions. These gradient inputs are different for the real and imaginary parts of the partial waves, each must be calculated seperately. Note negative Im(ω) values start Re(ω) search from Re(ω) = -Im(ω), reversing the gradients between Im(p) and Re(p) parts for the Im(ω) search.

The change in partial solutions with Re(ω) and Im(ω) are for frequency ranges up to 10^{10}, for relevant velocity ranges. Beyond this point the frequency dependency no longer follows

these trends, but also does not vary by large orders of magnitude with changes in frequency. In summary this approximation of the partial change, has been developed to track the fluid partials over large changes in complex frequency. At high frequencies the rapid change in fluid partial waves no longer occurs, allowing the use of 2-dimensional gradient tracking methods.

6.2 Characterisation of Fluid Loss

The case of fluid loaded anisotropic layered half-space will be investigated using the linear fluid model developed in the previous section. In a majority of these cases the layer thickness is set to a micrometre, with the other cases investigating the change in thickness. Within this frequency range, the effect that the change in fluid partial solutions has on the mutlilayered solution is small compared to the effect of anisotropy. Within this range the frequency dependences may be ignored or tracked using 2-dimensional gradient methods.

6.2.1 Isotropic waveforms

In Chapter 2 the existence of Rayleigh and Love waves was reviewed, these waves exist in elastic isotropic materials. In an half-space, coupling between the mechanical Rayleigh mode and fluid medium, propagates the so called Scholte wave [4–6]. Similar to the Stonely wave at the solid-solid interface, this waveform decays in both the mechanical half-space and fluid medium away from the interface. The fluid medium is unable to hold a propagating waveform due to the lack of stiffness, displacements have frequency dependent decay due to the viscosity tensor. Displacements that contribute to direct stresses couple to generate pressure waves, in fluid loaded Rayleigh wave devices, the out-of-plane displacement leads to attenuation [7, 8].

As a starting point, the fluid loaded layered isotropic problem is discussed, the Love waves do not leak energy out of the system due to the in-plane shear polarisation. Introducing an elastic layer between the fluid and elastic half-spaces yields the same decaying structure; this is dependent on the relative bulk velocities of the materials. Provided that the bulk velocity of the layer is lower than the mechanical half-space, then propagating modes may exist in the layer and decay in both half-spaces. This structure is presented in the Figures 6.5, which shows 1-dimensional displacements of copper [1] on silicon [9] using A-factor scaled to isotropic.

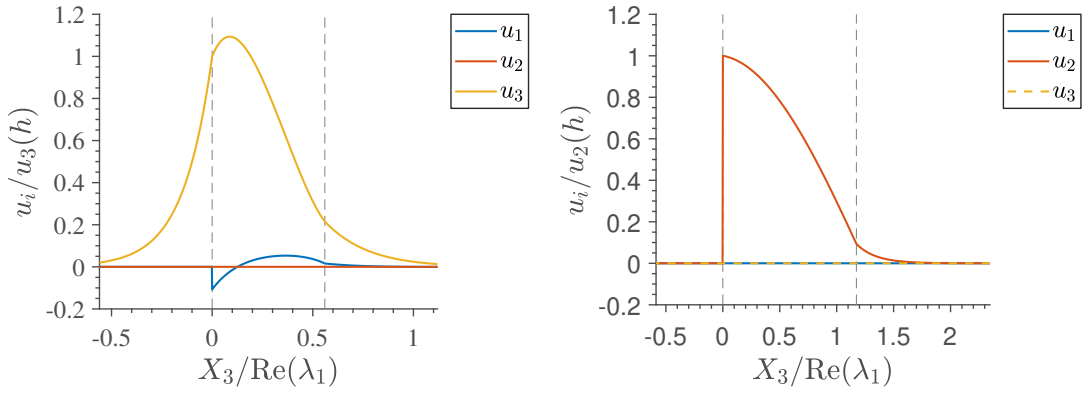

(a) Rayleigh type (b) Love type

Fig. 6.5 The first Rayleigh mode (a) and Love mode (b) of fluid loaded copper layer on silicon substrate, both materials scaled to isotropic using A-factor. Normalised to the maximum surface displacement $u_i(h)$, grey dotted lines denote interfaces, the line at zero is the interface between fluid and elastic.

The attenuation of the Rayleigh mode is much greater than the Love mode due to the structure of the stress constitution of the fluid. In the fluid, the spatial decay of the out-of-plane displacement u_3 is siginificantly larger than that of the shear displacements. This result is expected, due to the structure of the fluid stress constitution which couples the direct strains to the pressure wave. In application this may be physically interpreted as the generation of pressure waves due to out-of-plane displacements.

The case shown in Figure 6.5 is when the thickness is set to unity, presented in Figure 6.6 is the change in ratio of imaginary to real parts of the wavenumber for the first Rayleigh and Love modes.

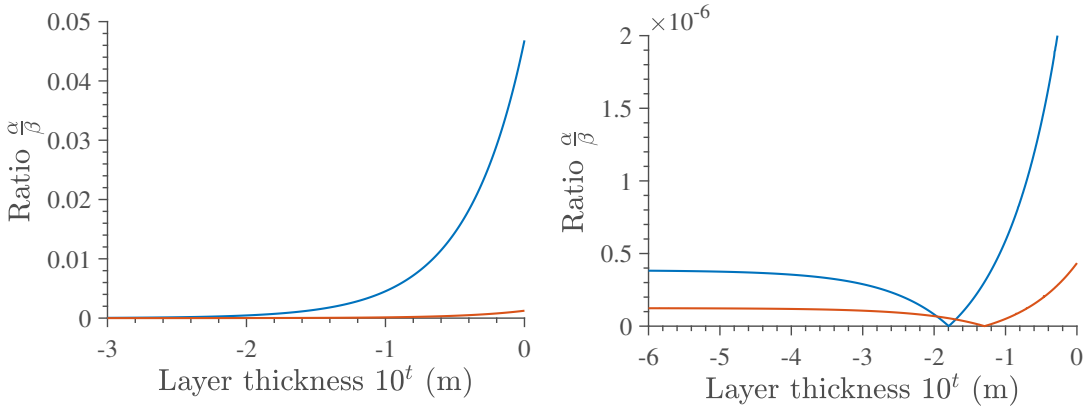

(a) Rayleigh type (b) Love type

Fig. 6.6 Presented is the change in the ratio of imaginary to real parts of the wavenumber with change in the layer thickness. In (a) the first two Rayleigh modes and in (b) the first two Love modes, the blue lines are the first mode for each.

For the Love modes of this particular case, the change in layer thickness does not have any siginificant effect on the attenuation when compared to the Rayleigh case. As the layer thickness approaches a micrometre, the attenuation of the Rayleigh wave approaches that of the Love wave solution. In this range, the attenuation of the distinctive isotropic wave types is low, for this particular layered case, in the next section particular anisotropic cases will be explored.

In comparison with analytic models from the literature [10], there is a difference of approximately 70ms^{-1} at 1MHz for a shear viscosity of 10Pa. The attenuation is within a similar magnitude range as the analytic mode at approximately 1. Note for this comparison a 3-dimensional modification of the water parameters using Stokes assumption was made. Along with this a bulk modulus for copper and steel was included to allow for the modelling of 3-dimensional waves.

6.2.2 Compatible symmetries of quartz and silicon

In Chapter 2 the topic of compatibility between different layered anisotropic crystals was introduced using bulk wave solutions. In Chapter 4, the compatibility discussion was expanded in the context of directional dependent LSAW propagation. In this section compatibility once again becomes relevant, in this case, the nature and variation of the generalised SAW modes. The interaction of differing symmetries will reduce the overall symmetry of the combination. The structure of the generalised modes in these combinations will differ from the isotropic waveforms, along with the attenuation, due to fluid coupling. These changes will be different for the dominant quasi-Rayleigh and quasi-shear horizontal modes, provided that a clear distinction between these displacement forms exist.

Before considering the fluid loading problem, the mechanical solutions for quartz on (100) and (111) cuts of silicon, in Miller notation, are investigated. These combinations are rare but are possible, see Section 1.2.2, typically an isotropic waveguide is used at the surface. Single crystals used in biosensor design are typically all anisotropic, so these types of combinations may not be avoidable. Limiting microsystems design to isotropic materials would also exclude many anisotropic behaviours, such as those explored in Chapter 4. Presented in Figure 6.7 are the wavenumber surfaces of first two generalised SAW modes with change in propagation angle. All the results in this and the next section are computed in the non-leaky range at at 4000ms^{-1}.

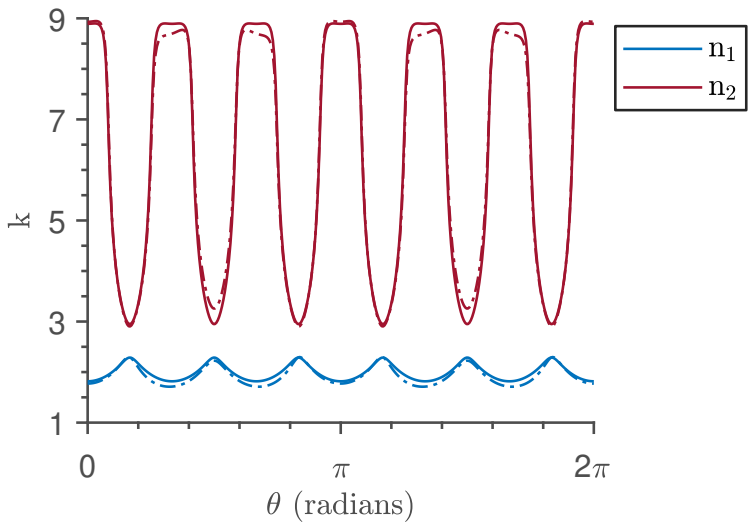

Fig. 6.7 Mechanical wavenumber solutions with change in the propagation angle for the first two generalised SAW modes of quartz layered on silicon (111) (Solid) and silicon (100) at 4000ms^{-1}.

For the modes of (111) substrate, a clear 6-fold symmetry is observed, expected due to the alignment of the symmetries of quartz and silicon. In the case of (100) substrate the 6-fold symmetry of the modes is broken, the 6-fold behaviour can be observed but an overall 2-fold symmetry is seen. This is predicted by lowest common symmetry of the bulk solutions of Z-cut quartz and (100) silicon, which is 2-fold symmetry. To predict the possible attenuation that the modes in these combinations will suffer under fluid loading, will require inspecting the out-of-plane displacement component. Using this data the average u_3 displacements at the surface, thickness of h, of quartz is computed over a wavelength (λ_1) area, presented in Figure 6.8.

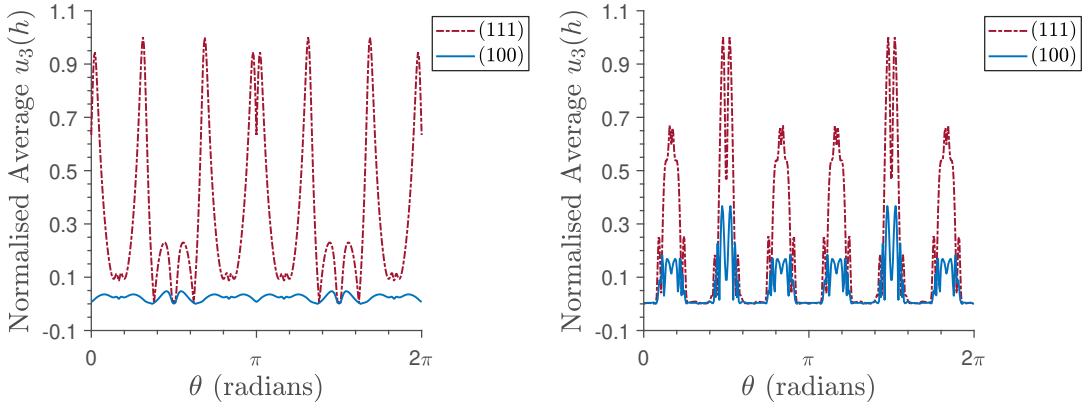

(a) 1st mode (b) 2nd mode

Fig. 6.8 Presented is the u_3 displacement for (a) first and (b) second generalised SAW modes of quartz layered on silicon (111) and silicon (100) with change in the propagation angle. These displacements have been normalised to maximum silicon (100) and averaged over a wavelength (λ_1) area at the surface of the quartz layer.

Even though the wavenumber surfaces are reasonably consistent in shape, the difference in value of the u_3 displacement can be clearly seen. The shape of the average u_3 closely matches between the two substrate cuts, though this is more distinct in the silicon (100) case. From these results it is expected that the (100) substrate should have a significantly large attenuation and that for both the attenuation should not be uniform with changes in propagation direction.

For completeness the relative displacement components are presented for the first mode of both cases in Figure 6.9.

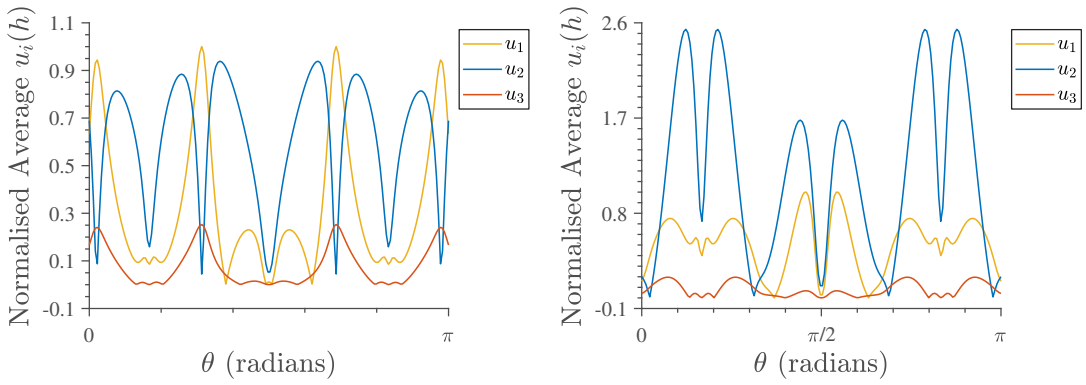

(a) Silicon (100)

(b) Silicon (100)

Fig. 6.9 Presented are the relative displacements u_i for the first generalised SAW mode of quartz layered on (a) silicon (111) and (b) silicon (100) with change in the propagation angle. These displacements have been normalised to maximum of u_3 and averaged over a wavelength (λ_1) area at the surface of the quartz layer.

6.2.3 Fluid loaded quartz layered on silicon

For the cases considered in the previous section a fluid will now be loaded, with the addition of an isotropic silicon case using the A-factor from Section 2.4.2. For all three cases at a high frequency, distinct lower and higher attenuated branches of solutions exist. Due to the frequency dependency of the fluid coupling, the attenuation varies with changes in layer thickness, see Figure 6.10. At large thicknesses the attenuation between the two generalised modes becomes comparable. These thicknesses are far larger than normal application range and the reliable range of this fluid formulation. Within the biosensor application range, the attenuation remains constant for both the maximum and minimum peaks of the multilayered solutions. For all branches of solution, the anisotropic case has a much greater value for the attenuation when compared to the isotropic cases previously.

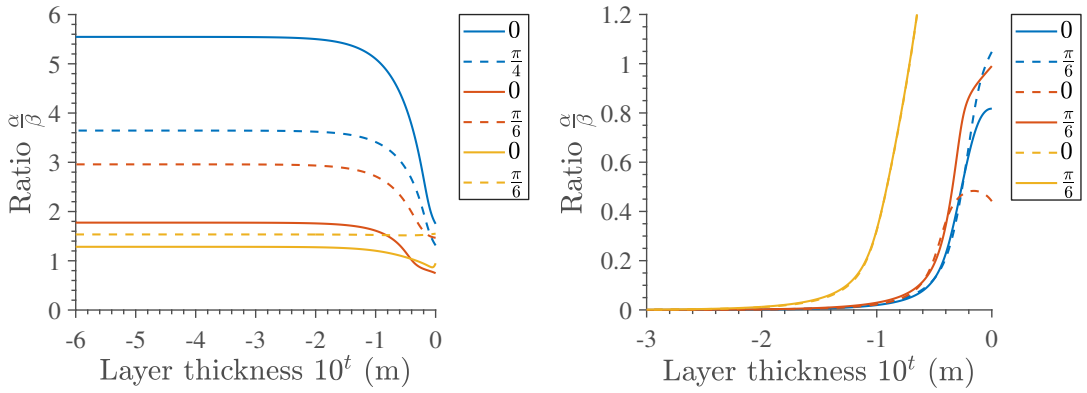

(a) High attenuation (b) Low attenuation

Fig. 6.10 Presented is the change in the ratio of imaginary to real parts of the wavenumber with change in the quartz layer thickness on silicon. In (a) are solutions from the high attenuated branches and in (b) are solutions from the low attenuated branches, blue line for (100), red for (111) and yellow for (Iso) by scaled A-factor.

The variation of the solution with propagation direction, due to the anisotropy, is presented for the high attenuated branches of all substrates in Figure 6.11. Figure 6.12 shows the same results but using the magnitude and phase representation of the complex wavenumber. For silicon (100) in this high attenuated branch the cubic structure of this cut can be clearly seen in the real part of the wavenumber. In the magnitude plot, this cubic structure is less prominent, though both clearly show the 2-fold cyclic structure that is expect due to the alignment of 4-fold and quasi-6-fold symmetries.

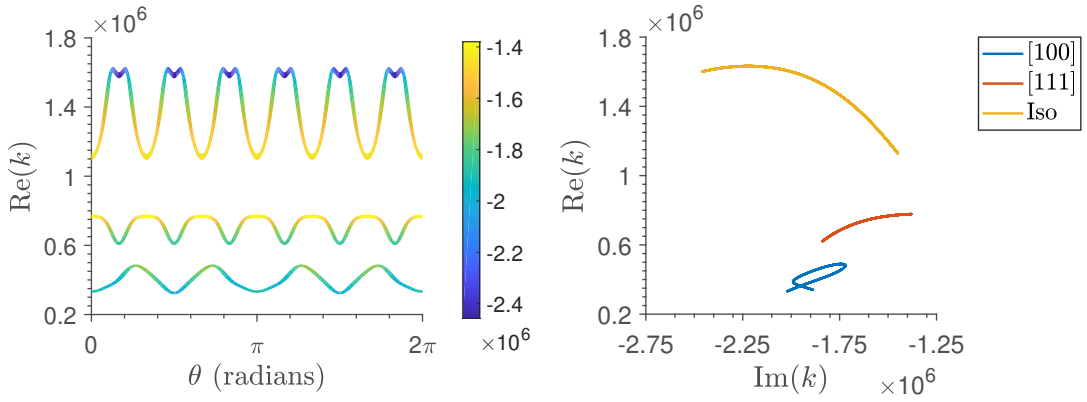

(a) Angle (b) Complex plane

Fig. 6.11 Presented is the variation of the 1st SAW mode from the high attenuated with branch change in the propagation angle. In (a) the change in real part of the wavenumber with the propagation angle, colour map denotes imaginary part, and in (b) the projection of this in the real and imaginary axis of the wavenumber.

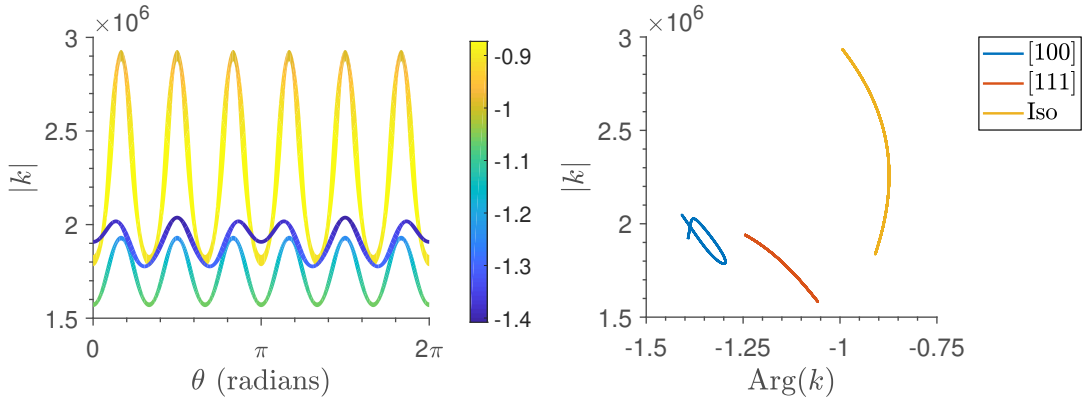

(a) Angle (b) Complex plane

Fig. 6.12 Presented is the variation of the 1st SAW mode from the high attenuated with branch change in the propagation angle. In (a) the change in magnitude of the wavenumber with the propagation angle, colour map denotes complex phase, and in (b) the projection of this in the complex magnitude and phase axis of the wavenumber.

For both silicon (111) and (Iso), a clear 6-fold cyclic symmetry exists in both the real and magnitude representations of these modes. The variation is due to the curvature of the solutions into the complex plane, and is uniform for all six peaks, unlike the viscoelastic cases in Section 5.2.2. For higher modes, for all the cases, the structure approaches the 6-fold cyclic symmetry structure of the isotropic silicon case, due to the lower contribution of the substrate for higher modes.

The variation of the low attenuated modes with propagation angle is presented in Figure 6.13, for all silicon cases.

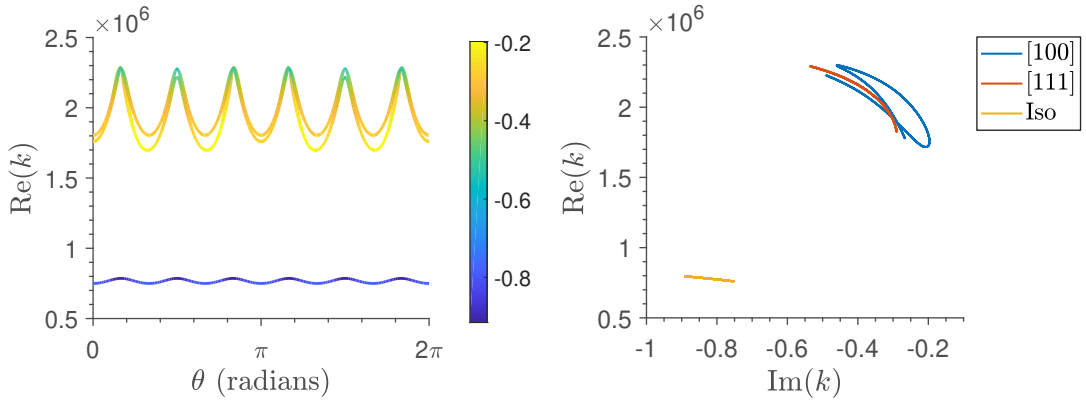

(a) Angle (b) Complex plane

Fig. 6.13 Presented is the variation of 1st SAW mode from the low attenuated branch with change in the propagation angle. In (a) the change in real part of the wavenumber with the propagation angle, colour map denotes imaginary part, and in (b) the projection of this in the real and imaginary axis of the wavenumber.

For all cases, the structure in the complex plane is similar to the high attenuated solutions. The complex curvature in the (111) and (Iso) cases does not effect of the structure of the real wavenumber variation as much as the high attenuated branch. In the case of (100) the structure is 2-fold cyclic symmetry, but this is a small deformation from the quasi-6-fold symmetry of the quartz.

Inspecting the silicon (100) case in closer detail, the two generalised multilayered modes have a degree of attenuation, both greater than the pure isotropic case. The stress distribution in the fluid for both modes is presented in Figure 6.14.

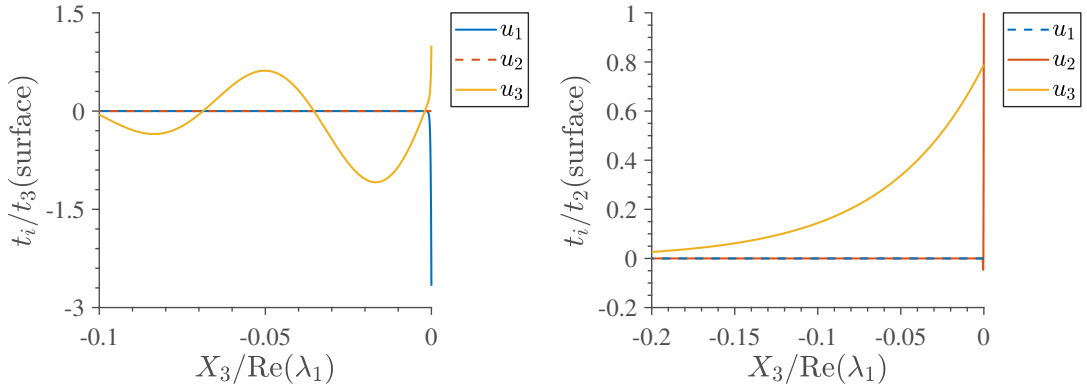

(a) High attenuation

(b) Low attenuation

Fig. 6.14 The 1-dimensional traction distribution with fluid depth from the surface. Presented for the first (a) high attenuated mode and (b) low attenuated mode of fluid loaded quartz layered on silicon (100) substrate.

Unlike the isotropic case, both types of mode now have an out-of-plane displacement which couples to the fluid, the shears rapidly decay. Due to the large energy loss in the high attenuated solution, the wave vector is tilted which leads to propagation into the bulk of the fluid. The displacements of this propagating wave will rapidly decay, due to the lack of an elastic tensor, and generate pressure waves due to the coupling in (6.10). Inspecting the 2-dimensional t_3 surfaces, presented in Figure 6.15, the difference in wave tilting between the high and low attenuated modes can be clearly seen.

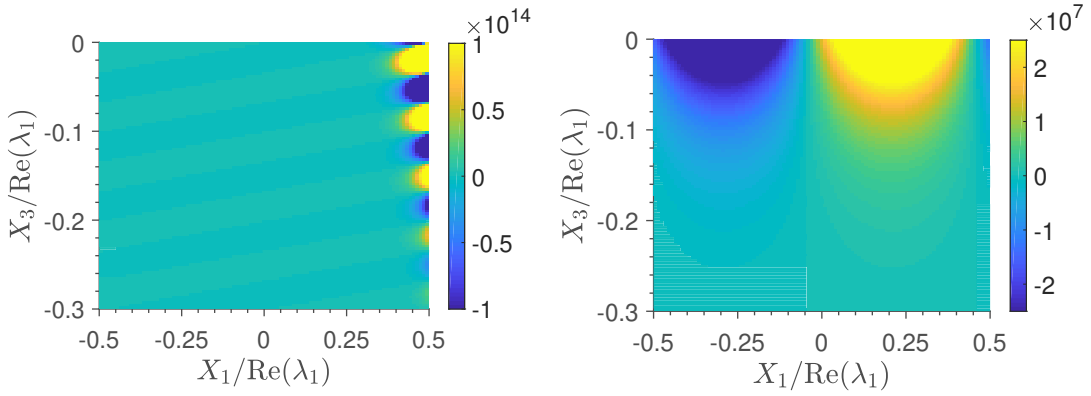

(a) High attenuation

(b) Low attenuation

Fig. 6.15 The 2-dimensional out-of-plane traction distribution with fluid depth from the surface. Presented for the first (a) high attenuated mode and (b) low attenuated mode of fluid loaded quartz layered on silicon (100) substrate. Colour map denotes out-of-plane u_3 displacement.

6.3 Conclusion

The 3-dimensional fluid partial wave eigenvalue problem has been developed using the viscosity tensor allowing for the coupling of both direct and shear stresses. The problem of fluid loading on a layered medium is presented for the case of water loading on isotropic and anisotropic layered medium. For the isotropic case, the Rayleigh wave attenuation is shown to be significantly larger than the Love wave attenuation, at high frequencies these both approach a negligible value.

The anisotropic case is focused on the compatibility of layer to substrate symmetries, and the impact this has on energy loss by fluid coupling. For all the cases presented, the attenuation increased with decreased layer thickness, in contrast to the isotropic layer behaviours. A set of high and low attenuated branches exist, similar to the LSAW modes. For the low attenuated case, the (Iso) silicon has the highest attenuation out of the three cases presented, but all approach zero as the layer thickness decreases. For the high attenuated mode, the incompatible quartz on silicon (100) has a significantly large attenuation, with the (Iso) case having the lowest.

For the low attenuated mode, the cyclic symmetry takes the structure of the layer material for all cases, with some minor variation for the (100) silicon case. The difference in cyclic symmetry is clearly seen in the high attenuated modes, for the (Iso) and compatible (111) cuts of silicon, the structure has a clear 6-fold cyclic symmetry. In the case of (100) cut of the silicon, the quasi-6-fold and 4-fold symmetries conflict resulting in an over 2-fold cyclic symmetry.

Chapter 7

Sources of Energy Loss and Q-factor Model

In this chapter the effect of various energy loss mechanisms, that have been explored in the previous chapters, is investigated using the Q-factor (quality). The energy loss of these devices will lead to error in the sensing mechanism, measured by the Q-factor, this must be lower than the errors of other components of the biosensor. In addition to the forms of attenuation that have already been developed, the effect of thermoelastic loss is also modelled. Unlike the previous forms which may be seen as purely mechanical, the thermal behaviour requires solving the heat equation, which will be coupled to the mechanical displacements. The comparison of the Q-factor for different forms of attenuation will be made in the simplified case of plane wave propagation in a single direction, as an analogue to a delay-line type biosensor. Along with the thermoelastic formulation, the piezoelectric coupling is also modelled using a similar approach. The piezoelectric effect is important for the excitation of surface acoustic wave (SAW) modes for biosensor applications and the design of shaped annular transducers.

7.1 A Review of Sources of Loss

The numerical models that have been developed so far can be used to predict the attenuation for various physical mechanisms. These include acoustic bulk leaking in Chapter 4, viscoelastic loss in Chapter 5 and fluid leakage in Chapter 6. In addition, the method developed for viscoelastic loss may be used to model the collective intrinsic losses within elastic materials. Intrinsic loss covers energy loss due to impurites and dislocations within a material which forms during the manufacturing process [1, 2]. If the material is a polycrystal then grain boundaries also exist,

which can cause energy loss due to scattering [3]. The propagating waveform is a physical motion of energy transfer between kinetic and potential, in reality this transfer of energy is not completely conservative due to this material scattering. The degree of energy loss is dependent on the material type and the quality of the manufacturing process.

In cases of non-fluid loading, outside of a vacuum, the acoustic loss in air [4] may be approximated using the methods developed for fluid loss. Another form of loss that can occur in mechanical sensors is surface loss, which is the loss due to imperfections and absorbates on the surface of the device [1, 4]. This may be viewed as the mass loading of a substance on the surface of the device, which has a lower stiffness than the materials that make up the sensor. Although both of these can be modelled, the loss due to these two effects can typically be mitigated by using vacuum packaging techniques. The degree of effect that the surface loss has is dependent on the class of clean room that a device would be produced in, before vacuum packing.

The SAW boundary conditions that have been used up to this point assume that the substrate material is an isolated half infinite space. In reality the SAW device is finite, and therefore energy may be acoustically leaked out of the system through support loss [1, 4, 5]. Resonators are designed to be free floating devices with supports, if the resonance frequency of the device matches that of the supports, then energy make be lost through flexural mode excitation. In addition to this, SAW resonators use reflectors to generate the stand mode, and mitgate energy leakage out of the system [6]. In the real world these reflectors will still leak energy out of the system through the supports. Therefore, these two types of loss mechanisms are inherently linked [7, 8], typically this is a design problem and therefore will be ignored for this investigation. The number and design of the reflector can also depend on the Q-factor of the tailored SAW mode, to contain other forms of energy loss.

Thermoelastic damping is a form of loss induced by the coupling between the mechanical and thermal properties. The propagating waveform in a thermoelastic medium create local temperature gradients, due to the coupling with strain. Material relaxation occurs due to the irreversible heat flow through the material in the form of an oscillating motion, due to the wave generated gradients. The traditional model for thermoelastic damping in micro-mechanical resonators is the Zener's approximation [9, 10], based on beam geometry. The approach taken in this work is to model this form of loss, covered in Section 7.2.

Piezoelectric coupling is the mechanism used to generate and detect SAW modes for mechanical biosensors. This subject has been mentioned throughout this work, but now in this chapter the problem is modelled using the standard tools developed in Chapter 3. With the coupling of

electric fields comes the introduction of several forms of energy loss, either through a complex piezoelectric or dielectric constant, see [11].

Alternatively, the piezoelectric coupling may alter the existence problem for the pure mechanical waves, requiring a complex wavenumber to exist. The existence of SAWs on anisotropic piezoelectric half-spaces can not be guaranteed for the free surface conditions [12], unlike in the elastic case. Although for the short circuit surface condition a solution can typically be guaranteed; multilayered anisotropic piezoelectric solutions have been calulated for particular biosensor applications [13]. For both possible forms of piezoelectric loss, a solution in the leaky form of Chapter 4 would be capable of capturing the attenuation.

7.2 Thermoelastic Formulation

The formulation, up to this point, has been 3-dimensional to allow the capture of anisotropic behaviour of different symmetry classes of crystals. A 3-dimensional approach is also used for the modelling of the thermoelastic coupling, to allow the modelling of anisotropic thermoelastic effects [14]. In addition, this will make all the models for Q-factor consistent and allow the modelling through the 3-dimensional eigenvalue approach.

7.2.1 3-Dimensional wave model

The coupled piezoelectric and thermoelastic constitutive and motion equations are formulised in Appendix B, using [15, 16]. Only the thermoelastic equations are used in this section, using the coupled wave and heat equations as the starting point,

$$C^{ijkl}\frac{\partial^2 u_l}{\partial x^j \partial x^k} - \lambda^{ij}\frac{\partial \delta T}{\partial x^j} = \rho\frac{\partial^2 u^i}{\partial t^2}, \tag{7.1}$$

$$K^{ij}\frac{\partial^2 \delta T}{\partial x^i \partial x^j} = T_0\lambda^{ij}\frac{\partial^2 u_j}{\partial t \partial x^i} + \rho C\frac{\partial \delta T}{\partial t}. \tag{7.2}$$

The extra terms, in addition to those introduced in Section 2.1, are thermal expansion λ_{ij}, thermal conductivity K_{ij}, small temperature change δT and reference temperature T_0 for the material. The constant temperature superscript has been dropped for the stiffness $C^{(T)}_{ijkl}$, along with the constant strain superscript for specific heat capacity $C^{(\varepsilon)}$, for convenience. Assuming a solution for the mechanical and thermal displacements, u_i and δT respectively, in the same form as (4.1). This solution is substituted in (7.1) and (7.2) which results in the coupled eigenvalue problem,

$$(\mathrm{i}\beta - \alpha)^2 C^{ijkl}(m_j + pn_j)(m_k + pn_k)A_l + (\mathrm{i}\beta - \alpha)\lambda^{ij}(m_j + pn_j)A_4 = \mathrm{i}^2 p\omega^2 A^i, \tag{7.3}$$

$$(\mathrm{i}\beta - \alpha)^2 K^{ij}(m_i + pn_i)(m_j + pn_j)A_4 = \mathrm{i}\omega\rho C A_4 - \mathrm{i}\omega(\mathrm{i}\beta - \alpha)T_0\lambda^{ij}(m_i + pn_i)A_j. \tag{7.4}$$

Where A_4 is now the amplitude of the thermal displacement. These can be rearranged into the following form in frequency ω and phase velocity v,

$$[\Gamma^{il} - \rho v^2 \delta^{il}]A_l + \frac{v}{\mathrm{i}\omega}\Lambda^i A_4 = 0, \tag{7.5}$$

$$[K - \frac{\rho v^2 C}{\mathrm{i}\omega}]A_4 + vT_0\Lambda^j A_j = 0. \tag{7.6}$$

The summation terms, along with the propagation tensor Γ^{il}, have been redefined as follows,

$$K = K^{ij}(m_i + pn_i)(m_j + pn_j), \tag{7.7}$$

$$\Lambda^j = \lambda^{ij}(m_i + pn_i), \tag{7.8}$$

$$\Lambda^i = \lambda^{ij}(m_j + pn_j), \tag{7.9}$$

7.2.2 Separated Eigenvalue problem

The determinant of the combined system of equations (7.5) and (7.6) is a function of the partials p with eight solutions. Six of these solutions belong to the mechanical displacements while the other two are introduced due to the thermal coupling, see Figure 7.1.

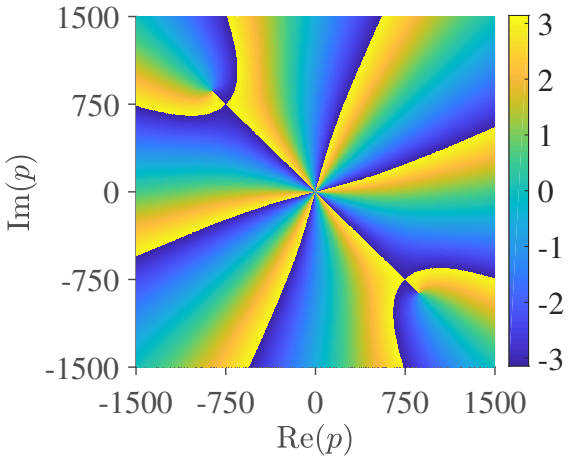

Fig. 7.1 Partial wave eigenvalue determinant of the combined set of equations (7.5) and (7.6), below bulk wave velocities at a frequency of 1MHz. Colour map denotes complex phase, solutions are points that appear to have all phase values.

In both the thermoelastic and piezoelectric cases, the mechanical, electrical, and thermal material input parameters are of several orders of magnitude, different from each other. The effect can be seen in the thermoelastic case, in Figure 7.1, the two thermal partial solutions are several orders of magnitude greater than the six mechanical solutions. This difference is dependent on frequency, with similar orders around 10GHz, for much smaller frequencies the thermal partial solutions increase in value. From a numerical approach, it is desirable to seperate the thermal and mechanical partial solutions, to reduce unnecessary computations. The approach taken here is to rearrange the thermal part (7.6),

$$A_4 = \frac{vT_0\Lambda^j}{K + \frac{\rho v^2 C}{\mathrm{i}\omega}} A_j, \tag{7.10}$$

and substitute the amplitude into the mechanical part (7.5),

$$[\Gamma^{il} - \rho v^2 \delta^{il} + \frac{v^2 T_0 \Lambda^i \Lambda^q}{\mathrm{i}\omega K}\delta^l_q + \frac{\Lambda^i \Lambda^q}{\rho C}\delta^l_q]A_l = 0, \tag{7.11}$$

Equation (7.11) may be numerically solved for the mechanical partial solutions of Figure 7.1, using techniques developed in Chapter 3. The mechanical amplitudes in (7.11) can be written as a function of the input partial $A_i = f(p)$, in this work this is achieved using a computer coded function. So now the thermal part of the problem can be computed using (7.6) with the mechanical amplitudes, the seperated partial determinant are presented in Figure 7.2.

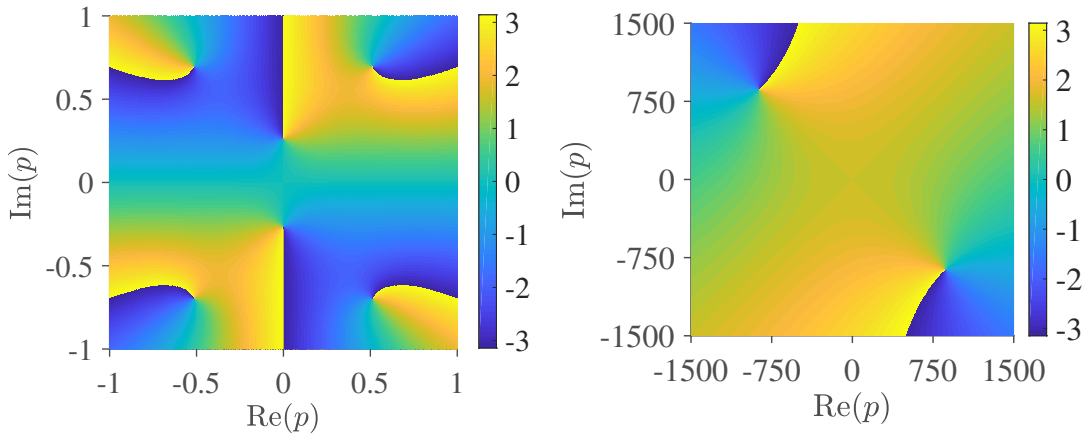

(a) Mechanical

(b) Thermal

Fig. 7.2 Partial wave eigenvalue determinants of (a) mechanical part (6.11) and (b) thermal part (6.6) with mechanical amplitudes as a function of p. Both are below bulk wave velocities at a frequency of 1MHz. Colour map denotes complex phase, solutions are points that appear to have all phase values.

7.2.3 Thermoelastic boundary conditions

The mechanical boundary conditions outlined in Section 3.2.3 remain the same, the only change is the extra terms in the tractions due to the coupling,

$$t^i = C^{ijkl}\frac{\partial u_l}{\partial x^k}n_j - \lambda^{ij}\delta T n_j. \tag{7.12}$$

In addition, thermal boundary conditions are required at the interface between materials and at the free surface. For the interface [17], the continuity of temperature and the component of temperature gradient, normal to the surface,

$$\delta T = \delta T', \tag{7.13}$$

$$\frac{\partial \delta T}{\partial x_j}n_j = \frac{\partial \delta T'}{\partial x_j}n_j. \tag{7.14}$$

For the free surface condition, a common approach seen through the literature [18, 19] is to use both the temperature and temperature gradient expressed in the form,

$$\frac{\partial \delta T}{\partial x_j}n_j + g\delta T = 0. \tag{7.15}$$

As $g \to 0$ the condition becomes thermally insulated and $g \to \infty$ the surface becomes isothermal.

7.2.4 Uncoupled boundary conditions

For thermoelastic problems it is often assumed that the mechanical stress fields have a negligible impact on the thermal gradients. With this assumption the coupling is only considered in the mechanical part and the thermal contribution is treated as a body force in the wave equation [20]. Solving the mechanical eigenvalue problem (7.11) yields the coupled mechanical partial wave roots as a function of the frequency and velocity. Solving the coupled part of the mechanical boundary conditions (7.12) will produce solutions, but the thermal part of the problem will not be constrained.

This uncoupled approach gives an approximation of thermoelastic loss by neglecting thermal interactions, but is computational cost efficient. Another benefit of this approach is the insignificant frequency dependency in the mechanical partial solutions, from the thermal coupling. The partial wave solutions of the thermal part of the eigenvalue problem are highly frequency dependence. This dependency does not significantly interact with mechanical partials, but does couple into the mechanical boundary conditions. Presented in Figure 7.3 is a comparison between the uncoupled curves with data points of the fully coupled problem.

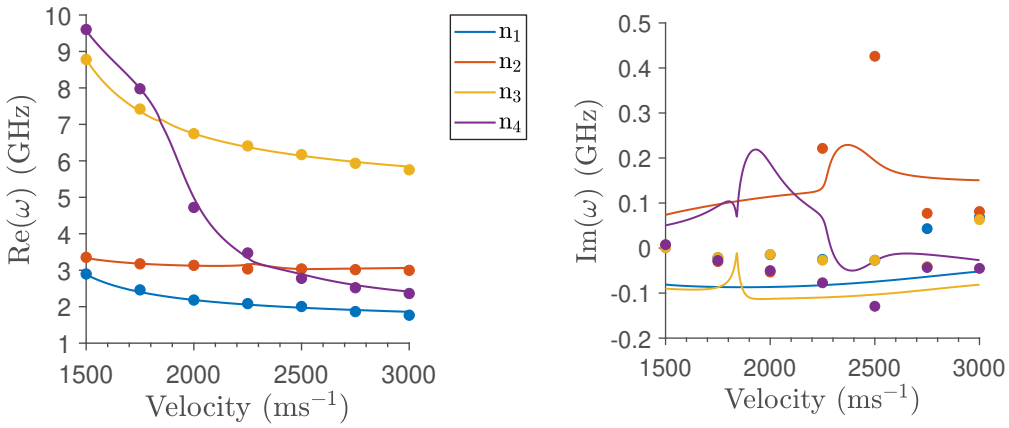

(a) Re(ω)

(b) Im(ω)

Fig. 7.3 Comparison between the coupled (points) and uncoupled (curves) solutions for the thermoelastic problem, for the case of SU-8 on Z-cut quartz. In (a) the real frequency data and (b) the imaginary frequency data for the first four SAW modes.

For Re(ω) the coupled and uncoupled agree with each other, a key point to note is that the curves also resemble the mechanical only problem. The thermal coupling in this case is not having a significant effect on the mechanical displacements, this is shown by the difference in magnitude between the real and imaginary parts of the solutions. For Im(ω) the uncoupled problem, for most of the curve, overestimates the impact of the thermoelastic coupling. There

is some disparity between the shapes of these curves, the uncoupled formulation predicts the presence of a peak at around 2400ms^{-1} for modes n_2 and n_3, but underestimates the value. Due to the overestimation of the loss and the dominance of the real part over imaginary, this is a suitable approximation of the Q-factor for this case. The uncoupled problem should not be relied on for information on presence of lossy spikes in the frequency.

7.3 Piezoelectric Formulation

Mechanical waveforms are excited using the applied electric fields in piezoelectric crystals, in which the mechanical and electric displacements are coupled. In addition the piezoelectric and dielectric tensors also differ between the crystal symmetry classes, similar to the stiffness coefficients. The piezoelectric coupling can alter the symmetry structure of a crystal and therefore must be computed when considering cases of cylindrical sensor design.

7.3.1 Coupled equations and eigenvalue problem

The approach to modelling the piezoelectric coupling is almost idenitical to the thermal model in the previous section. Starting with the equations in Appendix B, now only the piezoelectric part of the formulation is used alongside the mechanical part. The resulting equations take the form,

$$C^{ijkl}\frac{\partial^2 u_l}{\partial x^j \partial x^k} + d^{kij}\frac{\partial^2 \phi}{\partial x^j \partial x^k} = \rho\frac{\partial^2 u^i}{\partial t^2}, \tag{7.16}$$

$$d^{ijk}\frac{\partial^2 u_k}{\partial x^i \partial x^j} - e^{ij}\frac{\partial^2 \phi}{\partial x^i \partial x^j} = 0. \tag{7.17}$$

The extra terms, in addition to those introduced in Section 2.1, are piezoelectric coupling tensor d_{ijk}, dielectric constants e_{ij}, electric potential ϕ. The constant electric field superscript has been dropped for the stiffness $C^{(E)}_{ijkl}$, along with the constant strain superscript for specific dielectric constants $e^{(\varepsilon)}_{ij}$, for convenience.

As with the thermoelastic formulation, the coupled eigenvalue problem can be formed,

$$\left[\Gamma^{il} - \rho v^2 \delta^{il}\right] A_l + \gamma^i A_4 = 0, \tag{7.18}$$

$$\gamma^k A_k + e A_4 = 0. \tag{7.19}$$

Where A_4 is now the amplitude of the electric potential. The summation terms, along with the propagation tensor Γ^{il}, have been redefined as follows,

$$\gamma^i = d^{kij}(m_j + pn_j)(m_k + pn_k), \tag{7.20}$$

$$\gamma^k = d^{ijk}(m_i + pn_i)(m_j + pn_j), \tag{7.21}$$

$$e = e^{ij}(m_i + pn_i)(m_j + pn_j). \tag{7.22}$$

The mechanical eigenvalue problem may be written in the following form by rearranging (7.19) and substituting into (7.18),

$$\left[\Gamma^{il} + \frac{\gamma^i \gamma^q}{e}\delta^l_q - \rho v^2 \delta^{il}\right] A_l = 0. \tag{7.23}$$

The numerical solution to these eigenvalues problems are the same as the thermoelastic problem. Unlike the thermoelastic problem, these eigenvalue problems are only dependent on the velocity, similar to the pure elastic problem. For dielectric materials, the resulting amplitudes are uncoupled due to the zero piezoelectric coupling, for these cases the mechanical and electrical parts can be solved seperately.

The mechanical boundary conditions remain the same as Section 3.2.3, except for the extra terms in the tractions,

$$t^i = C^{ijkl}\frac{\partial u_l}{\partial x^k}n_j + d^{kij}\frac{\partial \phi}{\partial x^k}n_j. \tag{7.24}$$

For the interface between two materials, the electrical boundary conditions [21] are the continuity of the electric potential and electric displacement normal to the surface,

$$\phi = \phi', \tag{7.25}$$

$$D^i n_i = D^{i'} n_i. \tag{7.26}$$

The electric displacement normal to the surface is given as,

$$D^i n_i = d^{ijk}\frac{\partial u_k}{\partial x^j}n_i - e^{ij}\frac{\partial \phi}{\partial x^j}n_i. \tag{7.27}$$

The free surface electric boundary condition used through the remainer of this chapter is the zero electric displacement, normal to the surface,

$$D^i n_i = 0. \tag{7.28}$$

7.3.2 Slowness error due to piezoelectric coupling

In Chapter 5 the annular transducer for generating plane waves in the far field was designed for the case of SAWs in a lithium niobate half-space. The method required estimating the far field contribution to the Green's function, as a reverse point excitation. The approximation given in [22] uses piezoelectric coupling to determine the strength of the coupling and to compute slowness surfaces. For the case of SU-8 layered on lithium niobate the contribution of the piezoelectric coupling to the slowness computation is assumed to be negligible. Using the coupled piezoelectric model, these claims may be checked, Figure 7.4 shows the comparison between the mechanical and piezoelectric solutions.

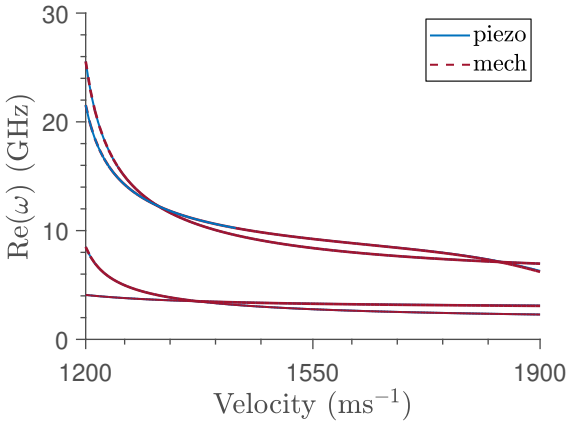

Fig. 7.4 For the case of dielectric SU-8 on piezoelectric lithium niobate, the comparison between the dispersion curves of the mechanical and piezoelectric formulation is presented. In the Z-cut of lithium niobate at a fixed angle $\theta = 0$ rad, in the non-leaky mechanical range.

For the case shown, the solutions of the piezoelectric and mechanical models are consistent, similar agreement is also seen at $\theta = \frac{\pi}{6}$. For the cases in Chapter 5, the piezoelectric coupling can be assumed to negligible, note this is due to the dominate SU-8 in the dynamics and should not be assumed for the half-space or other combinations.

7.4 Q-factor Model

For all of the loss mechanisms that have been developed so far the Q-factor may be computed for cases of interest. In this section different definitions of Q-factor for a resonator are briefly summarised along with the assumptions that will be made. For the case of SU-8 layered on an anisotropic substrate, the Q-factors will be calculated within the non-leaky velocity range and compared.

7.4.1 Q-factor modelling

Propagating waveforms in MEMS devices will suffer multiple sources of loss by leaking energy out of the system. The aim is to mitigate this energy loss which will result in the reduced performance of the device in real world situations. The degree of this energy loss will impact the design approach, and will be one of the criteria in optimising SAW propagation. Therefore, a measure of the energy loss must be developed, which will be done using the Q-factor. The Q-factor is a standard way to measure the energy loss of a resonator, this can be done using the energy loss directly [23, 24],

$$Q = 2\pi \frac{E}{\Delta E}. \tag{7.29}$$

Another approach is to inspecting the real and imaginary parts of frequency of the propagating waveforms [25, 26],

$$Q = \frac{\mathrm{Re}(\omega)}{2\mathrm{Im}(\omega)}. \tag{7.30}$$

The numerical methods developed up to this point have been developed to output the real and imaginary parts of the frequency. Mathematically these represent the conserved and non-conversed parts of the system, which is an equivalent description of energy loss. This defintion of Q-factor can be applied readily, as it comes directly from the solution to the boundary condition problem, and therefore will be used throughout this chapter.

Several numerical models have been developed that can model various mechanisms of loss. For each of these sources the Q-factors can be obtained and summated into the total Q-factor,

$$\frac{1}{Q_{total}} = \frac{1}{Q_{leaky}} + \frac{1}{Q_{visco}} + \frac{1}{Q_{fluid}} + \frac{1}{Q_{thermo}} + \frac{1}{Q_{piezo}} + ... + \frac{1}{Q_{others}}. \tag{7.31}$$

The total Q-factor can be used as the minimum seeking optimisation function to help narrow the possible high Q SAW types in general anisotropic materials. The mechanisms of loss will be modelled independently of each other, with exception for leaky loss which is inherent in all the models, but can still be shown independently in the pure mechanical case.

7.4.2 Assumptions of Q-factor model

The approach taken to modelling the Q-factor, discussed in the previous section, has several limitations due to required assumptions. The following are a list of the assumptions;

1. Material inputs remain constant.
2. The effects of each of the loss mechanisms are independent of each other.
3. The total Q-factor is the summation of the magnitude without consideration of direction.

The goal is to get an approximate effect of each of the loss mechanisms on the energy leakage of particular wave types. Even though the three approximations may be modelled, the increase in computation would be wasteful for an approximate solution. If situations arise in which certain loss mechanisms dominate, then their interaction may be modelled at a later date, for example fluid and thermal. Only the overall magnitudes are summated due to the sign of the imaginary parts of the wavenumber having physical meaning. The overall effect on the waveforms is what is of importance, not how the relative rotations of the wave vector interact.

7.4.3 Q-factor comparison for SU-8 on piezoelectric substrates

The following Q-factor investigation is presented for SU-8 layered on quartz and on lithium niobate, independently. It has been previously stated that the mechanical solutions between these cases should be similar due to the dominant layer. This may be true for the mechanical part but the difference in thermoelastic and piezoelectric coefficients may alter the Q-factors. The thickness of the waveguide for these Q-factor computations will be fixed at a micrometre, requiring operating frequencies in the GHz range. The non-attenuated mechanical dispersion curves are computed, presented in Figure 7.5 are the first four modes of SU-8 on lithium niobate and on quartz.

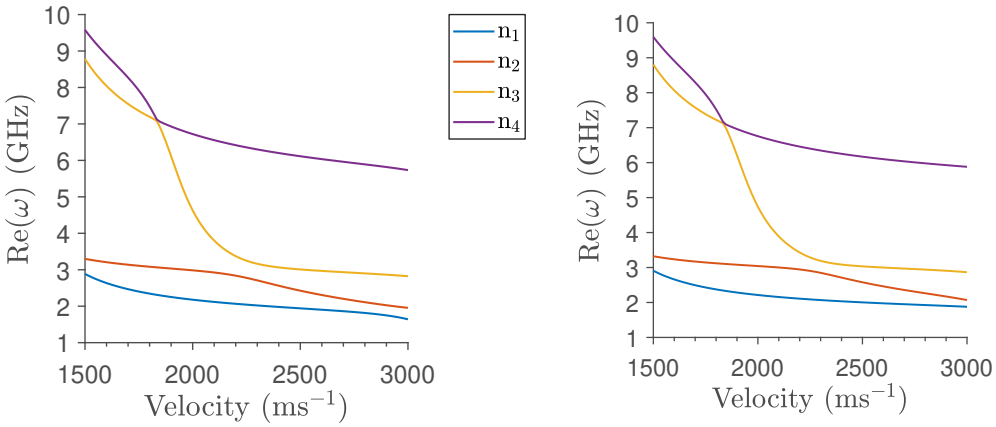

(a) Quartz (b) $LiNbO_3$

Fig. 7.5 The elastic dispersion curves for SU-8 on (a) quartz and (b) lithium niobate for the non-attenuated range. Viscoelastic parameter of SU-8 is set to zero.

The dispersion curves and Q-factors for multiple forms of attenuation have been computed independently of each other. The Q-factor is presented for viscoelastic loss with $\eta = 0.059$ in Figure 7.6, for fluid loss in Figure 7.7, for thermoelastic coupling in Figure 7.8 and piezoelectric coupling with real coefficients in Figure 7.9. The combined summation of the Q-factors is presented in Figure 7.10.

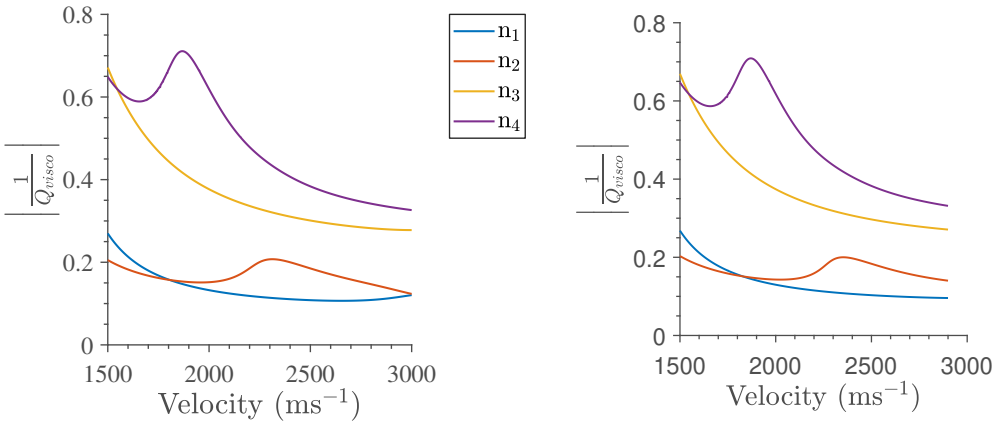

(a) Quartz (b) $LiNbO_3$

Fig. 7.6 Inverse Q-factor for viscoelastic loss in first four SAW modes of SU-8 ($\eta = 0.059$) loaded on (a) quartz and (b) lithium niobate, within the non-leaky velocity range.

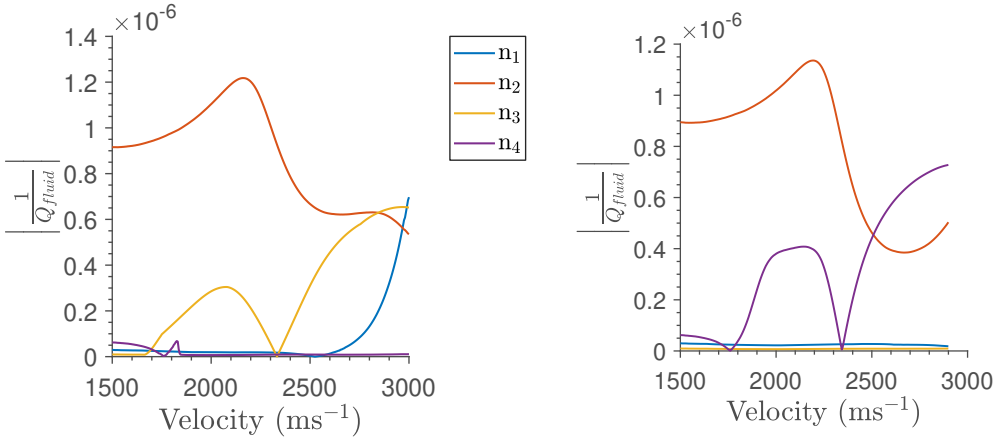

(a) Quartz (b) $LiNbO_3$

Fig. 7.7 Inverse Q-factor for a fluid half-space loading in first four SAW modes of SU-8 ($\eta = 0.0$) loaded on (a) quartz and (b) lithium niobate, within the non-leaky velocity range.

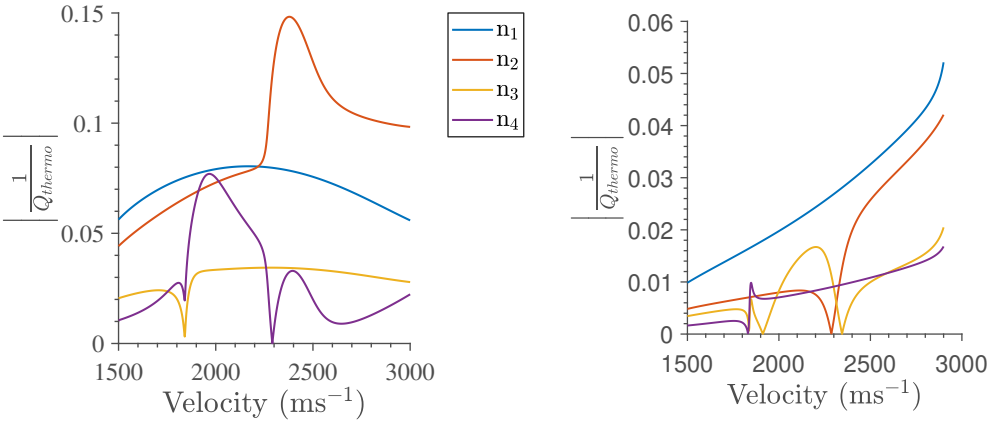

(a) Quartz (b) $LiNbO_3$

Fig. 7.8 Inverse Q-factor for loss through thermoelastic coupling in first four SAW modes of SU-8 ($\eta = 0.0$) loaded on (a) quartz and (b) lithium niobate, within the non-leaky velocity range.

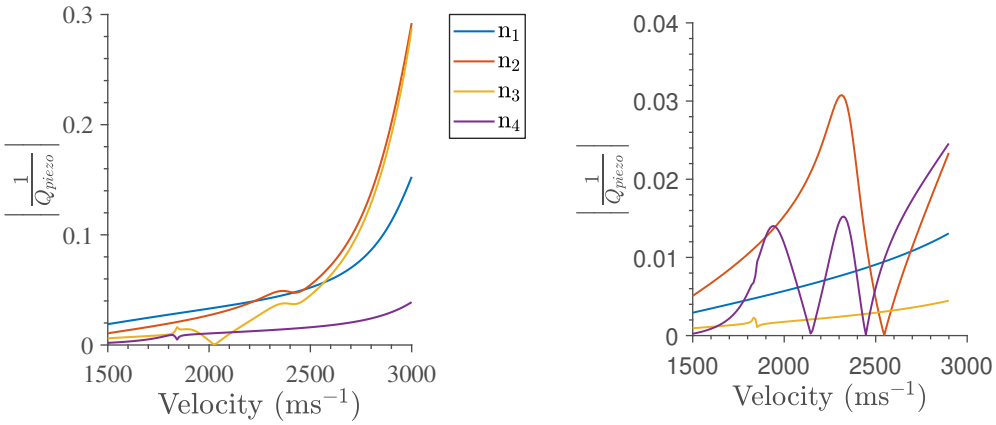

(a) Quartz (b) $LiNbO_3$

Fig. 7.9 Inverse Q-factor for loss through piezoeletric coupling, with real piezoelectric and dielectric constants, in the first four SAW modes of SU-8 ($\eta = 0.0$) loaded on (a) quartz and (b) lithium niobate, within the non-leaky velocity range.

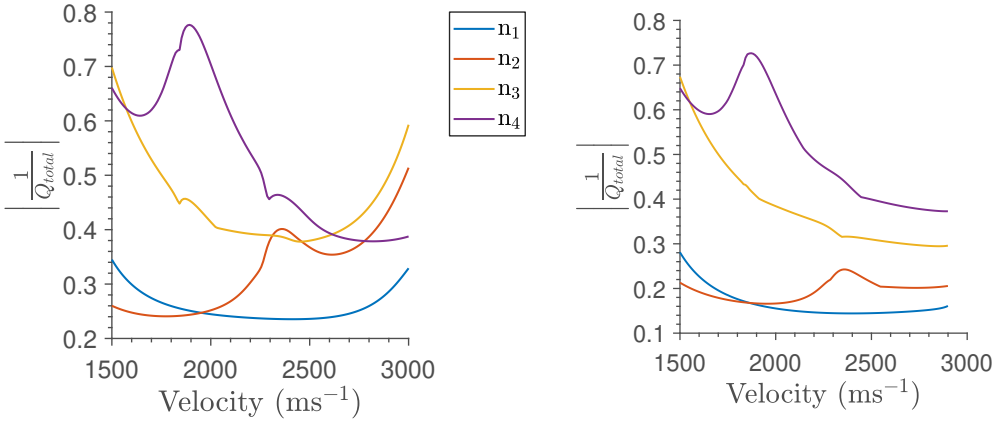

(a) Quartz (b) $LiNbO_3$

Fig. 7.10 Inverse total Q-factor for the first four SAW modes of SU-8 loaded on (a) quartz and (b) lithium niobate, within the non-leaky velocity range.

For all computed modes the greatest forms of attenuation is the viscoelastic loss, which also dominates the total Q-factor. The second mode for Quartz has a large thermoelastic peak, which is expected to be higher to due to the underestimation of the peak by the uncoupled approximation. Otherwise, the Q-factors for the two materials are more or less consistent, except for values closer to 3000ms^{-1} due to a attenuated peak in the piezoelectric Q-factor for quartz. The loss in the piezoelectric part is not due to complex piezoelectric or dielectric coefficients. Instead the attenuation is required to match the boundary conditions of the SU-8 and piezoelectric substrate materials.

7.5 Conclusion

In this chapter the extensions to thermoelastic and piezoelectric behaviours in the numerical model were achieved. For the thermoelastic extension, the goal was to make an approximation of Q-factor in 3-dimensional multilayered anisotropic combinations. Modelling the piezoelectric behaviour is required for designing MEMS that make use of the piezoelectric coupling to excite waveforms. Additionally, the piezoelectric coupling can alter the structure of the slowness curves used to design annular transducers. For the case of SU-8 on piezoelectric substrates, no significant change, due to the piezoelectric coupling, was present. For this case, this is due to the dominant isotropic dielectric layer, and should not be considered true for all cases involving lithium niobate.

For the particular cases presented of SU-8 on lithium niobate and on quartz, the Q-factor data was computed for multiple loss mechanisms. The dominant form of attenuation was due to the viscoelastic layer, which dominated the structure of the combined Q-factor. This form of attenuation is near identical between the two substrates, due to the dominate dynamics of the isotropic layer. Fluid behaviour has the lowest attenuation, this result is consistent with the data presented in Chapter 6 for the comparison of isotropic and anisotropic fluid loading.

For thermoelastic loss and the attenuation required for piezoelectric wave propagation, the attenuation of quartz is significant enough to impact the structure of the combined Q-factor. As for the lithium niobate substrate the attenuation due to these loss mechanisms remains an order of magnitude lower than the viscoelastic loss. The viscoelastic loss in the lithium niobate case dominates the structure of the combined Q-factor.

Chapter 8

Conclusion

8.1 Introduction

In this final chapter the outcomes of each of the major chapters will be discussed in the context of the research as a whole. The limitations of research in each of these chapters will be discussed, this will lead onto the recommendations for further work. Additionally, the original research questions posed in Chapter 1 will be reviewed in this chapter.

8.2 Review of Outcomes

In this section the outcomes for all major sections are reviewed in view of the original objectives and the overall research.

8.2.1 Chapter 3

One of the main requirements for studying the behaviour of multilayered waveforms for biosensor application is a robust numerical model. At the transition points for a material, corresponding to the bulk wave solutions, the complex partial wave solutions coalesce on the real axis and then seperate. At these points, the gradient based tracking methods suffer a loss of information on the location of the partial roots. The structure of the function depends heavily on the symmetry and rotation of the stiffness tensor for the anisotropic material. For attenuated cases these solutions can be rotated back into the complex plane, rendering methods that sweep along an axis useless. As stated in the objectives, the numerical method must be general enough to handle multiple material symmetries, properties and forms of attenuations.

It has been shown that the functions of the partial wave eigenvalue problem and boundary condition determinant are holomorphic. A novel method based on the curves of constant phase has been developed which makes use of both the phase and magnitude of the function. This method has been shown to be capable of computing materials with varied anisotropic stiffness, boundary conditions and attenuation mechanisms. A hybrid search by golden sections and curves of constant phase method has been developed for the fixed frequency. This allowed for the computation of problems for biosensor application, opposed to the fixed velocity cases which were limited to the existence problem. Therefore the robust and generalised numerical method has been developed which may be used to investigate the changing behaviour of SAW solutions and biosensor design.

A polar formulation, of the numerical methods of this problem, has not been developed. Instead the approach to use the plane wave formulation to approximate a point loaded Green's function is used in Chapter 5. The major advantage comes from the integrated approach to modelling waves in anisotropic layered, resulting in a general method that may be applied to many biosensor cases. Using the plane wave approach allows for the use of the modular coding methods developed, which may be efficiently tailored to particular problems of interest.

8.2.2 Chapter 4

Waveforms that only have pure sinusoidal variation in the direction of propagation are only a small group of waveforms of interest for biosensor applications. In in real world, just as with isotropy, these waveforms are an approximation which is suitable for first concept designs but not detailed optimisation. This case is limited, to capture solutions closer to the real world case, decay must also be allowed in the propagating direction which siginificantly increases the number of waveforms which may be modelled. In an elastic medium these are LSAWs, the methods developed in Chapter 3 allow for the search of these solutions in the complex plane of wavenumber or frequency. Modelling these LSAWs is required for characterisation of SAWs within layered anisotropic media, which may also lead to insight on novel sensor designs, as stated in the objectives.

In this chapter the interaction between differing anisotropic symmetries, namely quasi-6-fold Z-cut quartz on 4-fold (100) cubic, was investigated close to leaky transition regions. For the non-leaky range, the interaction of the 2-dimensional dispersion of the waveguide and anisotropy was presented. The resulting variation in solution surfaces, with angle, was increased by the leaky transition, which occurs at particular propagation angles. This rapid shifting of the solution

surfaces could prove useful for sensor design, this will be discussed further in the limitations and further work section.

As stated in one of the objectives, the cyclic variation of solutions due to anisotropic dispersion is of interest for application to clyindrical sensor design. In this chapter multiple mechanisms that impact the cyclic symmetry and their interaction have been presented for the fixed velocity case. For biosensor application, the velocity surfaces for a fixed real frequency value, have been computed for the same problem. The same leaky dispersive structure is also present in these curves, along with the waveguide and anisotropic dispersions.

8.2.3 Chapter 5

Viscoelastic materials such as SU-8 epxoy or Polymethyl methacrylate (PMMA) are used for components of biosensors, additionally many biological substances are also viscoelastic. Viscoelastic elements of multilayered biosensor designs have reporterly been the main source of energy loss in layered SAW devices. The formulation of this loss mechanism is a key step in the comparison of multiple forms of attenuation, stated as a biosensor objective. As a secondary objective, the cyclic symmetry of the wavenumber solutions is studied in this chapter, but now with viscoelastic loss.

The existence of attenuated solutions was expected and shown to exist; the attenuation, as expected from the literature, is frequency dependent in the partial wave solutions. The focus was placed on isotropic SU-8 layered on Z-cut trigonal lithium niobate, unlike in Chapter 4, this is a currently feasible combination. The viscoelastic loss has been shown to rotate the wavenumber surfaces into the complex plane, which may be uniformal or variable with angle.

The velocity surfaces for a fixed real frequency value have been computed for the half-space and SU-8 layered problem of lithium niobate. As with the previous chapter, the cyclic symmetry of solutions is of interest for application, stated in the objectives. Using the approximate Green's function method, the shaped annular transducer for the half-space problem has been designed. For the SU-8 layered case, an investigation into the character of the fixed frequency surfaces was presented instead of a design outline. This is due to the number of possibilities resulting from dispersion and viscosity, along with the significantly lower cyclic variation of this problem.

8.2.4 Chapter 6

Attenuation due to fluid loading is one of the earliest problems to be faced by mechanical sensors used in biosensing applications. As with the previous chapter, stated in the objectives, the focus is

the formulation of the energy loss and the resulting cyclic symmetry. For fluid loading, the extra objectives of isotropic verse anisotropic, and Rayleigh verse Love type displacements was of interest. In addition, in this chapter, the generalised displacements for anisotropic combinations was investigated in the mechanical case for the prediction of fluid attenuation.

The linearised fluid loading model has been developed using the small signal approximation, the viscoelastic tensor is used to capture shear horizontal coupling. The starting point of this formulation was the 3-dimensional equations, methods in the literature typically use 3-dimensional extensions of 1-dimensional equations. The resulting set of equations must be solved together, a coupled eigenvalue problem, to determine the unknown displacements. This novel approach allows the fluid formulation to be integrated into the current formulation as a module. Therefore, the fluid can be easily introduced into the boundary condition problem, allowing the efficient generation of code for a large number of cases.

The attenuation of Rayleigh type displacements in an isotropic layered medium is shown to be larger than the Love wave attenuation for large layer thicknesses. The attenuation of the Love wave remains small and within a similar range, over large change in magnitude of the thickness, while the Rayleigh wave attenuation decreases as thickness decreases. For small thicknesses within typical MEMS biosensor ranges, the attenuation of the Rayleigh wave approaches the same range as the Love wave attenuation.

A focus of this chapter, in addition to fluid loading, was the compatiblity between layer and substrate materials, briefly outlined in Chapter 2. For the mechanical case the lower compatibility resulted in increased averaged out-of-plane displacements at the surface of the material. An interesting point for both cases, the cyclic symmetry was 2-fold with a dominant 6-fold shape, dependent on the mode. Therefore, with the loading of the fluid, the cyclic symmetry of all modes was altered by the attenuation. The attenuation is larger than the isotropic case, with significantly higher attenuation for the incompatible combination.

8.2.5 Chapter 7

Several types of attenuated behaviour has been investigated throughout the course of this thesis, in this chapter these loss mechansims are compared in a common case. The objective is to indentify the major form of attenuation and to optimise these in relation to biosensor design. The optimisation is a significant undertaking, due to the many variables and design parameters that may be considered for SAW sensors. In this chapter, the focus is placed on the comparison between forms of attenuation, and development of methology. The additonal formulation of

thermoelastic loss is undertaken in this chapter, along with the piezoelectric formulation, required to model the piezoelectric coupling.

The comparison of loss mechanisms was undertaken for SU-8 on Z-cut lithium niobate, the same case covered in Chapter 5, and on Z-cut quartz for comparison. For both the total Q-factor was dominated by the viscoelastic loss of the layer, with identical mechanical structures implying dominant isotropic layer propagation. For quartz, some additional contributions are present due to thermoelastic loss and piezoelectric propagation requiring a complex wavenumber. The fluid loss, for both cases, is insignificant due to the use of an isotropic layer, as suggested in Chapter 6. For SU-8 on lithium niobate, the dispersion structure with piezoelectric coupling matches the mechanical slowness.

8.3 Scope and Limitations

For each chapter the relevance of the limitations and scope of the work is reviewed in the context of the application of MEMS biosensors, and the physical understanding of SAW mode behaviour.

8.3.1 Chapter 3

The numerical models that have been developed can be applied to any complex holomorphic function. When compared to grid based methods, the numerical model suffers increased computation time with an increase in the number of solutions, within the search range. Although grid methods can also increase in computation times, dependent on the method, location of solutions and initial conditions. This is not an issue for the partial wave problem, which only has six to eight solutions in the cases presented. For the boundary condition determinant, only the first few modes of a problem are relevant for biosensor application and so this is acceptable in the context of this application.

8.3.2 Chapter 4

The material combination that has been investigated is quartz on silicon; these anisotropic combinations are uncommon in biosensing technology. Literature of the bonding or growth of these materials, using an intermediate layer, exist to a limited extent. The major limitation is the state of technology for bonding of different types of anisotropic substrate. Another problem could arise is the bonding approach, if it makes use of a viscoelastic layer, which has been shown to attenuate energy, in this case as constrained layer damping. Many possible material

combinations exist in which symmetric leaky behaviour may be introduced for rapid shifting of slowness structure. The methods developed in this thesis may be used to test the feasibility, along with other possible materials to be used in such a device. The commercial viability of such research may generate the motivation required to further research crystal bonding.

8.3.3 Chapter 5

Modelling of 3-dimensional wave based viscoelastic behaviour is used for a wide range of applications including MEMS devices and vibrational control. Allowing the material to have anisotropic properties, expands the number of cases this can be used for biosensor application, such as SU-8 or biological elements on the quartz on silicon problem. The methods are based on plane wave formulation, this means that they can also be readily applied to optimise traditional linear devices.

8.3.4 Chapter 6

A model that captures the shear and out-of-plane coupling between a fluid and solid interface has been developed, this linearised fluid model has been built for just the interface problem. A wide scope of cases have been presented, the effect of mutliple wave types has been investigated along with isotropic and anisotropic layers. The results can hint at the behaviours for a wide range of interface cases, although it is most reliable at small amplitude ranges for applications in MEMS devices. Additionally, the numerical method can be readily used for many more multilayered cases and anisotropic material properties due to the modularity. This means that it is also compatible with the piezoelectric and viscoelastic formulations, for the study of interface wave types.

The scope of the investigation was, unfortunately, limited to modelling only water for fluid loading of SAW solutions. Other fluids may be modelled, provided that the input region in the partial wave tracker is sufficiently coded for large variations in magnitude. The properties of these fluids need to be representable in the form of a viscosity tensor, which for this work must remains constant. Another mechanism which is not fully explored in this chapter is change due to dispersion, though this is investigated in Chapter 7 it is only for a single case of an isotropic layer. The work provides a good overview of the expected attenuation range for isotropic and anisotropic layers on a substrate.

8.3.5 Chapter 7

The Q-factor comparison is limited to two particular cases of SU-8 on lithium niobate and quartz substrates, even so these provide insight in many relevant biosensor cases. Firstly, the cases in which the layer can be assumed to be isotropic and secondly, when the layer is viscoelastic or a sensor has viscoelastic elements loaded onto the surface. A case in which these results can not yield much insight, is the leaky concept in Chapter 4 of 3-fold (quasi-6-fold) Z-cut quartz on 4-fold silicon. This case combines an anisotropic layer with directionally dependent leaky behaviour and is currently beyond the scope of this investigation. It is important to state that even though these results have not been presented for this case, the methods developed can readily generate the required data. In fact the general approach to modelling these different forms of attenuation, means that this Q-factor model can represent a large number of systems, not just in MEMS sensors.

The Q-factors are modelled independently, due to a combination of computational time and required level of detail. The Q-factor provides a suitable view of the sources of energy loss for biosensor technology and the magnitude of attenuation. The limitation is that it does not provide insight into how these loss mechanisms interact with each other. Therefore, this model remains an approximation tool only and should not be used to further infer the complicated behaviour of these interactions, which is beyond the scope of this thesis.

In the review section of this chapter, it was stated that the optimisation problem was also dependent on the SAW mode selected, with the in-plane SAW being a suitable option. The major problem is the technological limitations in exciting a radial propagating Love wave using linear polarised piezoelectric materials, due to the coupling coefficients. A possibility beyond the scope of this research is to make use of generalised displacements of anisotropic materials. These displacement forms will be some combination of Rayleigh and shear horizontal displacements, briefly explored in Chapter 6. The optimisation problem would then become a balance between the attenuation of these generalised displacements and the ability to excite, also known as the coupling factor.

8.4 Review of Research Questions

1. *In the layered half-space problem, the wavelength may vary from small to large values, due to the interaction of waveguide dispersion and SAW decay behaviour. How does the symmetry of the solution relate to the symmetry of the material? How do the symmetries of the contributing materials interact to give rise to the symmetry of the multilayered solution? And does the solution symmetry smoothly transition between that of the layer and of the substrate, dependent on the layer thickness?*

   Comment: Solution surfaces are some combination of the symmetries of the individual contributing materials, dependent on the waveguide dispersion. For particular modes, the structure is a smooth transiton between the symmetries of the contributing materials with change in wavelength. These cases are believed to be dominated by shear horizontal displacements, whereas the out-of-plane displacements would couple the layers together. In these out-of-plane cases, the 2-fold symmetry is always present, but is dominated by either the layer or substrate symmetries.

2. *What are the most significant forms of energy loss for mechanical SAW biosensors using anisotropic multilayered waveforms? How can these forms be mitigated from a design and material perspective?*

   Comment: For the case of an isotropic viscoelastic layer, the attenuation is dominated by the viscoelasitc layer. This case was conducted for a low value of shear viscosity, for SU-8 photoresist from the literature. For an anisotropic layer, evidence is presented for a high coupling to a loaded fluid layer which is expected to be the dominant source of attenuaton.

3. *For the pure isotropic case, the loss due to fluid loading is assumed to be small in Love waves, compared to Rayleigh waves. To what degree is this true? And how does this differ in an anisotropic case?*

   Comment: Rayleigh waves have a higher attenuation than Love waves in isotropic media, although at small layer thicknesses in the range of MEMS design the attenuation is within a similar range. The half-space Rayleigh wave and layered Love wave comparison remains untested, but it is expected that the Rayleigh loss is comparible to large thicknesses of multilayered Rayleigh type displacements. In the anisotropic cases explored the differences are much more significant.

4. *For multilayered SAW modes within a layered medium, comprised of conflicting symmetries, how do the generalised displacements lead to increased or decreased energy loss? And how does the energy loss now vary with the propagation angle?*

   Comment: For incompatible symmetries, the attenuation due to fluid loading has been shown to be higher, due to the larger variation in generalised mode displacement. The attenuation can either be an uniform rotation of the solution surface into the complex plane, or the attenuation can be directional dependent. This is based on the symmetries of the contributing anisotropic materials and the loss mechanism being investigated.

5. *What will the form of the displacement be for the generalised versions of the well-known isotropic wave types in different layered anisotropic media? And how will this impact the piezoelectric coupling of these modes? Is it possible to produce and detect a shear dominated waveform by out-of-plane transducer coupling?*

   Comment: This remains an open question, the generalised displacements have been shown to be combinations of the Rayleigh and shear horizontal displacements. Due to this, it would be reasonable to assume that a generalised in-plane shear dominant modes may be excited by out-of-plane coupling. The degree of this coupling has not been explored in the course of this investigation, but could be approximated by comparing the piezoelectric and mechanical solutions. Note this would have to be considered when taking advantage of these anisotropic concepts for sensor design, discussed in further work.

8.5 Recommendations and Further Work

The following is a brief summary of several recommended research routes or projects that can further develop on the research conducted in this thesis.

1. Continue the development of the layered lithium niobate cylindrical device, using shaped annular transducers. The starting points for this work should be the half-space case and the SU-8 waveguide case. Some of the following steps maybe be considered for this route.

    - Develop and test a number of devices for the half-space lithium niobate and the SU-8 layered variant, using circular or shaped annular transducers.
    - Investigate the fluid loading loss for both cases, based on the finding in this thesis, the loss for the generalised anisotropic half-space Rayleigh wave should be significantly larger than the isotropic layered case.
    - Conduct optimisation of the Q-factor and sensing mechanism, as the start of the development of a commerical device, making use of the automated slowness and transducer design tools. This may involve expanding the material selection for more suitable layer options.

2. An expanded numerical investigation into the layered anisotropic stiffness problem close to transition regions. This may involve some of the following steps.

    - Increasing the number of materials and standard cuts of these materials. Starting with the case of isotropic on anisotropic materials.
    - Investigate the feasibility of activating embedded layers, as part of the n-layers problem. Compare the differences between SAW and LSAW modes when lower layers are present. These layers will have lower bulk velocities than higher layers.
    - For particular cases, investigate the Q-factor and frequency shift behaviour under mass loading.
    - Investigate the variation in electromagnetic coupling and generalised displacements pattern around the multilayered cut.

    If a potential candiate is identified for a cylindrical geometry biosensor, then investigate the feasibility of material bonding or crystal growth. Design the shaped annular transduers

for the particular mode of interest, and excited a multilayered polar form SAW mode, close to an anisotropic leaky transiton point. Note that the results shown in Chapter 4 is for initial data, for only two materials, without optimisation for improved frequency shift.

3. Investigate the behaviour of generalised modes in materials with anisotropic stiffness, along with the relative out-of-plane to in-plane shears displacements. The objective is to excited dominate in-plane shears by piezoelectric coupling through the out-of-plane component and to enchance this coupling. An extra note, the further development of annular transducer manufacturing techniques will allow for sophisticated design such as adjustable IDT grids. This may be important for anisotropic combination in which the relative displacement types vary with propagation angle. With the constant improvement in the state of technology may come the ability to regional adjust piezoelectric coupling and develop adjustable MEMS based metamaterials. Biosensor designs that make use of annular transducers and anisotropic dispersive structures could prove to be a motivation for the development of advanced MEMS manufacturing and material polarisation techniques.

8.6 Concluding Remarks

The central focus of this thesis has been on the physical mechanisms that effect the cyclic symmetry of SAW modes in multilayered combinations. The goal of this investigation has been to develop the required numerical framework to investigate these problems in the context of MEMS biosensor applications. It has been shown that the effects of waveguide dispersion, anisotropy and a number of energy loss mechanisms can alter the slowness structure of various material combinations. Additionally, a comparison between these sources of energy loss in a dispersive, and anisotropic feasible SAW biosensor example has been conducted. To build on the research conducted in this thesis, it is recommended that the anisotropic structure be explored for a greater range of materials. The physical behaviours that may be used in novel sensor design requires the further development of MEMS manufacturing techniques.

References

Chapter 1

[1] S.K. Vashist, P.B. Luppa, L.Y. Yeo, A. Ozcan, and J.H.T. Luong. Emerging Technologies for Next-Generation Point-of-Care Testing. Trends in Biotechnology, 2015, 33(11), pp. 692-705.

[2] M.M. Pereira da Silca Neves, M.B. González-García, D. Hernández-Santos, and P. Fanjul-Bolado. Future trends in the market for electrochemical biosensing. Current Opinion in Electrochemistry, 2018, 10, pp. 107-111.

[3] M.E.G. Bigelow, B.G. Jamieson, C.O. Chui, Y. Mao, K-S. Shin, T.J. Huang, P-Hsun. Huang, L. Ren, B. Adhikari, J. Chen, and E. Iturriaga. Point-of-Care Technologies for the Advancement of Precision Medicine in Heart, Lung, Blood, and Sleep Disorders. IEEE Journal of Translational Engineering in Health and Medicine, 2016, 4, doi:10.1109/JTEHM.2016.2593920

[4] B.J. Gallacher, J.S. Burdess, Z.X. Hu, H.T. Grigg, C. Dale, J. Hedley, C. Fu, J. Spoors, N. O'Meara, and N. Keegan. Experimental verification of a quasi-trapped degenerate mode magnetic acoustic resonator, Sensor and Actuators A: Physical, 2018, 269, pp. 238-248.

[5] J.S. Burdess, B.J. Gallacher, H.T. Grigg, Z.X. Hu, C. Dale, N. Keegan, J. Hedley, C. Fu, and J. Spoors. The theory of a trapped degenerate mode resonator. The Journal of the Acoustical Society of America, 2017, 141, pp. 4622-4632.

[6] H.T.D. Grigg, T.H. Hanley and B.J. Gallacher. Degeneracy Breaking, Modal Symmetry and MEMS Biosensors. Proceedings of the COMSOL Conference, Rotterdam, 2013.

[7] R.S. Burlage, and J. Tillmann. Biosensors of bacterial cells. Journal of Microbiological Methods, 2017, 138, pp. 2-11.

[8] M.I. Mohammed, and M.P. Desmulliez. Lab-on-a-chip based immunosensor principles and technologies for the detection of cardiac biomarkers: a review. Lab on a Chip, 2011, 11(4), pp. 569-595.

[9] S. Neethirajan, S.K. Tuteja, S-T, Huang, and D. Kelton. Recent advancement in biosensors technology for animal and livestock health management. Biosensors and Bioelectronics, 2017, 98, pp. 398-407.

[10] S. Singh. Sensors - An effective approach for the detection of explosives. Journal of Hazardous Materials, 2007, 144(1-2), pp. 15-28.

[11] P. Leonard, S. Hearty, J. Brennan, L. Dunne, J. Quinn, T. Chakraborty, and R. O'Kennedy. Advances in biosensors for detection of pathogens in food and water. Enzyme and Microbial Technology, 2003, 32(1), pp. 3-13.

[12] D. Ivnitski, I. Abdel-Hamid, P. Atanasov, and E. Wilkins. Biosensors for detection of pathogenic bacteria. Biosensors and Bioelectronics, 1999, 14(7), pp. 599-624.

[13] Z. Junhui, C. Hong, and Y. Ruifu. DNA based biosensors. Biotechnology Advances, 1997, 15(1), pp. 43-58.

[14] M.A. Cooper. Label-free screening of bio-molecular interactions. Analytical and Bioanalytical Chemistry, 2003, 377(5), pp. 834-842.

[15] R. Konradi, M. Textor, and E. Reimhult. Using Complementary Acoustic and Optical Techniques for Quantitative Monitoring of Biomolecular Adsorption at Interfaces. Biosensors, 2012, 2(4), pp. 341-376.

[16] M.A. Cooper, and C. Whalen. Profiling molecular interactions using label-free acoustic screening. Drug Discovery Today: Technologies, 2005, 2(3), pp. 241-245.

[17] M.A. Cooper. Non-optical screening platforms: the next wave in label-free screening?. Drug Discovery Today, 2006, 11(23-24), pp. 1068-1074.

[18] E.R. Hirst, Y.J. Yuan, W.L. Xu, and J.E. Bronlund. Bond-rupture immunosensors - A review. Biosensors and Bioelectronics, 2008, 23, pp. 1759-1768.

[19] I. Voiculescu, and A.N. Nordin. Acoustic wave based MEMS devices for biosensing applications. Biosensors and Bioelectronics, 2012, 33, pp. 1-9.

[20] Y.Q. Fu, J.K. Luo, N.T. Nguyen, A.J. Walton, A.J. Flewitt, X.T. Zu, Y. Li, G. McHale, A. Matthews, E. Iborra, H. Du, and W.I. Milne. Advances in piezoelectric thin films for acoustic biosensors, acoustofluidics and lab-on-chip applications. Progress in Materials Science, 2017, 89, pp. 31-91.

[21] M. Pohanka. Overview of Piezoelectric Biosensors, Immunosensors and DNA Sensors and Their Applications. Materials, 2018, 11(3), 448.

[22] M. Pohanka. The Piezoelectric Biosensor: Principle and Applications, a review. International Journal of Electrochemical Science, 2017, 12, pp. 496-506.

[23] I. Katardjiev, and V. Yantechev. Recent developments in thin film electro-acoustic technology for biosensor applications. Vacuum, 2012, 86, pp. 520-531.

[24] W. Pang, H. Zhao, E.S. Kim, H. Zhang, H. Yu, and X. Hu. Piezoelectric microelectromechanical resonant sensors for chemical and biological detection, 2012, 12(1), pp. 29-44.

[25] S. Xu. Electromechanical biosensors for pathogen detection. Microchimica Acta, 2012, 178(3-4), pp. 245-260.

[26] M. Saitakis, and E. Gizeli. Acoustic sensors as a biophysical tool for probing cell attachment and cell/surface interactions. Cellular and Molecular Life Sciences, 2012, 69(3), pp. 357-371.

[27] K. Länge, B.E. Rapp, and M. Rapp. Surface acoustic wave biosensor: a review. Analytical and Bioanalytical Chemistry, 2008, 391(5), pp. 1509-1519.

[28] Z. Xu, and Y.J. Yuan. Implementation of guiding layers of surface acoustic wave devices: A review. Biosensors and Bioelectronics, 2018, 99, pp. 500-512.

[29] L. Bo, C. Xiao, C. Hualin, M.A. Mohammad, T. Xiangguang, T. Luqi, and R. Tianling. Surface acoustic wave devices for sensor applications. Journal of Semiconductors, 2016, 37(2), pp. 1-9.

[30] M-I, Rocha-Gaso, C. March-Iborra, A. Montoya-Baides, and A. Arnau-Vives. Surface Generated Acoustic Wave Biosensors for the Detection of Pathogens: A Review. Sensors, 2009, 9, pp. 5740-5769.

[31] T.M.A, Gronewold. Surface acoustic wave sensors in the bioanalytical field: Recent trends and challenges. Analytica Chimica Acta, 2007, 603(2), pp. 119-128.

[32] Y. Zhang, J. Luo, A.J. Flewitt, Z. Cai, and X. Zhao. Film bulk acoustic resonators (FBARs) as biosensors: A review. Biosensors and Bioelectronics, 2018, 116, pp. 1-15.

[33] G. Wingqvist. AlN-based spuuter-deposited shear mode thin film bulk acoustic resonator (FBAR) for biosensor applications - A review. Surface and Coatings Technology, 2010, 205, pp. 1279-1289.

[34] M. Kasper, H. Stadler, T. Weiß, and C. Ziegler. Thickness shear mode resonators ("mass-sensitive devices") in bioanalysis. Fresenius' Journal of Analytical Chemistry, 2000, 366(6-7), pp. 602-610.

[35] B.N. Johnson, and R. Mutharasan. Biosensing using dynamic-mode cantilever sensors: A review. Biosensors and Bioelectronics, 2012, 32, pp. 1-18.

[36] H. Saberkari, H.B. Ghavifekr, and M. Shamsi. Comprehensive Performance Study of Magneto Cantilevers as a Candidate Model for Biological Sensors used in Lab-on-a-Chip Applications. Journal of Medical Signals and Sensors, 2015, 5(2), pp. 77-87.

[37] C. Ziegler. Cantilever-based biosensors. Analytical and Bioanalytical Chemistry, 2004, 379(7-8), pp. 946-959.

[38] L.A. Kuznetsova, and W.T. Coakley. Applications of ultrasound streaming and radiation force in biosensors. Biosensors and Bioelectronics, 2007, 22, pp. 1567-1577.

[39] A. Sarvazyan. Diversity of biomedical applications of acoustic radiation force. Ultrasonics, 2010, 50, pp. 230-234.

[40] X. Yu, W. Zhang, P. Zhang, and Z. Su. Fabrication technologies and sensing applications of graphere-based composite films: Advances and challenges. Biosensors and Bioelectronics, 2017, 89, pp. 72-84.

[41] J.Y. Chen, L.S. Penn, and J. Xi. Quartz crystal microbalance: Sensing cell-substrate adhesion and beyond. Biosensors and Bioelectronics, 2018, 99, pp. 593-602.

[42] X. Qiao, X. Zhang, Y. Tian, and Y. Meng. Progresses on the theory and application of quartz crystal microbalance. Applied Physics Reviews, 2016, 3(3).

[43] H. Ogi. Wireless-electrodeless quartz-crystal-microbalance biosensors for studying interactions among biomolecules: A review. Proceedings of the Japan Academy, Series B Physical and Biological Sciences, 2013, 89(9), pp. 401-417.

[44] G.N.M. Ferreira, A-C. da-Silva, and B. Tomé. Acoustic wave biosensors: physical models and biological applications of quartz crystal microbalance. Trends in Biotechnology, 2009, 27(12), pp. 689-697.

[45] R.E. Speight, and M.A. Cooper. A Survey of the 2010 Quartz Crystal Microbalance Literature. Journal of Molecular Recognition, 2012, 25(9), pp. 451-473.

[46] B. Becker, and M.A. Cooper. A Survey of the 2006-2009 Quartz Crystal Microbalance Biosensor Literature. Journal of Molecular Recognition, 2011, 24(5), pp. 754-787.

[47] M.A. Cooper, and V.T. Singleton. A survey of the 2001 to 2005 quartz crystal microbalance biosensor literature: applications of acoustic physics to the analysis of biomolecular interactions. Journal of Molecular Recognition, 2007, 20(3), pp. 154-184.

[48] A. Arnau. A Review of Interface Electronic Systems for AT-cut Quartz Crystal Microbalance Applications in Liquids. Sensors, 2008, 8(1), pp. 370-411.

[49] V. Matko. Next Generation AT-Cut Quartz Sensing Devices. Sensors, 2011, 11(5), pp. 4474-4482.

[50] J.C. Andle, and M.G. Schweyer. Acoustic plate mode properties of rotated Y-Cut quartz. IEEE Ultrasonics Symposium, San Antonio, Texas, USA, 3-6 Nov. 1996, pp. 532-540.

[51] A. Isobe, M. Hikita, and K. Asai. Propagation Properties of Love Wave-Type Surface Acoustic Wave on α-Quartz. Electronics and Communications in Japan (Part II: Electronics), 1996, 79(2), pp. 24-30.

[52] C.K. O'Sullivan, and G.G. Guilbault. Commercial quartz crystal microbalances - theory and applications. Biosensors and Bioelectronics, 1999, 14(8-9), pp. 663-670.

[53] M.A. Shiryaev, S.A. Eremin, and A.N. Baranov. Biosensors Based on Zinc Oxide. Nanotechnologies in Russia, 2014, 9(3-4), pp. 99-115.

[54] N. Izyumskaya, A. Tahira, Z.H. Ibupoto, N. Lewinski, V. Avrutin, Ü. Özqür, E. Topsakal, M. Willander, and H. Morkoç. Review - Electrochemical Biosensors Based on ZnO

Nanostructure. ECS Journal of Solid State Science and Technology, 2017, 6(8), pp. Q84-Q100.

[55] S.K. Arya, S. Saha, J.E. Ramirez-Vick, V. Gupta, S. Bhansali, and S.P. Singh. Recent advances in ZnO nanostructures and thin films for biosensor applications: Review. Analytica Chimica Acta, 2012, 737, pp. 1-21.

[56] A. Tereshchenko, M. Bechelany, R. Viter, V. Khranovskyy, V. Smyntyna, N. Starodub, and R. Yakimova. Optical biosensors based on ZnO nanostructures advantages and perspectives. A review. Sensors and Actuators B: Chemical, 2016, 229, pp. 664-677.

[57] Y.Q. Fu, J.K. Luo, X.Y. Du, A.J. Flewitt, Y. Li, G.H. Markx, A.J. Walton, and W.I. Milne. Recent developments on ZnO films for acoustic wave based bio-sensing and microfluidic applications: a review. Sensors and Actuators B: Chemical, 2010, 143(2), pp. 606-619.

[58] M. Ferrari, and G.C. Johnson. The equilibrium properties of a 6mm polycrystal exhibiting transverse isotropy. Journal of Applied Physics, 1988, 63(9), pp. 4460-4468.

[59] L. Su, L. Zou, C-C. Fong, W-L. Wong, F. Wei, K-Y. Wong, R.S.S. Wu, and M. Yang. Detection of cancer biomarkers by piezoelectric biosensor using PZT ceramic resonator as the transducer. Biosensors and Bioelectronics, 2013, 43, pp. 155-161.

[60] H-C. Lu, W-K. Lai, and H-C. Young. Preparation and Application of Sub-micron Lead Zirconium Titanate Surface Acoustic Wave Biosensors. 3rd Interactional Nanoelectronics Conference, Hong Kong, China, 3-8 Jan. 2010.

[61] T. Xu, and J. Miao. Investigation of the Effect of Adsorption Induced Surface Stress on the Resonant Frequency of PZT Membrane Based Biosensors. Proceedings of the 5th IEEE International Conference on Nano/Micro Engineered and Molecular Systems, Xiamen, China, 20-23 Jan. 2010, pp. 569-572.

[62] Y. Lee, G. Lim, and W. Moon. A self-excited micro cantilever biosensor actuated by PZT using the mass micro balance technique. Sensors and Actuators A: Physical, 2006, 130-131, pp. 105-110.

[63] Y.S. Lee, D.S. Yoon, and T.S. Kim. Improvement of the Mass Sensitivity in Flexural Plate Wave Biosensor Based on PZT Thin Film. Integrated Ferroelectrics, 2005, 69, pp. 391-400.

[64] N. Keegan, J. Hedley, Z.X. Hu, J.A. Spoors, W. Waugh, B.J. Gallacher, and C.J. McNeil. Piezoelectrically Actuated Circualr Diaphragm Resonator Mass Sensors. 7th IEEE International Conference on Nano/Micro Engineered and Molecular Systems (NEMS), Kyoto, Japan, 5-8 March 2012, pp. 73-77.

[65] P.K. Panda. Review: environmental friendly lead-free piezoelectric materials. Journal of Materials Science, 2009, 44(19), pp. 5049-5062.

[66] J. Rödal, K.G. Webber, R. Dittmer, W. Jo, M. Kimura, D. Damjanovic. Transferring lead-free piezoelectric ceramics into application. Journal of the European Ceramic Society, 2015, 35(6), pp. 1659-1681.

[67] A.E. Murillo, L. Melo-Máximo, B. García-Farrera, O.S. Martínez, D.V. Melo-Máximo, J. Oliva-Ramírez, K. García, L. Huerta, and J. Oseguera. Development of AlN thin films for breast cancer acoustic biosensors. Journal of Materials Research and Technology, 2018, https://doi.org/10.1016/j.jmrt.2018.02.007.

[68] B. García-Farrera, A.E. Murillo, D.V. Melo-Máximo, O. Salas, L. Melo-Máximo, and J. Oseguera. Effect of the Electrode Layer on the Deposition of AlN for Biosensors. Journal of Bio- and Tribo-Corrosion, 2017, 3(2), pp. 1-8.

[69] C-J. Chung, P-T. Hsieh, J-F. Lin, C-L. Wei, W-T. Chang, C-T. Chen, Y-C. Chen, C-C. Cheng, C-H. Lin, K-C. Chiu, S-J. Chen, and K-S. Kao. Investigation of Acoustic Properties and Raman Scattering of AlN Films for Biosensor Application. 6th IEEE International Conference on Nano/Micro Engineered and Molecular Systems, Kaohsiung, Taiwan, 20-23 Feb. 2011, pp. 618-621.

[70] Y.C. Chen, W.C. Shih, W.T. Chang, C.H. Yang, K.S. Kao, and C.C. Cheng. Biosensor for human IgE detection using shear-mode FBAR devices. Nanoscale Research Letters, 2015, 10, pp. 1-8.

[71] M. DeMiguel-Ramos, T. Mirea, J. Olivares, M. Clement, J. Sangrador, E. Iborra, and M. Barba. Influence of the electrical extensions in AlN-BAW resonators for in-liquid biosensors. European Frequency and Time Forum, 2014, pp. 301-304.

[72] T.Y. Lee, and J.T. Song. Detection of carcinoembryonic antigen using ALN FBAR. Thin Solid Films, 2010, 518(22), pp. 6630-6633.

[73] L. Shu, B. Peng, C. Li, D. Gong, Z. Yang, X. Liu, and W. Zhang. The Characterization of Surface Acoustic Wave Device Based on AlN-Metal Structure. Sensors, 16(4), pp. 1-10.

[74] Y-G. Li, L-X. Ma, P.M. Sarro, D-X. Du, and X-F. Liu. Mass sensitivity of aluminium nitride thin film based surface acoustic wave sensors prepared for biosensing application. Symposium on Piezoelectricity, Xi'an, China, 21-24 Oct. 2016, pp. 368-370.

[75] R.J. Jiménez Riobóo, V. Brien, and P. Pigeat. Elastic properties in different nano-structured AlN films. Journal of Materials Science, 2010, 45, pp. 363-368.

[76] Q. Rolland, S. Dupont, J. Gazalet, J-C. Kastelik, Y. Pennec, B. Djafari-Rouhani, and V. Laude. Simultaneous bandgaps in LiNbO3 phoxonic crystal slab. Optics Express, 2014, 22(13), pp. 16288-16297.

[77] T-J. Wang, W-S. Lin, and F-K. Liu. Integrated-optic biosensor by electro-optically modulated surface plasmon resonance. Biosensors and Bioelectronics, 2007, 22(7), pp. 1441-1446.

[78] O.I. Guliy, B.D. Zaitsev, I.A. Borodina, A.M. Shikhabudinov, A.A. Teplykh, S.A. Staroverov, and A.S. Fomin. The biological acoustic sensor to record the interactions of the microbial cells with the phage antibodies in conducting suspensions. Talanta, 2018, 178, pp. 569-576.

[79] I. Borodina, B. Zaitsev, A. Shikhabudinov, O. Guliy, O. Ignatov, and A. Teplykh. The Biological Sensor for Detection of Bacterial Cells in Liquid Phase Based on Plate Acoustic Wave. Physics Procedia, 2015, 70, pp. 1157-1160.

[80] J.C. Andle, J.T. Weaver, D.J. McAllister, F. Josse, and J.F. Vetelino. Improved acoustic-plate-mode biosensor. Sensors and Actuators B: Chemical, 1993, 13(1-3), pp. 437-442.

[81] S.K.R. Sankaranarayanan, R. Singh, and V.R. Bhethanabotla. Acoustic streaming induced elimination of nonspecifically bound proteins from a surface acoustic wave biosensor: Mechanism prediction using fluid-structure interaction models. Journal of Applied Physics, 2010, 108, 104507.

[82] K.J. Suthar, S.K.R.S. Sankaranarayanan, M. Richardson, and V. Bhenthanabotla. Comparison of Newtonian and non-Newtonian fluid dynamics on removal efficiency of non-specifically bound proteins in SAW biosensors, IEEE International Ultrasonics Symposium, Prague, Czech Republic, 21-25 July 2013, pp. 1347-1350.

[83] M.S. Zaghloul, T.E. Taha, A.H.A. Moustafa, and K. El-Shennawy. Modeling and Simulation of Fluid SAW-Sensors Under Acoustic Plate Mode Operation. IEEE Transactions on Instrumentation and Measurement, 2001, 50(1), pp. 95-100.

[84] Z.Y.A. Al-Shibaany, J. Hedley, and Z. Hu. Degenerate modes of operation in lithium niobate sensors. IEEE Sensors, Busan, South Korea, 1-4 Nov. 2015.

[85] Z.Y.A. Al-Shibaany, Z.J. Choong, H. Huo, J. Hedley, and Z. Hu. CNC machining of lithium niobate for rapid prototyping of sensors. IEEE Sensors, Busan, South Korea, 1-4 Nov. 2015.

[86] Z.Y.A. Al-Shibaany, J. Hedley, D. Huo, and Z. Hu. Micromachining Lithium Niobate for Rapid Prototyping of Resonant Biosensors. IOP Conference Series: Materials Science and Engineering, 2014, 65, pp. 1-6.

[87] J. Kondoh, Y. Matsui, and S. Shiokawa. New Biosensor Using Shear Hoizontal Surface Wave Device. Japanese Journal of Applied Physics, 1993, 32, pp. 2376-2379.

[88] T. Moriizumi, Y. Unno, and S. Shiokawa. New Sensor in Liquid Using Leaky SAW. IEEE Ultrasonics Symposium, Denver, Colorado, USA, 14-16 Oct. 1987, pp. 579-582.

[89] S.K.R.S. Sankaranarayanan, S. Cular, and V.R. Bhethanabotla. Finite Element modeling of hexagonal surface acoustic wave biosensor based on LiTaO3. IEEE Sensors, Lecce, Italy, 26-29 Oct. 2008, pp. 514-517.

[90] A.W. Nowek, R. Stankiewicz, M. Baran, I. Zalewska, and E. Brzozowski. ZnO thin films for applications in surface acoustic wave actuators. IEEE Sensors, Orlando, FL, USA, 30 Oct. - 3 Nov. 2016.

[91] F. Moreira, M. El-Hakiki, O. Elmazria, F. Sarry, L. Le Brizoual, and P. Alnot. Theoretical and Experimental Identification of Love Wave Frequency Peaks in Layered Structure ZnO/Quartz SAW Device. IEEE Sensors Journal, 2008, 8(8), pp. 1399-1403.

[92] R-C. Chang, S-Y. Chu, C-S. Hong, and Y-T. Chuang. A study of Love wave devices in ZnO/Quartz and ZnO/$LiTaO_3$ structures. Thin Solid Films, 2006, 498(1-2), pp. 146-151.

[93] S-Y. C, W. Water, and J-T. Liaw. An investigation of the dependence of ZnO film on the sensitivity of Love mode sensor in ZnO/quartz structure. Ultrasonics, 2003, 41, pp. 133-139.

[94] K.K. Zadeh, A. Trinchi, W. Wlodarski, and A. Holland. A novel Love-mode device based on ZnO/ST-cut quartz crystal structure for sensing applications. Sensors and Actutators A, 2002, 100, pp. 135-143.

[95] M.I. Rocha-Gaso, A. Renaudin, F. Sarry, and D. Beyssen. Lab-on-a-chip based Integrated Hybrid Technologies for Biofluids Manipulation and Characterization. Procedia Engineering, 2015, 120, pp. 687-690.

[96] A. Talbi, F. Sarry, M. Elhakiki, L. Le Brizoual, O. Elmazria, P. Nicolay, and P. Alnot. ZnO/quartz structure potentiality for surface acoustic wave pressure sensor. Sensors and Actuators A: Physical, 2006, 128(1), pp. 78-83.

[97] Z.T. Salim, U. Hashim, M.K. Md. Arshad, and M.A. Fakhri. Simulation, Fabrication and Validation of Surface Acoustic Wave Layered Sensor Based on ZnO/IDT/128°YX $LiNbO_3$. International Journal of Applied Engineering Research, 2016, 11(15), pp. 8785-8790.

[98] T-J. Huang, and C-C. Ma. Characterization of Response of ZnO/$LiNbO_3$-Based Surface Acoustic Wave Delay Line Photodetector. Japanese Journal of Applied Physics, 2008, 47(8), pp. 6507-6512.

[99] L. Rana, R. Gupta, M. Tomar, and V. Gupta. Highly sensitive Love wave acoustic biosensor for uric acid. Sensors and Actuators B: Chemical, 2018, 261, pp. 169-177.

[100] R-C. Chang, S-Y. Chu, C-S. Hong, Y-T. Chuang. An Investigation of preferred orientation of doped ZnO films on the 36°YX-$LiTaO_3$ substrate and fabrication of Love-mode devices. Surface & Coating Technology, 2002, 200, pp. 3235-3240.

[101] D.A. Powell, K. Kalantar-Zadeh, S. Ippolito, and W. Wlodarski. A Layered SAW Device Based on ZnO/$LiTaO_3$ for Liquid Media Sensing Applications. IEEE Ultrasonics Symposium, Munich, Germany, 8-11 Oct. 2002, pp. 493-496.

[102] S. Krishnamoorthy, and A.A. Iliadis. Development of ZnO/SiO_2/Si Love Mode Surface Acoustic Wave Devices with High Sensitivity for Biosensor Applications. IEEE Sensors Applications Symposium, Houston, Texas, USA, 7-9 Feb. 2006, pp. 14-17.

[103] Y-J. Hsiao, T-H. Fang, Y-H. Chang, Y-S. Chang, and S. Wu. Surface acoustic wave characteristics and electromechanical coupling coefficient of lead zirconate titanate thin films. Material Letters, 2006, 60(9-10), pp. 1140-1143.

[104] S. Li, W. Ren, X. Chen, Z. Wang, P. Shi, X. Wu, and X. Yao. Preparation of Diffuser-Type Micropumps Using PZT Thin Films Prepared by Metallo-Organic Compound Decomposition Process. Ferroelectrics, 2010, 383, pp. 144-150.

[105] A.A. Talin, S.M. Smith, S. Voight, J. Finder, K. Eisenbeiser, D. Penunuri, Z. Yu, P. Fejes, T. Eschrich, J. Curless, D. Convey, and A. Hooper. Epitaxial $PbZr._{52}Ti_{48}O_3$ films on $SrTiO_3$/(001)Si substrates depositied by sol-gel method. Applied Physics Letters, 2002, 81(6), pp. 1062-1064.

[106] F. Martin, and P. Muralt. AlN thin film as waveguide for shear acoustic waves. Applied Physics Letters, 2006, 88, 242506.

[116] M.B. Assouar, O. Elmazria, M. Elhakiki, and P. Alnot. Study of structural and microstructural properties of AlN films deposited on silicon and Quartz substrates for surface acoustic wave devices. Journal of Vacuum Science & Technology B: Mircoelectronics and Nanometer Structures Processing Measurement and Phenomena, 2004, 22, pp. 1717-1722.

[108] M-S. Lee, F-C. Chang, and S. Wu, and L. Wu. The Characterization of Surface Acoustic Wave Modes on Rotated Y-Cut Quartz (ST-X Quartz) with Different AlN Film Thickness. The Japan Society of Applied Physics, 2001, 40, pp. 4590-4592.

[109] J-H. Song, J-L. Huang, S. Wu, S-C. Wang, J-L. Ruan, and D-F. Lii. Surface acoustic wave device properties of (B, Al)N Films on 120°Y-X $LiNbO-3$ substrate. Applied Surface Science, 2010, 256, pp. 7156-7159.

[110] K.S. Kao, C.C. Cheng, Y.C. Chen, C.H. Chen. The dispersion properties of surface acoustic wave devices on AlN/$LiNbO_3$ film/substrate structure. Applied Surface Science, 2004, 230, pp. 334-339.

[111] K.S. Kao, C.C. Cheng, Y.C. Chen, Y.H. Lee. The characteristics of surface acoustic wave on AlN/$LiNbO_3$ substrates. Applied Physics A: Materials Science & Processing, 2003, 76, pp. 1125-1127.

[112] C-C. Cheng, K-S. Kao, and Y-C. Chen. Highly c-axis oriented AlN films deposited on $LiNbO_3$ substrates for surface acoustic wave devices. IEEE International Symposium on Applications of Ferroelectrics, Honolulu, HI, USA, 21 July - 2 Aug. 2000. pp. 439-442.

[113] M.Z. Aslam, V. Jeoti, S. Karuppanan, A.F. Malik, and A. Iqbal. FEM Analysis of Sezawa Mode SAW Sensor for VOC Based on CMOS Compatible AlN/SiO_2/Si Multilayer Structure. Sensors, 2018, 18(6), 1687; https://doi.org/10.3390/s18061687.

[114] S.W. Chen, H.F. Lin, T.T. Sung, J.D. Wu, H.L. Kao, and J.S. Chen. Synthesis and SAW characteristics of AlN thin films fabricated on Si and GaN using helicon sputtering system. Electronics Letters, 2003, 39(23).

[115] M.M.E.I Gowini, and W.A. Moussa. Evaluating the adhesion of SU-8 thin films using an AlN/Si surface acoustic wave sensor. Journal of Micromechanics and Microengineering, 2015, 25(3), pp. 1-14.

[116] M.B. Assouar, O. Elmazria, M. Elmazria, and P. Alnot. Study of structural and microstructural properties of AlN films deposited on silicon and quartz substrates for surface wave devices. Journal of Vacuum Science & Technology B: Microelectronics and Nanometer Structures Processing, Measurement, and Phenomena, 2004, 22, pp. 1717-1722.

[117] Y. Tang, D. Ao, W. Li, X. Zu, S. Li, Y.Q. Fu. NH_3 sensing property and mechanisms of quartz surface wave sensors deposited with SiO_2, TiO_2 and SiO_2-TiO_2 composite films. Sensors and Actuators B: Chemical, 2018, 254, pp. 1165-1173.

[118] S. Li, M. Richardson, S.K.R.S. Sankaranarayanan, C. Fan, Y. Su, V.R. Bhenthanabotla. Design and fabrication of SiO_2 waveguide-based SAW sensors with filled microcavities. IEEE Sensors, Busan, South Korea, 1-4 Nov. 2015.

[119] W. Soluch. Love wave synchronous resonator on quartz with SiO_2 layer. Electronics Letters, 2006, 42(8), pp. 495-497.

[120] G.L. Harding, J. Du. Design and properties of quartz-based Love wave acoustic sensors incorporating silicon dioxide and PMMA guiding layers. Smart Materials and Structures, 1997, 6(6), pp. 716-720.

[121] C-C. Cheng, C-J. Chang, Y-C. Chen, K-S. Kao. Temperature effect on the characteristics of surface acoustic wave on SiO_2 thin films. Ultrasonics Symposium, Montreal, Quebec, Canada, 23-27 Aug. 2004.

[122] K. Yamanouchi, and T. Ishii. High Temperature Stable Acoustic Surface Wave Substrates of SiO_2/$LiNbO_3$ Structure with Super Hugh Coupling. Japanese Journal of Applied Physics, 2002, 41, pp. 3480-3482.

[123] F.S. Hickernell, H.D. Knuth, R.C. Dablemont, and T.S. Hickernell. The Surface Acoustic Wave Propagation Characteristics of 41°Lithium Niobate with Thin-Film SiO_2. IEEE International Frequency Control Symposium, Honolulu, HI, USA, 5-7 June 1996, pp. 216-221.

[124] M. Bisoffi, B. Hjelle, D.C. Brown, D.W. Branch, T.L. Edwards, S.M. Brozik, V.S. Bondu-Hawkins, and R.S. Larson. Detection of viral bioagents using a shear horizontal surface acoustic wave biosensor. Biosensors and Bioelectronics, 2008, 23(9), pp. 1397-1403.

[125] D.W. Branch, and T.L. Edwards. Love Wave Acoustic Array Biosensor Platform for Autonomous Detection. IEEE Ultrasonics Symposium, New York, NY, USA, 28-31 Oct. 2007, pp. 260-263.

[126] K. Asai, M. Hikita, A. Isobe, K. Sakiyama, and T. Tada. Experimental and theoretical investigation for temperature characteristic and propagation losses of SAWs on SiO_2/Al/$LiTaO_3$. IEEE Ultrasonics Symposium, Munich, Germany, 8-11 Oct. 2002, pp. 235-238.

[127] J. Su, H. Esmaeilzadeh, F. Zhang, Q. Yu, G. Cernigliaro, J. Xu, and H. Sun. An ultrasensitive micropillar-based quartz crystal microbalance device for real-time measurement of protein immobilization and protein-protein interaction. Biosensors and Bioelectronics, 2018, 99, pp. 325-331.

[128] W. Wang, and S. He. Passive and Remote Polymer-coated Love Wave Chemical Sensor. IEEE Ultrasonics Symposium, Beijing, China, 2-5 Nov. 2008, pp. 1854-1857.

[129] H. Oh, C. Fu, K. Kim, and K. Lee. Wireless and Simultaneous Detection of Multiple Bio-Molecules in a Single Sensor Using Love Wave Biosensor. Sensors, 2014, 14, pp. 21660-21675.

[130] T. Song, S.Y. Song, H.C. Yoon, and K. Lee. Development of a Wireless Love Wave Biosensor Platform for Multi-functional Detection. Japanese Journal of Applied Physics, 2011, 50, pp. 1-6.

[131] W. Wang, T. Kim, K. Lee, S. Yang. Wireless Love-wave chemical sensor on 41°$LiNbO_3$. Electronics Letters, 2007, 43(22), pp. 1239-1241.

[132] Z. Li, Y. Jones, J. Hossenlopp, R. Cemosek, and F. Josse. Analysis of Liquid-Phase Chemical Detection Using Guided Shear Horizontal-Surface Acoustic Wave Sensors. Analytical Chemistry, 2005, 77, pp. 4594-4603.

[133] F. Martin, M.I. Newton, G. McHale, K.A. Melzak, and E. Gizeli. Pulse mode shear horizontal-surface acoustic wave (SH-SAW) system for liquid based sensing applications. Biosensors and Bioelectronics, 2004, 19(6), pp. 627-632.

[134] H.S. Ju, and B.R. Tittmann. Quantitative Acoustic Model for Adhension Evaluation of PMMA/Silicon Film Structures. AIP Conference Proceedings, 2010, 1211(1), pp. 1182-1189.

[135] S. Lee, K-B. Kim, and Y.Il, Kim. Love Wave SAW Biosensors for Detection of Antigen-antibody Binding and Comparison with SPR Biosensor. Food Science and Biotechnology, 2011, 20(5), pp. 1413-1418.

[136] L.E. Fissi, J-M. Friedt, F. Chérioux, and S. Ballandras. Amine functionalised SU-8 layer guiding love mode surface acoustic wave. Sensors and Actuators B: Chemical, 2010, 144(1), pp. 23-26.

[137] L-J. Wang, J-S. Liu, S-T. He. Humidity sensing by Love wave detectors coated with different polymeric films. Symposium on Piezoelectricity, Acoustic Waves, and Device Applications, Beijing, China, 30 Oct. - 2 Nov. 2014. pp. 44-47.

[138] S. Grousset, P. Lavenus, L. Benaissa, R. Taïbi, E. Augendre, T. Signamarcheix, O. Le Traon, S. Ballandras. Quartz-based vibrating MEMS fabricated using a wafer-bonding process with sealed cavities. IEEE International Frequency Control Symposium, Taipei, Taiwan, 19-22 May 2014.

[139] G.L. Drisko, A. Carretero-Genevrier, M. Gich, J. Gázquez, D. Ferrah, D. Grosso, C. Boissiére, J. Rodriguez-Carvajal, C. Sanchez. Water-Induced Phase Seperation Forming Macrostructured Epitaxial Quartz Films on Silicon. Advanced Functional Materials, 2014, 24, pp. 5494-5502.

[140] C. Jeffrey Brinker, and P. Clem. Quartz on Silicon. Science, 2013, 340, pp. 818-819.

[141] B. Imbert, A. Reinhardt, T. Ricart, C. Billard, E. Defaÿ, H. Virieux, T. Jouanneau, F. Pierre, V. Delaye, P. Gergaud, E. Augendre, T. Signamarcheix, C. Deguet, and S. Ballandras. Thin film quartz layer reported on silicon. Joint Conference of the IEEE International Frequency Control and the European Frequency and Time Forum, San Francisco, CA, USA, 2-5 May 2011.

[142] H. Suzaki, H. Kuwae, A. Okada, B. Ma, S. Shoji, and J. Mizuno. ST-quartz/$LiTaO_3$ Direct Bonding Using SiO_2 Amorphous Layers with VUV/O_3 Pre-treatment for a Novel 5G Surface Acoustic Wave Device. International Conference on Electronics Packaging, Sapporo, Japan, 20-22 April 2016, pp. 443-446.

[143] H. Majjad, V. Laude, and S. Ballandras. Low Temperature Bonding of Interface Acoustic Waves Resonators on Silicon Wafers. IEEE Ultrasonics Symposium, Rotterdam, The Netherlands, 18-21 Sept. 2005, pp. 1307-1310.

[144] H. Majjad, D. Gachon, V. Laude, and S. Ballandras. Interface Acoustic Wave Devices Made By Indirect Bonding of Lithium Niobate on Silicon. IEEE Ultrasonics Symposium, Vancouver, BC, Canada, 2-6 Oct. 2006, pp. 1193-1196.

[145] W-C. Shih, T-L. Wang, X-Y. Sun, and M-S. Wu. Growth of c-Axis-Oriented $LiNbO_3$ Films on ZnO/SiO_2/Si Substrate by Pulsed Laser Deposition for Surface Acoustic Wave Applications. Japanese Journal of Applied Physics, 2008, 47(5), pp. 4056-4059.

Chapter 2

[1] W. Flügge. Tensor Analysis and Continuum Mechanics. Springer Berlin Heidelbreg. Berlin, 1986.

[2] P. Grinfeld. Introduction to Tensor Analysis and the Calculus of Moving Surfaces. Springer. New York, 2013.

[3] S. W. Hawking, and G.F.R Ellis. The Large Scale Structure of Space-Time. Cambridge Monographs on Mathematical Physics. Cambridge University Press, 1973.

[4] G. E. Shilov. Linear Algebra. Dover books on advanced mathematics. Dover Publications, 1977.

[5] P. A. M. Dirac. The Principles of Quantum Mechanics. International series of monographs on physics. Clarendon Press, 1981.

[6] K. Kodaira. Complex Manifolds and Deformation of Complex Structures. Springer Berlin Heidelbreg. Berlin, Heidelbreg, 2005.

[7] K. Tanuma. Stroh Formalism and Rayleigh Waves. Journal of Elasticity, 2007, 89(1), pp.5-154.

[8] K.F. Graff. Wave Motion in Elastic Solids. Dover Books on Physics Series. Dover Publications. New York, 1975.

[9] D. Royer, D.P. Morgan, and E. Dieulesaint. Elastic Waves in Solids I: Free and Guided Propagation. Advanced Texts in Physics. Springer Berlin Heidelberg. Berlin, 2000.

[10] C.T. Schröder, and W.R. Jr Scott. On the complex conjugate roots of the Rayleigh equation: The leaky surface wave. Journal of the Acoustical Society of America, 2011, 110(6) pp.2867-2877.

[11] N. Favretto-Cristini, D. Komatitsch, J.M. Carcione, and F. Cavallini. Elastic surface waves in crystals part 1: Review of the physics. Ultrasonics, 2011, 51(6), pp.653-660.

[12] M. Iannitto, T.J. Royston, and R.L. Magin. Identifying fractional viscoelastic models based on surface wave motion. Proceedings of the ASME Design Engineering Technical Conference, 2011, 3, pp.267-274.

[13] A.A. Ipatov, L.A. Igumnov, and A.A. Belov. Boundary element method in three dimensional transient poroviscoelastic problems. Advanced Materials, 2017, pp.331-346.

[14] Q. Ma, and F. Zhou. Propagation conditions of Rayleigh wave in nonhomogeneous saturated porous media. Soil Mechanics and Foundation Engineering. 2016, 53(4), pp.268-273.

[15] M.D. Sharma. Effect of local fluid flow on Rayleigh waves in a double porosity solid. Bulletin of the Seismological Society of America, 2014, 104(6), p.2633.

[16] B. Maruszewski, A. Drzewiecki, and R. Starosta. Magnetoelastic surface waves in auxetic structure. IOP conference series: Materials Science and Engineering, 2010, 10(1), pp.1-9.

[17] P.K. Saroj, and S.A. Sahu. Reflection of plane waves at traction-free surface of a prestressed funcationally graded piezoelectric material half space. Journal of Solid mechanics, 2017, 9(2), pp.411-422.

[18] A.Sur, and M. Kanoria. Three dimensional viscoelastic medium under thermal shock. Engineering Solid Mechanics, 2016, 4(4), pp.187-200.

[19] T. Kamas, V. Giurgiutiu and B. Lin. Modeling and experimentation of thickness mode E/M impedance and Rayleigh wave propagation for piezoelectric wafer active sensors on thick plates. Proceedings of the ASME 2014 Conference on Smart Materials, Adaptive Structures and Intelligent Systems, Rhode Island, USA, 8-10 September 2014.

[20] T.C.T. Ting. Existence of one-component Rayleigh waves, Stoneley waves, Love waves, slip waves and one-component waves in a plate or layered plate. Journal of Mechanics of Materials and Structures, 2009, 4, pp.631-647.

[21] A.H. Fahmy, and E.L. Adler. Computer-program description. Transformation of tensor constants of anisotropic materials due to rotations of the co-ordinate axes. Proceeding of the Institution of Electrical Engineers, 1975, 122(5), pp.591-592.

[22] J.J. Craig. Introduction to Robotics: Mechanics and Controls. Pearson Education Limited. New Jersey, 2013.

[23] D.I. Anderson. Elastic wave propagation in layered anisotropic media. Journal of Geophysical Research, 1961, 66(9), pp.2953-2963.

[24] A. Freedman. On the overlapping resonances concept of acoustic transmission through an elastic plate II: Numerical examples and physical implications. Journal of Sound and Vibration, 1982, 82(2), pp.197-213.

[25] M. Sofer, P. Ferfecki, and P. Sofer. Numerical solution of Rayleigh-Lamb frequency equation for real, imaginary and complex wave numbers. MATEC Web Conference, 2018.

[26] J. Liu, and S. He. Properties of Love waves in layered piezoelectric structures. International Journal of Solids and Structures, 2010, 47(2), pp.169-174.

[27] Y. Chen, J. Wang, J. Du, and J. Yang. Shear-horizontal waves in a rotated y-cut quartz plate on an elastic half space. Philosophical Magazine Letters, 2012, 92(2), pp.77-85.

[28] J. Liu. A Theoretical study on Love wave sensors in a structure with multiple viscoelastic layers on a piezoelectric substrate. Smart Materials and Structures, 2014, 23(7), pp.1-8.

[29] B. Jakoby, and M.J. Vellekoop. Properties of Love waves: applications in sensors. Smart Materials and Structures, 1997, 6(6), pp.668-679.

[30] A. Isobe, M. Hikita, and K. Asai. Propagation properties of Love wave-type surface acoustic wave on α-quartz. Electronics and Communications in Japan (Part II: Electronics), 1996, 79(2), pp.24-30.

[31] N. Naumenko, and B. Abbott. 6E-1 analysis of highly piezoelectric non-leaky saw propagating in rotated y-cuts of lithium niobate with thick metal films or gratings. IEEE Ultrasonics Symposium, Vancouver, BC, Canada, 2-6 Oct. 2006, pp.493-496.

[32] K. Hashimoto, H. Asano, K. Matsuda, N. Yokoyama, T. Omori, and M. Yamaguchi. Wideband Love wave filters operating in Ghz range on Cu-grating/rotated-YX-LiNbO3-substrate structure. IEEE Ultrasonics Symposium, Montreal, Canada, 23-27 Aug. 2004, pp.1330-1334.

[33] A. Isobe, M. Hikita, and K. Asai. Love-wave-type/Rayleigh-wave-type SAW resonators with thick Al-grating structure. Electronics and Communications in Japan (Part II: Electronics), 2005, 88(4), pp.1-8.

[34] S. Crampin. A review of the effect of anisotropic layering on the propagation of seismic waves. Geophysical Journal of the Royal Astronomical Society, 1977, 49(1), pp.9-27.

[35] I. Kawasaki, and K. Koketsu. Rayleigh-Love wave coupling in an azimuthally anisotropic medium. Journal of Physics of the Earth, 1990, 38, pp.361-390.

[36] D.T. Blackstock. Fundamentals of Physical Acoustics. John Wiley & Sons, Toronto, Canada, 2000.

[37] J.F. Nye. Physical Properties of Crystals: Their Representation by Tensors and Matrices. Oxford science publications. Clarendon Press, 1985.

[38] D. Mainprice, F. Bachmann, R. Hielscher, H. Schaeben, and G.E. Llyod. Calculating anisotropic piezoelectric properties from texture data using the MTEX open source package. Geological Society Special Publications, 2015, 409(1), pp. 223-249.

[39] L. Yang, Y-Y. Chen, J.S-T. Yu. Eigenstructure of First-Order Velocity-Stress Equations for Waves in Elastic Solids of Trigonal 32 Symmetry. Journal of Applied Mechanics, 2010, 77(6), pp. 061003 1-15.

[40] T. Pensala, M. Prunnila, and A. Jaakkola. Bulk acoustic wave propagation characteristics in degenerately n-doped Si. IEEE International Frequency Control Symposium Proccedings, Baltimore, MD, USA, 21-24 May 2012.

Chapter 3

[1] A. Tsouvalas, H. Hendrikse, and A. Metrikine. The completeness of the set of modes for various waveguides and its significance for the near-field interaction with vibrating structures. Proceedings of the 9th International Conference on Structural Dynamics, Porto, Portugal, 30 June - 2 July 2014.

[2] S. Amat, S. Busquier, and S. Plaza. Review of some iterative root-finding methods from a dynamical point of view. Scientia, 2004, 10, pp. 3-35.

[3] D.E. Marthaler. An Overview of Mathematical Methods for Numerical Optimization. Numerical Methods for Metamaterials Design, Topics in Applied Physics, 2013, 127, pp. 31-53.

[4] Y-C. Chang. N-Dimension Golden Section Search: Its Variants and Limitations. 2nd International Conference on Biomedical Engineering and Informatics, Tianjin, China, 17-19 Oct. 2009.

[5] D.J. Wilde. Optimum Seeking Methods. Prentice-Hall, New Jersey, USA, 1964.

[6] A.A. Stratonnikov, A.P. Bogatov, A.E. Drakin, and F.F. Kamenets. A semianalytical method of mode determination for a multilayer planar optical waveguide. Journal of Optics A: Pure and Applied Optics, 2002, 4(5), pp. 535-539.

[7] T. Johnson, and W. Tucker. Enclosing all zeros of an analytic function - A rigorous approach. Journal of Computational and Applied Mathematics, 2009, 228, pp.418-423.

[8] J.L.G. Zapata, and J.C.D. Martín, Finding the number of roots of a polynomial in a plane refion using winding number. Computer & Mathematics with Applications, 2014, 67(3), pp.555-568.

[9] C.J. Gillan, A. Schuchinsky, and I. Spence. Computing zeros of analytic functions in the complex plane without using derivatives. Computer Physics Communications, 2006, 175(4), pp. 304-313.

[10] T. Needham. Visual Complex Analysis, Oxford University Press, Oxford, UK, 1998.

[11] D. Royer, D.P. Morgan, and E. Dieulesaint. Elastic Waves in Solids I: Free and Guided Propagation. Advanced Texts in Physics. Springer Berlin Heidelberg. Berlin, 2000.

[12] MathWorks. MATLAB Documentation [Internet]. 2018 [Cited 2 November 2018]. Available from: https://uk.mathworks.com/help/matlab/

[13] S, Musuvathy, E. Cohen, J. Damon and J-K. Seong. Principal Curvature Ridges and Geometrically Salient Regions of Parametric B-Spline Surfaces. Computer-Aided Design, 2010, 43(7), pp. 756-770.

Chapter 4

[1] K.F. Graff. Wave Motion in Elastic Solids. Dover Books on Physics Series. Dover Publications. New York, 1975.

[2] C.T. Schröder, and W.R. Jr Scott. On the complex conjugate roots of the Rayleigh equation: The leaky surface wave. Journal of the Acoustical Society of America, 2011, 110(6) pp. 2867-2877.

[3] N. Favretto-Cristini, D. Komatitsch, J.M. Carcione, and F. Cavallini. Elastic surface waves in crystals part 1: Review of the physics. Ultrasonics, 2011, 51(6), pp. 653-660.

[4] N. Naumenko, and B. Abbott. Transverse Acoustic Anisotropy of Obliquely Propagating LSAW in Resonator Structures on $LiTaO_3$ and $LiNbO_3$ Substrates. IEEE Ultrasonics Symposium, Montreal, Quebec, Canada, 23-27 Aug. 2004, pp. 1561-1564.

[5] T. Makkonen, M. Kalo, V.P. Plessky, J. Knuuttila, W. Steichen, and M.M. Salomaa. Side Radiation of Rayleigh Waves from Synchronous Leaky SAW Resonators. IEEE Ultrasonics Symposium, Munich, Germany, 8-11 Oct. 2002, pp. 85-88.

[6] J. Koskela, J.V. Knuuttila, T. Makkonen, and M.M. Salomaa. Acoustic loss mechanisms in leaky SAW resonators on lithium tantalate. IEEE Transactions on Ultrasonics, Ferroelectrics, and Frequency Control, 2001, 48(6), pp. 1517-1526.

[7] H.S. Park, H-S. Lee, H-S. Lee, H-B. Kim, and Y.H. Kim. Measurement of ultrasonic surface wave velocities in silicon crystals and its comparison with finite element analysis. Japanese Journal of Applied Physics, 2017, 56, 07JB04.

[8] J. Hayashi, M. Gomi, M. Suzuki, S. Kakio, H. Suzaki, T. Yonai, K. Kishida, and J. Mizuno. High-Coupling Leaky SAWs on $LiTaO_3$ Thin Plate Bonded to Quartz Substrate. IEEE International Ultrasonic Symposium, Washington, DC, USA, 6-9 Sept. 2017.

[9] M. Suzuki, M. Gomi, and S. Kakio. Propagation characteristics of longitudinal-type leaky surface acoustic wave on layered structure consisting of $Sc_xAl_{1-x}N$ film/$LiNbO_3$ substrate. Japanese Journal of Applied Physics, 2018, 57, 07LD06.

[10] L. Zhang, Y. Wang, M. Chen, Y. Luo, K. Deng, D. Chen, and W. Fu. A new system for the amplification of biological signal RecA and complimentary single strand DNA probes on a leaky surface acoustic wave biosensor. Biosensors and Bioelectronics, 2014, 60, pp. 259-264.

[11] K. Chang, Y. Pi, W. Lu, F. Wang, F. Pan, F. Li, S. Jia, J. Shi, S. Deng, and M. Chen. Label-free and high-sensitive detection of human breast cancer cells by aptamer-based leaky surface acoustic wave biosensor array. Biosensors and Bioelectronics, 2014, 60, pp. 318-324.

[12] Q. Xu, K. Chang, W. Lu, W. Chen, Y. Ding, S. Jia, K. Zhang, F. Li, J. Shi, L. Cao, S. Deng, and M. Chen. Detection of single-nucleotide polymorphisms with novel leaky surface acoustic wave biosensors, DNA ligation and enzymatic signal amlification. Biosensors and Bioelectronics, 2012, 33(1), pp. 274-278.

[13] Y. Wang, M. Chen, L. Zhang, Y. Ding, Y. Luo, Q. Xu, J. Shi, L. Cao, and W. Fu. Rapid detection of human papilloma virus using a novel leaky surface acoustic wave peptide nucleic acid biosensor. Biosensors and Bioelectronics, 2009, 24(12), pp. 3455-3460.

[14] M.J.S. Lowe. Matrix Techniques for Modeling Ultrasonic Waves in Multilayered Media. IEEE Transactions on Ultrasonics, Ferroelectrics, and Frequency Control, 1995, 42(4), pp. 525-542.

Chapter 5

[1] Z. Li, Y. Jones, J. Hossenlopp, R. Cernosek, and F. Josse. Analysis of Liquid-Phase Chemical Detection Using Guided Shear Horizontal-Surface Acoustic Wave Sensors, Analytical Chemistry, 2005, 77(14), pp. 4595-4603.

[2] J. Hossenlopp, L. Jiang, R. Cernosek, and F. Josse. Characterizaton of epoxy resin (SU-8) film using thickness-shear mode (TSM) resonator under various conditions. Journal of Polymer Science Part B: Polymer Physics, 2004, 42(12), pp. 2373-2384.

[3] Y-T. Lai, H. Ogi, K. Noi, and F. Kato. Viscoelasticity Response during Fibrillation of Amyloid β Peptides on a Quartz-Crystal-Microbalance Biosensor. Langmuir, 2018, 34(19), pp. 5474-5479.

[4] M. Goto, H. Yatsuda, and J. Kondoh. Effect of viscoelastic film for shear horizontal surface acoustic wave on quartz. Japanese Journal of Applied Physics, 2015, 54, 07HD02.

[5] T. Shagawa, H. Torii, F. Kato, H. Ogi, and M. Hirao. Viscoelasticity evolution in protein layers during binding reactions evaluated using high-frequency wireless and electrodeless

quartz crystal microbalance biosensor without dissipation. Japanese Journal of Applied Physics, 2015, 54(9), 096601.

[6] H. Wu, X. Xiong, H. Zu, J.H-C. Wang, and Q-M. Wang. Theoretical analysis of a Love wave biosensor in liquid with a viscoelastic wave guiding layer. Journal of Applied Physics, 2017, 121(5), 054501.

[7] W. Wang, and S. He. Theoretical analysis on response mechanism of polymer-coated chemical sensor based Love wave in viscoelastic media. Sensors and Actuators B: Chemical, 2009, 138(2), pp. 432-440.

[8] N. Barié, U. Stahl, and M. Rapp. Vacuum-deposited wave-guiding layers on STW resonators based on $LiTaO_3$ substrate as Love wave sensors for chemical and biochemical sensing in liquids. Ultrasonics, 2010, 50(6), pp. 606-612.

[9] K. Länge, B.E. Rapp, and M. Rapp. Surface acoustic wave biosensor: a review. Analytical and Bioanalytical Chemistry, 2008, 391(5), pp. 1509-1519.

[7] N. Kumar, and S.P. Singh. Experimental study on vibration and damping of curved panel treated with constrained viscoelastic layer. Composite Structures, 2010, 92(2), pp. 233-243.

[8] E.M. Kerwin. Damping of Flexural Waves by a Constrained Viscoelastic Layer. Journal of the Acoustical Society of America, 1959, 31, pp. 952-962.

[9] J.D. Achenbach. Wave Propagation in Elastic Solids. Elsevier Science. Amsterdam, The Natherlands, 1999.

[10] D. Royer, D.P. Morgan, and E. Dieulesaint. Elastic Waves in Solids I: Free and Guided Propagation. Advanced Texts in Physics. Springer Berlin Heidelberg. Berlin, 2000.

[11] H. Lorenz, M. Despont, N. Fahrni, N. LaBianca, P. Renaud, and P. Vettiger. SU-8: a low-cost negative resist for MEMS. Journal of Micromechanics and Microengineering, 1997, 7(3), pp. 121-124.

[12] V. Laude, D. Gérard, N. Khelfaoui, C.F. Jerez-Hanckes, S. Benchabane, H. Moubchir, and A. Khelif. Anisotropic wave-surface shaped annular interdigital transducer. IEEE Ultrasonics Symposium Proceedings, New York, USA, 28-31 Oct. 2007.

[13] V. Laude, K. Kokkonen, and S. Benchabane. Characterization of surface acoustic wave focusing by an annular interdigital transducer. IEEE International Ultrasonics Symposium, Rome, Italy. 20-23 Sept. 2009.

[14] V. Laude, C.F. Jerez-Hanckes, and S. Ballandras. Surface Green's function of a piezoelectric half-space. IEEE Ultrasonics, Ferroelectrics, and Frequency Control Society, 2006, 53(2), pp. 420-428.

Chapter 6

[1] D.T. Blackstock. Fundamentals of Physical Acoustics. John Wiley & Sons, Toronto, Canada, 2000.

[2] W. Flügge. Tensor Analysis and Continuum Mechanics. Springer Berlin Heidelbreg. Berlin, 1986.

[3] M.J. Holmes, N.G. Parker, and M.J.W. Povey. Temperature dependence of bulk viscosity in water using acoustic spectroscopy. Journal of Physics: Conference Series, 2011, 269(1), DOI:10.1088/1742-6596/269/1/012011.

[4] Z. Yan. Energy leakage rate of Rayleigh wave at fluid-solid interface. The European Physical Journal Applied Physics, 2014, 65(1), DOI:10.1051/epjap/2013130217.

[5] S. Tamura, R.E. Vines, and J.P. Wolfe. Effects of liquid loading on surface acoustic wave in solids. Physical Review B, 1996, 54(1), pp. 5151-5163.

[6] C. Glorieux, K. Van de Rostyne, K. Nelson, W. Gao, W. Lauriks, and J. Thoen. On the character of acoustics waves at the interface between hard and soft solids and liquids. The Journal of the Acoustical Society of America, 2001, 110(3), pp. 1299-1306.

[7] K. Länge, B.E. Rapp, and M. Rapp. Surface acoustic wave biosensor: a review. Analytical and Bioanalytical Chemistry, 2008, 391(5), pp. 1509-1519.

[8] J.C. Andle, and J.F. Vetelino. Acoustics wave biosensors. Sensors and Actuators, 1994, 44(3), pp. 167-176.

[9] D. Royer, D.P. Morgan, and E. Dieulesaint. Elastic Waves in Solids I: Free and Guided Propagation. Advanced Texts in Physics. Springer Berlin Heidelberg. Berlin, 2000.

[10] P. Kielczyński, M. Szalewski, and A. Balcerzak. Effect of a viscous liquid loading on Love wave propagation. International Journal of Solids and Structures, 2012, 49(17), pp. 2314-2319.

Chapter 7

[1] P. Mohanty, D.A. Harrington, K.L. Ekinci, Y.T. Yang, M.J. Murphy, and M.L. Roukes. Intrinsic dissipation in high-frequency micromechanical resonators. Physical Review B, 2002, 66(8), 085416 pp.1-15.

[2] A. Granato, and K. Lücke. Theory of Mechanical Damping Due to Dislocations. Journal of Applied Physics, 1956, 27(6), pp. 583-593.

[3] R.B. Thompson, F.J. Margetan, P. Haldipur, L. Yu, A. Li, P. Panetta, and H. Wasan. Scattering of elastic waves in simple and complex polycrystal. Wave Motion, 2008, 45(5), pp. 655-674.

[4] B. Kim, M.A. Hopcroft, R.N. Candler, C.M. Jha, M. Agarwal, R. Melamud, S.A. Chandorkar, G. Yama, and T.W. Kenny. Temperature Dependence of Quality Factor in MEMS Resonators. Journal of Microelectromechanical Systems, 2008, 17(3), pp. 755-766.

[5] B.L. Foulgoc, T. Bourouina, O.L. Traon, A. Bosseboeuf, F. Marty, C. Breluzeau, J-P. Granchamp, and S. Masson. Highly decoupled single-crystal silicon resonators: an approach for the intrinic quality factor. Journal of Micromechanics and Microengineering, 2006, 16, pp. S45-S53.

[6] I. Voiculescu, and A.N. Nordin. Acoustic wave based MEMS devices for biosensing applications. Biosensors and Bioelectronics, 2012, 33, pp. 1-9.

[7] B.P. Harrington, and R. Abdolvand. In-plane acoustic reflectors for reducing effective anchor loss in lateral-extensional MEMS resonators. Journal of Micromechanics and Microengineering, 2011, 21(8), 085021 pp. 1-11.

[8] M. Weinberg, R. Candler, S. Chandorkar, J. Varsanik, T. Kenny, and A. Duwel. Energy Loss in MEMS Resonators and the Impact on Intertial and RF Devices. Transducers International Solid-State Sensors, Actuators and Microsystem Conference, Denver, CO, USA, 21-25 June 2009, pp. 688-695.

[9] Y. Sun, D. Fang, and A.K. Soh. Thermoelastic damping in micro-beam resonators. International Journal of Solids and Structures, 2006, 43, pp. 3213-3229.

[10] R. Lifshitz, and M.L. Roukes. Thermoelastic Damping in Micro- and Nano-Mechanical Systems. Physical Review B, 2000, 61(8), pp. 5600-5609.

[11] A.M. Gonźalez, A. Garcí, C. Benavente-Peces, and L. Pardo. Revisiting the Characterization of the Losses in Piezoelectric Materials from Impedance Spectroscopy at Resonance. Materials, 2016, 9(2), doi: 10.3390/ma9020072.

[12] R. Peach. On the Existence of Surface Acoustic Waves on Piezoelectric Substrates. IEEE Transactions on Ultrasonics, Ferroelectrics, and Frequency Control, 2001, 48(5), pp. 1308-1320.

[13] J. Liu, and S. He. Properties of Love waves in layered piezoelectric structures. International Journal of Solids and Structures, 2010, 47, pp. 169-174.

[14] J.F. Nye. Physical Properties of Crystals: Their Representation by Tensors and Matrices. Oxford science publications. Clarendon Press, 1985.

[15] E. Bassiouny, and H.M. Youssef. Thermo-Elastic Properties of Thin Ceramic Layers Subjected to Thermal Loadings. Journal of Thermoelasticity, 2013, 1(1), pp. 4-10.

[16] R.D. Mindlin. Equation of High Frequency Vibration of Thermopiezoelectric Crystal Plates. International Journal of Solids and Structures, 1974, 10(6), pp. 625-637.

[17] N. Chakraborty, and M.C. Singh. Reflection and refraction of a plane thermoelastic wave at a solid-solid interface under perfect boundary condition, in presence of normal initial stress. Applied Mathematical Modelling, 2011, 35, pp. 5286-5301.

[18] B. Singh. Rayleigh wave in a thermoelastic solid half-space with impedance boundary conditions. Meccanica, 2016, 51(5), pp. 1135-1139.

[19] N.C. Das, A. Lahiri, S. Sarkar, and S. Basu. Reflection of generalized thermoelastic waves from isothermal and insulated boundaries of a half space. Computer & Mathematics with Applications, 2008, 56(11), pp. 2795-2805.

[20] J.D. Achenbach. Wave Propagation in Elastic Solids. North-Holland Publishing Company. Amsterdam, The Netherlands, 1975.

[21] D. Royer, D.P. Morgan, and E. Dieulesaint. Elastic Waves in Solids I: Free and Guided Propagation. Advanced Texts in Physics. Springer Berlin Heidelberg. Berlin, 2000.

[22] V. Laude, D. Gérard, N. Khelfaoui, C.F. Jerez-Hanckes, S. Benchabane, H. Moubchir, and A. Khelif. Anisotropic Wave-Surface Shaped Annular Interdigital Transducer. IEEE Ultrasonics Symposium Proceedings, New York, USA, 28-31 Oct. 2007, pp. 2115-2118.

[23] C. Zener. Internal friction in solids. Proceedings of the Physical Society, 1940, 52, pp. 152-166.

[24] M.S. Blanter, I.S. Golovin, H. Neuhäuser, and H-R. Sinning. Internal Friction in Metallic Materials. Springer-Verlag, Berlin, Heifelberg, 2007.

[25] D. Royer, and E. Dieulesaint. Elastic Waves in Solids II: Generation, Acousto-optic Interaction, Applications. Springer-Verlag, Berlin, Heidelberg, 2000.

[26] T. Künzig, M. Niessner, G. Wachutka, G. Schrag, and H. Hammer. The effect of the thermoelastic damping on the total Q-factor of state-of-the-art MEMS gyroscopes with complex beam-like suspensions. Procedia Engineering, 2010, 5, pp. 1296-1299.

Appendix A

Elastic Wave Tensor Form

Formulation based on the tensor calculus notation and theory of [1], the continuum tensor formulations of [2] and the 3-dimensional wave formulation of [3].

Tensor notation

A vector $\boldsymbol{a}$ may be written in terms of the covariant $\boldsymbol{z}_i$ or contravariant $\boldsymbol{z}^i$ basis in the following form,

$$\boldsymbol{a} = a^i \boldsymbol{z}_i = a_i \boldsymbol{z}^i. \tag{A.1}$$

Where the Einstein summation convention is assumed over upper and lower repeated indices. The covariant derivative acting on the tensor a_i is given by,

$$\nabla_j u_i = \frac{\partial u_i}{\partial z^j} - \Gamma^m_{ij} u_m, \tag{A.2}$$

$$\nabla_j u^i = \frac{\partial u^i}{\partial z^j} - \Gamma^i_{jm} u^m. \tag{A.3}$$

The Christoffel symbol Γ is required for partial differentiation, it is used to track of the change in coordinate system z_i. The intrinsic derivative $\frac{\delta}{\delta t}$ of a contravariant tensor where t denotes time is given in the following form,

$$\frac{\delta u^i}{\delta t} = \frac{\mathrm{d}u^i}{\mathrm{d}t} + v^j \Gamma^i_{jk} u^k. \tag{A.4}$$

Coordinate free wave equation

Taking the linear strain tensor ε,

$$\varepsilon_{ij} = \frac{1}{2}(\nabla_i u_j + \nabla_j u_i), \tag{A.5}$$

and mechanical conservation as,

$$\sigma^{ij} = C^{ijkl}\varepsilon_{kl}. \tag{A.6}$$

The components of displacements $\boldsymbol{u}$ are denoted u_i, σ_{ij} denotes stress tensor and C_{ijkl} denotes stiffness tensor. Taking the force balance on a three dimensional elastic body, F_i denotes body forces, results in th equilibrium equation as,

$$\nabla_j \sigma^{ij} + F^i = 0. \tag{A.7}$$

Substitution in Newton's second law results in the elastic wave equations,

$$\nabla_j \sigma^{ij} + F^i = \frac{\delta}{\delta t}\left(\rho \frac{\delta u^i}{\delta t}\right). \tag{A.8}$$

Substituting (A.5) and (A.6) into (A.8) results in the form,

$$\nabla_j C^{ijkl}\frac{1}{2}(\nabla_k u_l + \nabla_l u_k) + C^{ijkl}\frac{1}{2}\nabla_j(\nabla_k u_l + \nabla_l u_k) + F^i = \frac{\delta}{\delta t}\left(\rho \frac{\delta u^i}{\delta t}\right). \tag{A.9}$$

Using the definitions of the covariant derivatives (A.2) and (A.3) the terms on the left hand side of the equation can be expanded out into the forms,

$$\begin{aligned} \nabla_j C^{ijkl}(\nabla_k u_l + \nabla_l u_k) = & \\ & \left(\frac{\partial C^{ijkl}}{\partial z^j} + \Gamma^i_{jm} C^{mjkl} + \Gamma^j_{jm} C^{imkl} + \Gamma^k_{jm} C^{ijml}\right. \\ & \left. + \Gamma^l_{jm} C^{ijkm}\right)\left(\frac{\partial u_l}{\partial z^k} + \frac{\partial u_k}{\partial z^l} - 2\Gamma^m_{lk} u_m\right) \end{aligned} \tag{A.10}$$

$$\nabla_j(\nabla_k u_l + \nabla_l u_k) = \left(\frac{\partial^2 u_l}{\partial z^j \partial z^k} - \Gamma^m_{lj}\frac{\partial u_m}{\partial z^k} - \Gamma^m_{kj}\frac{\partial u_l}{\partial z^m} + \frac{\partial^2 u_k}{\partial z^j \partial z^l} - \Gamma^m_{kj}\frac{\partial u_m}{\partial z^l} - \Gamma^m_{lj}\frac{\partial u_k}{\partial z^m} - 2\left[\frac{\partial \Gamma^m_{lk}}{\partial z^j}u_m + \Gamma^m_{lk}\frac{\partial u_m}{\partial z^j} - \Gamma^n_{lj}\Gamma^m_{nk}u_m - \Gamma^n_{kj}\Gamma^m_{ln}u_m\right]\right) \tag{A.11}$$

Cartesian systems

The change in coordinates in the covariant derivative is captured by the Christoffel symbols which can be written in terms of the metric tensor z_{ij},

$$\Gamma^k_{ij} = \frac{1}{2}Z^{km}\left(\frac{\partial Z_{mi}}{\partial Z^j} + \frac{\partial Z_{mj}}{\partial Z^i} + \frac{\partial Z_{ij}}{\partial Z^m}\right). \tag{A.12}$$

For Cartesian coordinates $[Z_1\ Z_2\ Z_3] = [x\ y\ z] = x_i$ the Christoffel symbols for all indices equals zero $\Gamma^i_{jk} = 0$. The equations of motion reduces to the known Cartesian form,

$$\frac{\partial C^{ijkl}}{\partial x^j}\frac{1}{2}\left(\frac{\partial u_l}{\partial x^k} + \frac{\partial u_k}{\partial x^l}\right) + C^{ijkl}\frac{1}{2}\left(\frac{\partial^2 u_l}{\partial x^j \partial x^k} + \frac{\partial^2 u_k}{\partial x^j \partial x^l}\right) + F^i = \frac{\partial}{\partial t}\left(\rho\frac{\partial u^i}{\partial t}\right). \tag{A.13}$$

References

[1] P. Grinfeld. Introduction to Tensor Analysis and the Calculus of Moving Surfaces. Springer. New York, 2013.

[2] W. Flügge. Tensor Analysis and Continuum Mechanics. Springer Berlin Heidelbreg. Berlin, 1986.

[3] D. Royer, D.P. Morgan, and E. Dieulesaint. Elastic Waves in Solids I: Free and Guided Propagation. Advanced Texts in Physics. Springer Berlin Heidelberg. Berlin, 2000.

Appendix B

Linear Piezoelectric and Thermoelastic Formulation

Linear constitution

These constitution relations are formulated using the laws of thermodynamic by minimising the total energy relation, see [1] for a full description. The three constitution equations for stress, electric displacement and entropy density are as follows,

$$\sigma^{ij} = C^{ijkl(E,T)}\varepsilon_{kl} - d^{kij(T)}E_k - \lambda^{ij(E)}\delta T, \tag{B.1}$$

$$D^i = d^{ijk(T)}\varepsilon_{jk} + e^{ij(\varepsilon,T)}E_j + P^{i(\varepsilon)}\delta T, \tag{B.2}$$

$$S = \lambda^{ij(E)}\varepsilon_{ij} + P^{i(\varepsilon)}E_i + \frac{\rho C^{(\varepsilon,E)}}{T_0}\delta T. \tag{B.3}$$

The bracket superscript quantities are fixed process conditions, for the remainer of the appendix these will be dropped for the purpose of reduced notation. All constants of proportionality are assumed to be constant under changes in space x_i and time t.

Set of governing equations

The following formulation are based on work by [2, 3]. The mechanical wave equation, heat equation and Gauss law in a region with zero charge are as follows,

$$\frac{\partial \sigma_{ij}}{\partial x_j} = \rho \frac{\partial^2 u_i}{\partial t^2}, \tag{B.4}$$

$$\frac{\partial q_i}{\partial x_i} = -T_0 \frac{\partial S}{\partial t}, \tag{B.5}$$

$$\frac{\partial D_i}{\partial x_i} = 0. \tag{B.6}$$

The equations for strain, electric field and heat flux are as follows,

$$\varepsilon_{ij} = \frac{1}{2}\left(\frac{\partial u_i}{\partial x_j} + \frac{\partial u_j}{\partial x_i}\right), \tag{B.7}$$

$$E_i = -\frac{\partial \phi}{\partial x_i}, \tag{B.8}$$

$$q_i = -K_{ij} \frac{\partial \delta T}{\partial x_j}. \tag{B.9}$$

Combined system of equations

Differentiate (B.1) with respect to x_j and substitute (B.7) and (B.8),

$$\frac{\partial \sigma^{ij}}{\partial x^j} = C^{ijkl} \frac{\partial^2 u_l}{\partial x^j \partial x^k} + d^{kij} \frac{\partial^2 \phi}{\partial x^j \partial x^k} - \lambda^{ij} \frac{\partial \delta T}{\partial x^j}. \tag{B.10}$$

Differentiate (B.2) with respect to x_i and substitute (B.7) and (B.8),

$$\frac{\partial D^i}{\partial x^i} = d^{ijk} \frac{\partial^2 u_k}{\partial x^i \partial x^j} - e^{ij} \frac{\partial^2 \phi}{\partial x^i \partial x^j} + P^i \frac{\partial \delta T}{\partial x^i}. \tag{B.11}$$

Differentiate (B.3) with respect to t and substitute (B.7) and (B.8),

$$\frac{\partial S}{\partial t} = \lambda^{ij} \frac{\partial^2 u_j}{\partial t \partial x^i} - P^i \frac{\partial^2 \phi}{\partial t \partial x^i} + \frac{\rho C}{T_0} \frac{\partial \delta T}{\partial t}. \tag{B.12}$$

Differentiate (B.9) with respect to x_i,

$$\frac{\partial q^i}{\partial x^i} = -K^{ij} \frac{\partial^2 \delta T}{\partial x^i \partial x^j}. \tag{B.13}$$

Substituting (B.10) into (B.4), (B.12) and (B.13) into (B.5) and (B.11) into (B.6) results in the combined equations of motions,

$$C^{ijkl}\frac{\partial u_l}{\partial x^j \partial x^k} + d^{kij}\frac{\partial^2 \phi}{\partial x^j \partial x^k} - \lambda^{ij}\frac{\partial \delta T}{\partial x^j} = \rho \frac{\partial^2 u^i}{\partial t^2}, \tag{B.14}$$

$$-K^{ij}\frac{\partial^2 \delta T}{\partial x^i \partial x^j} = -T_0 \lambda^{ij}\frac{\partial^2 u_j}{\partial t \partial x^i} + T_0 P^i \frac{\partial^2 \phi}{\partial t \partial x^i} - \rho C \frac{\partial \delta T}{\partial t}, \tag{B.15}$$

$$d^{ijk}\frac{\partial^2 u_k}{\partial x^i \partial x^j} - e^{ij}\frac{\partial^2 \phi}{\partial x^i \partial x^j} + P^i \frac{\partial \delta T}{\partial x^i} = 0. \tag{B.16}$$

References

[1] R.C. Smith. Smart Material Systems: Model Development. SIAM, Philadelphia, USA, 2005.

[2] E. Bassiouny, and H.M. Youssef. Thermo-Elastic Properties of Thin Ceramic Layers Subjected to Thermal Loadings. Journal of Thermoelasticity, 2013, 1(1), pp. 4-10.

[3] R.D. Mindlin. Equation of High Frequency Vibration of Thermopiezoelectric Crystal Plates. International Journal of Solids and Structures, 1974, 10(6), pp. 625-637.

Appendix C

MATLAB Codes

Curves of constant phase procedure

Example MATLAB codes for the curves of constant phase tracking procedure. The following codes are for the partial wave determinant function, therefore the centre of the initial procedure is zero, and the number of solutions is predefined.

Listing C.1 Main function for curves of constand phase.

```
% Partial root tracking by curve of constant phase
function out = phaseTrackPartialRoots(func,realStartRange,
   imagStartRange,rangeSteps,setAngle,numRoots,circleSteps,
   trackStep,converge)

    % Initial procedure
    % call phaseStartSearch function
    startPoints = phaseStartSearch(func,realStartRange,
       imagStartRange,rangeSteps,setAngle,numRoots);

    % Main procedure
    % for each start point run the phase tracking
    out = zeros([1,numRoots]);
    for i = 1:length(startPoints)
        startPoint = startPoints(i);
        % call phaseTracker function
        z = phaseTracker(func,startPoint,circleSteps,trackStep,
           converge);
        out(i) = z;
    end
end
```

Listing C.2 Initial procedure of curves of constant phase.

```
% Four searchs around zero to create a rectangle in complex
   plane
% Minimise the difference between phase and setAngle
function out = phaseStartSearch(func,realRange,imagRange,steps,
   setAngle,numRoots)

    % Length is expected number of outcomes
    out = zeros([numRoots,1]);

    % Step size from search range
    rStep = realRange/(steps-1);
    iStep = imagRange/(steps-1);

    % Root counter
    q = 0;

    % Setting corners of the rectangle
    R1 = -(realRange/2) + (imagRange/2)*1i;
    R2 = (realRange/2) - (imagRange/2)*1i;
    I1 = -(realRange/2) - (imagRange/2)*1i;
    I2 = (realRange/2) + (imagRange/2)*1i;

    % First real axis search
    Xc = R1;
    Xm = R1 - rStep;
    Dc = func(Xc);
    Dm = func(Xm);

    if angle(Dc) > setAngle
        Pc = setAngle - (angle(Dc)-setAngle);
    else
        Pc = angle(Dc);
    end

    if angle(Dm) > setAngle
        Pm = setAngle - (angle(Dm)-setAngle);
    else
        Pm = angle(Dm);
    end
```

```
38
39      for n = 1:steps-1
40          X = R1 + rStep*n;
41          Dn = func(X);
42
43          if angle(Dn) > setAngle
44              Pn = setAngle - (angle(Dn)-setAngle);
45          else
46              Pn = angle(Dn);
47          end
48
49          if Pn < Pc && Pm < Pc
50              q = q + 1;
51              out(q) = Xc;
52          end
53
54          Xc = X;
55          Pm = Pc;
56          Pc = Pn;
57      end
58
59      % Second real axis search
60      Xc = R2;
61      Xm = R2 + rStep;
62      Dc = func(Xc);
63      Dm = func(Xm);
64
65      if angle(Dc) > setAngle
66          Pc = setAngle - (angle(Dc)-setAngle);
67      else
68          Pc = angle(Dc);
69      end
70
71      if angle(Dm) > setAngle
72          Pm = setAngle - (angle(Dm)-setAngle);
73      else
74          Pm = angle(Dm);
75      end
76
77      % Find all minimums between current and setAngle
```

```
78      for n = 1:steps-1
79          X = R2 - rStep*n;
80          Dn = func(X);
81
82          if angle(Dn) > setAngle
83              Pn = setAngle - (angle(Dn)-setAngle);
84          else
85              Pn = angle(Dn);
86          end
87
88          if Pn < Pc && Pm < Pc
89              q = q + 1;
90              out(q) = Xc;
91          end
92
93          Xc = X;
94          Pm = Pc;
95          Pc = Pn;
96      end
97
98      % First imag axis search
99      Xc = I1;
100     Xm = I1 - iStep*1i;
101     Dc = func(Xc);
102     Dm = func(Xm);
103
104     if angle(Dc) > setAngle
105         Pc = setAngle - (angle(Dc)-setAngle);
106     else
107         Pc = angle(Dc);
108     end
109
110     if angle(Dm) > setAngle
111         Pm = setAngle - (angle(Dm)-setAngle);
112     else
113         Pm = angle(Dm);
114     end
115
116     % Find all minimums between current and setAngle
117     for n = 1:steps-1
```

```
        X = I1 + iStep*n*1i;
        Dn = func(X);

        if angle(Dn) > setAngle
            Pn = setAngle - (angle(Dn)-setAngle);
        else
            Pn = angle(Dn);
        end

        if Pn < Pc && Pm < Pc
            q = q + 1;
            out(q) = Xc;
        end

        Xc = X;
        Pm = Pc;
        Pc = Pn;
    end

    % Second imag axis search
    Xc = I2;
    Xm = I2 + iStep*1i;
    Dc = func(Xc);
    Dm = func(Xm);

    if angle(Dc) > setAngle
        Pc = setAngle - (angle(Dc)-setAngle);
    else
        Pc = angle(Dc);
    end

    if angle(Dm) > setAngle
        Pm = setAngle - (angle(Dm)-setAngle);
    else
        Pm = angle(Dm);
    end

    % Find all minimums between current and setAngle
    for n = 1:steps-1
        X = I2 - iStep*n*1i;
```

```
158         Dn = func(X);
159
160         if angle(Dn) > setAngle
161             Pn = setAngle - (angle(Dn)-setAngle);
162         else
163             Pn = angle(Dn);
164         end
165
166         if Pn < Pc && Pm < Pc
167             q = q + 1;
168             out(q) = Xc;
169         end
170
171         Xc = X;
172         Pm = Pc;
173         Pc = Pn;
174     end
175
176     chr = int2str(numRoots);
177     if q ~= numRoots
178         error(['Length of initial search vector is not ',chr])
179     end
180 end
```

Listing C.3 Main procedure of curves of constant phase.

```
% Main procedure of curves of constant phase
function out = phaseTracker(func,startPoint,circleSteps,
   trackStep,magCon)

    radius = 10^trackStep; % Search step size
    p = startPoint;
    setAngle = angle(func(p)); % Redefine setAngle
    circleStep = (2*pi)/circleSteps;

    % 1. First step of main procedure
    % Call circleAngleOutputLowest
    [xi,theta] = circleAngleOutputLowest(func,real(p),imag(p),
       radius,circleSteps,setAngle);
    Di = func(xi);

    th = theta;

    whileCon = 0;
    while whileCon == 0

        % 2. Tracker step of main procedure
        th1 = th + circleStep;
        th2 = th - circleStep;

        xunit = radius * cos(th) + real(xi);
        yunit = radius * sin(th) + imag(xi);
        xA0 = xunit + yunit*1i;
        DA0 = func(xA0);
        if angle(DA0) > setAngle
            PA0 = setAngle - (angle(DA0)-setAngle);
        else
            PA0 = angle(DA0);
        end

        xunit = radius * cos(th1) + real(xi);
        yunit = radius * sin(th1) + imag(xi);
        xA1 = xunit + yunit*1i;
        DA1 = func(xA1);
        if angle(DA1) > setAngle
```

```
        PA1 = setAngle - (angle(DA1)-setAngle);
    else
        PA1 = angle(DA1);
    end

    xunit = radius * cos(th2) + real(xi);
    yunit = radius * sin(th2) + imag(xi);
    xA2 = xunit + yunit*1i;
    DA2 = func(xA2);
    if angle(DA2) > setAngle
        PA2 = setAngle - (angle(DA2)-setAngle);
    else
        PA2 = angle(DA2);
    end

    if PA0 > PA1 && PA0 > PA2
        xf = xA0;
        thf = th;
        whileCon2 = 1;
    elseif PA1 > PA2 && PA1 > PA0
        P1 = PA0;
        P2 = PA1;
        thN = th1;
        Df = DA1;
        whileCon2 = 0;
    elseif PA2 > PA1 && PA2 > PA0
        P1 = PA0;
        P2 = PA2;
        thN = th2;
        Df = DA2;
        circleStep = circleStep*-1;
        whileCon2 = 0;
    end

    % 3. Correction step of main procedure
    r = 0;
    while whileCon2 == 0
        r = r + 1;
        thN = thN + circleStep;

```

```
78              xunit = radius * cos(thN) + real(xi);
79              yunit = radius * sin(thN) + imag(xi);
80              xA = xunit + yunit*1i;
81              DA = func(xA);
82              if angle(DA) > setAngle
83                  P3 = setAngle - (angle(DA)-setAngle);
84              else
85                  P3 = angle(DA);
86              end
87
88              if P2 > P1 && P2 > P3
89                  if abs(Df) < abs(Di)
90                      xunit = radius * cos(thN-circleStep) + real
                            (xi);
91                      yunit = radius * sin(thN-circleStep) + imag
                            (xi);
92                      thf = thN;
93                      xf = xunit + yunit*1i;
94                      whileCon2 = 1;
95                      continue
96                  end
97              end
98
99              P1 = P2;
100             P2 = P3;
101             Df = DA;
102         end
103
104         % Has the solution been lost?
105         if abs(func(xf)) > abs(func(xi))
106             % 4. Reduce magnitude of step
107             if trackStep <= magCon
108                 whileCon = 1;
109                 out = xi;
110             elseif trackStep > magCon
111                 trackStep = trackStep - 1;
112                 radius = 10^trackStep;
113             end
114
115             continue
```

```
116         else
117             xi = xf;
118             th = thf;
119         end
120     end
121 end
122 
123 % circleAngleOutputLowest to be used in phaseTracker
124 function [out,thetaOut] = circleAngleOutputLowest(func,y1,y2,
    radius,circleSteps,setAngle)
125 
126     out = [];
127     thetaOut = [];
128 
129     % Create circle of points in complex plane
130     da = (2*pi)/(circleSteps);
131     th = 0:da:2*pi;
132     xunit = radius * cos(th) + y1;
133     yunit = radius * sin(th) + y2;
134     circleDataSet = xunit + yunit*1i;
135 
136     x = circleDataSet;
137 
138     for i = 1:length(x)
139         p = x(i);
140         z = func(p);
141         if angle(z) > setAngle
142             ANG(i) = setAngle - (angle(z)-setAngle);
143         else
144             ANG(i) = angle(z);
145         end
146     end
147 
148     % Find all minimums between phase and setAngle
149     r = 0;
150     vect = [];
151     for i = 1:(length(ANG)-1)
152         ANG(i);
153         if i == 1
```

```
154             % last and first point are the same so length-1 is
                   used here
155             if (ANG(length(ANG)-1) < ANG(i)) && (ANG(i) > ANG(i
                   +1))
156                 r = r + 1;
157                 vect(r) = x(i);
158                 theta(r) = th(i);
159                 tANG(r) = ANG(i);
160             end
161         else
162             if (ANG(i-1) < ANG(i)) && (ANG(i) > ANG(i+1))
163                 r = r + 1;
164                 vect(r) = x(i);
165                 theta(r) = th(i);
166                 tANG(r) = ANG(i);
167             end
168         end
169     end
170
171     % Select complex point with lowest output magnitude
172     if length(vect) == 2
173         D1 = func(vect(1));
174         D2 = func(vect(2));
175         if abs(D1) < abs(D2)
176             out = vect(1);
177             thetaOut = theta(1);
178         elseif abs(D2) < abs(D1)
179             out = vect(2);
180             thetaOut = theta(2);
181         end
182     end
183 end
```